

# REPORT DOCUMENTATION PAGE

Form Approved  
OMB No. 0704-0188

Public reporting burden for this collection of information is estimated to average 1 hour per response, including the time for reviewing instructions, searching existing data sources, gathering and maintaining the data needed, and completing and reviewing the collection of information. Send comments regarding this burden estimate or any other aspect of this collection of information, including suggestions for reducing the burden, to Washington Headquarters Services, Directorate for Information Operations and Services, 1215 Jefferson Davis Highway, Suite 1204, Arlington, VA 22202-4302, and to the Office of Management and Budget, Paperwork Reduction Project (0704-0188), Washington, DC 20503.

1. AGENCY USE ONLY (Leave blank) 2. REPORT DATE November 1994 3. REPORT TYPE AND DATES COVERED Final Technical Report 01.09.93-31.08.94

4. TITLE AND SUBTITLE  
"Fibre compatible acousto-optic modulator using a gradient index lens"

5. FUNDING NUMBERS  
F49620-93-1-0494

6. AUTHOR(S)  
B.Wacogne, M.P. Roe, T.J. Pattinson and C.N. Pannell

7. PERFORMING ORGANIZATION NAME(S) AND ADDRESS(ES)  
Optoelectronics Research Centre  
University of Southampton  
Hants, SO17 1BJ  
United Kingdom

8. PERFORMING ORGANIZATION REPORT NUMBER

9. SPONSORING/MONITORING AGENCY NAME(S) AND ADDRESS(ES)  
EOARD  
223/231 Old Marylebone Road  
London NW1 5TH

10. SPONSORING/MONITORING AGENCY REPORT NUMBER  
TR-95-04

11. SUPPLEMENTARY NOTES

12a. DISTRIBUTION/AVAILABILITY STATEMENT  
DISTRIBUTION STATEMENT A  
Approved for public release  
Distribution Unlimited

12b. DISTRIBUTION CODE  
19950221 010

13. ABSTRACT (Maximum 200 words)  
We present the work carried out at the Optoelectronics Research Centre concerning acousto-optic modulators. The first part deals with theoretical studies concerning the design of fibre-compatible acousto-optic switcher-connectors. We explain how to build efficient AOM's according to the characteristics required for specific applications. The concept of modulators exhibiting a double curvature is proposed. The second part deals with the deposition and evaluation of sputtered ZnO thin films. This work highlights several new aspects concerning the sputtering of thin piezoelectric films. An *in situ* interferometric method used to measure both the film thickness and the depth resolved optical losses of the film is developed. We also investigate the real piezoelectric activity of sputtered ZnO films. In part III, we present experimental results obtained with the acoustooptic modulators we built. The main results are; a diffraction efficiency in good agreement with the theoretical calculations, a broad frequency range of operation, low transduction losses, the ability to electrically match every type of transducer, and a phase modulation efficiency in optical fibres twice that which has already been published. We also propose new acoustooptic devices we will be able to build within the near future.

14. SUBJECT TERMS

15. NUMBER OF PAGES  
118

16. PRICE CODE

17. SECURITY CLASSIFICATION OF REPORT

18. SECURITY CLASSIFICATION OF THIS PAGE

19. SECURITY CLASSIFICATION OF ABSTRACT

20. LIMITATION OF ABSTRACT

# DISCLAIMER NOTICE





THIS DOCUMENT IS BEST QUALITY AVAILABLE. THE COPY FURNISHED TO DTIC CONTAINED A SIGNIFICANT NUMBER OF COLOR PAGES WHICH DO NOT REPRODUCE LEGIBLY ON BLACK AND WHITE MICROFICHE.

TR-95-04

This report has been reviewed and is releasable to the National Technical Information Service (NTIS). At NTIS it will be releasable to the general public, including foreign nations.

This technical report has been reviewed and is approved for publication.

  
For MICHAEL S. MARKOW, Lt Col, USAF  
Chief, Aerospace Electronics

  
DONALD R. ERBSCHLOE, Lt Col, USAF  
Chief, International Programs

TR-95-04

**FIBRE COMPATIBLE ACOUSTO-OPTIC  
MODULATOR USING A  
GRADIENT-INDEX LENS**

**U.S. Air Force Project Number F 49620-93-1-0494**

**( Final Technical report )**

**Prepared by:**

**B. Wacogne, M.P. Roe, T.J. Pattinson, and C.N. Pannell**

**Optoelectronics Research Centre  
University of Southampton  
Southampton SO17 1BJ  
United Kingdom**

**November 1994**

<b>Accession For</b>	
NTIS GRA&I	<input checked="checked" type="checkbox"/>
DTIC TAB	<input type="checkbox"/>
Unannounced	<input type="checkbox"/>
Justification	
By	
Distribution	
Availability Codes	
Dist	Avail and/or Special
A-1	



# CONTENTS

## GENERAL INTRODUCTION

<b>PART I: THEORETICAL STUDIES</b>	<b>1</b>
<b>PRELIMINARY REMARK</b>	<b>2</b>
<b>I DESIGN OF THE GRADED INDEX LENS DEVICE</b>	<b>3</b>
I-1 Laser beam characteristics in the device	4
I-2 Bragg angle condition	5
I-3 Transducer dimensions	7
I-4 Acoustooptic interaction	11
I-5 Optical coupling losses	13
I-6 Conclusion	15
<b>II CRITERION TO CHOOSE PLANAR OR CYLINDRICAL GEOMETRY</b>	<b>15</b>
II-1 Cylindrical transducer	16
II-2 Planar transducer	17
II-3 Criterion to choose the transducer geometry	17
II-4 Conclusion	18
<b>III COMPARISON BETWEEN THE REQUIRED ACOUSTIC POWER FOR BOTH GEOMETRIES</b>	<b>19</b>
III-1 Diffraction efficiency in a cylindrical geometry	19
III-2 Transducer dimensions in a planar geometry	20
III-3 Acoustooptic interaction in a planar geometry	20
III-4 Conclusion	22
<b>IV DESIGN OF THE TeO<sub>2</sub> DEVICE</b>	<b>23</b>
IV-1 Bragg angle condition and off-axis position	24
IV-2 Transducer dimensions in a cylindrical geometry	25
IV-3 Transducer dimensions in a planar geometry	25
IV-4 Comparison of the 100% power for both geometries	26
IV-5 Conclusion	26

<b>V</b>	<b>DESIGN OF THE ADVANCED DEVICE</b>	<b>27</b>
V-1	General presentation of the device	28
V-1-1	Transducer geometry and modulator curvature	29
V-1-2	Acoustooptic interaction	31
V-2	Determination of the resonant frequency	32
V-2-1	Coupling losses due to a non normal incidence at the output plane	33
V-2-2	Determination of the resonant frequency	35
V-3	Problem due to the beam diameter at the output face of the device	35
V-4	Conclusion	37
<b>VI</b>	<b>ONE PITCH LENS DEVICE - THE ACOUSTOOPTIC FREQUENCY SHIFTER</b>	<b>37</b>
<b>VII</b>	<b>CONCLUSION</b>	<b>39</b>
	<b>REFERENCES PART I</b>	<b>41</b>
<b>PART II :</b>	<b>PIEZOELECTRIC THIN FILMS - Deposition and evaluation</b>	<b>42</b>
<b>I</b>	<b>ZINC OXIDE THIN FILMS - THE MECHANISM OF SPUTTERING</b>	<b>43</b>
I-1	The zinc oxide crystal	43
I-2	The mechanism of sputtering	44
I-3	Description of the RF reactive sputtering system	45
<b>II</b>	<b>INFLUENCE OF THE SPUTTERING PARAMETERS</b>	<b>47</b>
II-1	Description of the experimental studies	48
II-2	Influence of the RF power on the deposition rate	51
II-3	Influence of the sputtering gas pressure	53
II-4	Control of the substrate temperature	55
II-4-1	Evolution of the film density during the first hour of the deposition process	55
II-4-2	Control of the substrate temperature	57
II-5	Problems we met during sputtering	61
<b>III</b>	<b>IN SITU MEASUREMENT OF FILM THICKNESS AND OPTICAL LOSSES</b>	<b>63</b>

III-1 Theoretical considerations	63
III-2 Experimental results	68
III-3 Conclusion	68
<b>IV EFFECTIVE PIEZOELECTRIC ACTIVITY OF ZINC OXIDE FILMS GROWN BY RF PLANAR MAGNETRON SPUTTERING</b>	<b>71</b>
IV-1 Summarise of what we already know	71
IV-2 Consequence for the real resonant frequency	73
IV-3 Conclusion	76
<b>V DEPOSITION OF ZINC OXIDE FILMS ON OPTICAL FIBRES</b>	<b>76</b>
V-1 Introduction	76
V-2 Deposition of ZnO on highly curved surfaces	76
V-3 Conclusion	78
<b>VI CONCLUSION</b>	<b>80</b>
<b>REFERENCES PART II</b>	<b>81</b>
 <b>PART III : EXPERIMENTAL RESULTS CONCERNING THE PIEZOELECTRIC ACTIVITY OF ZnO FILMS</b>	 <b>82</b>
 <b>I PULSE-ECHO TECHNIQUE FOR INSERTION LOSSES EVALUATION</b>	 <b>83</b>
I-1 Basic considerations on pulse-echo technique	83
I-2 Advanced considerations on the calculation of the transducer losses	85
I-2-1 Effect of the acoustic diffraction on the reflected power	86
I-2-2 Acoustic propagation losses	87
I-2-3 Transduction losses	89
I-3 Experimental results	89
I-4 Conclusion	95
<b>II PROBLEM OF ELECTRICAL IMPEDANCE MATCHING</b>	<b>95</b>
II-1 Why is it important to rematch ZnO transducers ?	95
II-2 Electrical matching of piezoelectric transducers	96
II-3 Conclusion	100
<b>III ACOUSTOOPTIC INTERACTION IN A TeO<sub>2</sub> CRYSTAL</b>	<b>100</b>

<b>III ACOUSTOOPTIC INTERACTION IN A <math>\text{TeO}_2</math> CRYSTAL</b>	<b>100</b>
III-1 Dependence of the regime of operation with the applied electric frequency	102
III-2 Diffraction efficiency, rise time, and bandwidth	102
III-3 Problem of the resonant frequency	103
III-4 Conclusion	106
<b>IV OPTICAL PHASE MODULATION USING A FIBRE TRANSDUCER</b>	<b>106</b>
IV-1 Theoretical considerations	108
IV-2 Experimental result	
IV-2-1 Acoustooptic phase modulation in an optical fibre	108
IV-2-2 Problem of maximum applied power	110
IV-3 Conclusion	
<b>V ACOUSTOOPTIC MODULATOR USING A GRADIENT INDEX LENS</b>	<b>110</b>
<b>VI CONCLUSION</b>	
 <b>GENERAL CONCLUSION</b>	 <b>114</b>
 <b>APPENDICES : GENERAL COMMENTS AND DIRECTIONS OF RESEARCH</b>	 <b>116</b>
 <b>I HIGH <math>M_2</math> GRADED INDEX MATERIALS</b>	 <b>116</b>
<b>II ANOTHER TRANSDUCER MATERIAL</b>	<b>117</b>
<b>III NEW ACOUSTOOPTIC DEVICES INVOLVING <math>\text{ZnO}</math> TRANSDUCERS</b>	<b>117</b>

## GENERAL INTRODUCTION

This report describes the work carried out by the Optoelectronics Research Centre, University of Southampton under the U.S. Air Force project number F 49620-93-1-0494, concerning a "Fibre-compatible acousto-optic modulator using a gradient-index lens". It contains details of theoretical and experimental results obtained during the period November 1993- November 1994 on this project in which a large number of acoustooptic modulator fabrication aspect were investigated. The work described in the following sections has been conducted in collaboration with Gooch & Housego Ltd who provided  $\text{TeO}_2$  crystals, and housings for the different experiments we built.

The original project proposal defined the following areas of investigation:

- 1) Theoretical studies on curved acoustooptic modulators
- 2) Experimental investigations of ZnO sputtering
- 3) Realisation of a graded index device.

All these topics have been addressed in the work presented here. Furthermore, it appeared that the project was significantly wider than expected, leading to a large number of supplementary and essential theoretical and experimental studies.

# PART I

## THEORETICAL STUDIES

This section is intended to present the theoretical studies that have been carried out to build a micro-optic frequency shifter/switch based on the use of a cylindrical graded-index lens.

The purpose of this research is the development of a micro-optic component based on the interaction of acoustic waves with an optical beam which will be capable of functioning as a switch and frequency shifter and which will be inherently compatible with optical fibre technology. To this end we propose the use of graded-index structures (i.e. cylindrical structures having radial variation of refractive index) as the acoustooptic interaction medium. Gradient-index structures are currently commercially available in the form of small rod lenses and in the form of gradient-index multimode optical fibres. These lenses are routinely used to couple light from one optical fibre to another, or for beam collimation.

We propose a novel method of generating acoustic waves inside the gradient-index material in order to produce diffracted beams, which because of the inhomogeneous nature of the refractive index distribution, may be imaged directly from fibre to fibre or from fibre to collimated beam. This situation is in direct contrast to conventional bulk acoustooptic modulators (AOMs) which are constructed from materials which are homogeneous (but frequently non-isotropic) and therefore have no imaging properties. One further desirable property of the cylindrical geometry of the graded index structure is that the acoustic waves generated by a piezoelectric transducer deposited on the curved surface will be automatically focused on the axis of symmetry of the lens.

We also propose to study AOMs based on the use of cylindrical  $\text{TeO}_2$  as the acoustooptic interaction medium. The interest in this material is based on its strong acoustooptical properties, giving high optical diffraction. The diffraction efficiency is of crucial importance in the case of a high frequency AOM. Since graded index  $\text{TeO}_2$  rods are not available, these devices will have graded index lenses attached to both ends for fibre to fibre optical coupling.

This part deals with theoretical studies of these different devices. AOMs are evaluated in terms of diffraction efficiency, the applied acoustic power, and other characteristics such as electrical matching, acoustooptic matching, and optical coupling losses. We will also define a criterion suggesting the kind of transducer geometry (planar or cylindrical) which leads to the lowest driving acoustic power.

## PRELIMINARY

### REMARK

#### CHOICE OF THE GRADED INDEX LENS WE INTEND TO USE

The following sections deal with the use of gradient index materials in acoustooptic devices. Before presenting these theoretical studies, we have to determine the kind of graded index lens to use. We will see below that one of the most important parameters is the optical beam diameter at the interaction region, which has to be as small as possible. In particular, we will see that the beam diameter is directly related to the on-axis refractive index and the quadratic constant of the graded index lens. The quadratic constant is directly related to the radial refractive index distribution as shown further. Several graded index lenses are available for the optical wavelength  $\lambda = 633 \text{ nm}$ .

Product Number	Numerical Aperture	On-axis Index	Quadratic constant
06 LGS(D) 112	0.37	1.564	0.247
06 LGS(D) 114	0.46	1.608	0.339
06 LGS(D) 115	0.46	1.608	0.304
06 LGS(D) 116	0.60	1.658	0.428

We will show in the next section, that the corresponding beam diameters are :

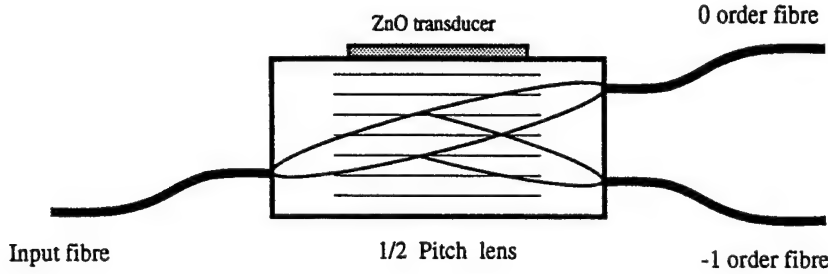
Product Number	(++) 112	(++) 114	(++) 115	(++) 116
Diameter ( $\mu\text{m}$ )	568	402	448	308

The smallest beam diameter is obtained with the (++) 116 lens.

We have also to take into account that the Numerical Aperture (NA) of the lens should match as closely as possible the NA of the optical fibre (NA = 0.11). The aperture of the (++) 116 lens is too large. Therefore, we choose to use the (++) 114 graded index lenses.

## I DESIGN OF THE GRADED INDEX LENS DEVICE

As previous stated, we intend to use the imaging properties of cylindrical graded index lenses to couple the light directly from one input fibre attached to one face of the device, to a pair of output fibres attached to the other face. The basic device is illustrated below:



The device consists of a zinc oxide thin film deposited directly on the curved surface of the graded index lens. This thin film acts as a piezoelectric transducer producing ultrasonic waves in the interaction medium. We choose to use zinc oxide transducers because of their large piezoelectric coupling constant  $k_t$ . This constant is defined as the ratio of the stored electrical energy to the stored elastic energy. It is a function of the piezoelectric constant, the elastic constant, and the permittivity of the material. The following table compare the  $k_t$  of different crystals.

Material	ZnO	CdSe	ZnS	SiO <sub>2</sub>	CdS
$k_t$	0.28	0.13	0.08	0.09	0.15

Ultrasonic waves are generated by applying a high frequency RF voltage to the transducer. The principle of operation is quite simple. When no RF voltage is applied, the light issued from the input fibre is directly imaged onto the 0 order output fibre using the imaging properties of the graded index lens. When RF voltage is applied to the transducers, the light is diffracted by the ultrasonic waves and imaged onto the -1 order output fibre.

The optical fibres are designed for the wavelength  $\lambda = 633$  nm, and exhibit a numerical aperture N.A. = 0.11. The interaction medium (i.e. the AOM) is a half pitch graded index lens. The radial distribution of the refractive index is given by:

$$n(r) = n_0 \left( 1 - \frac{A}{2} r^2 \right) \quad (1)$$

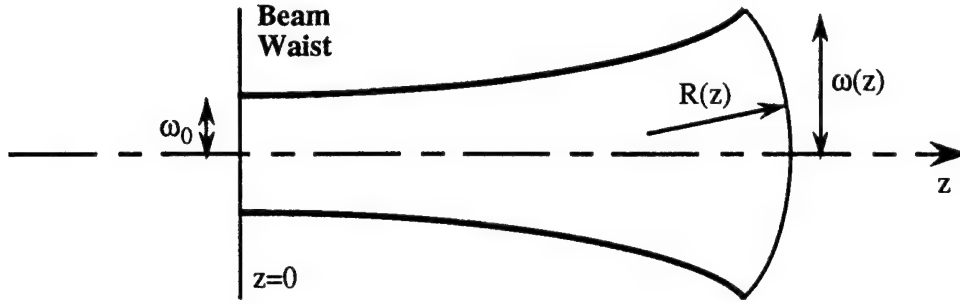
with:  $n_0 = 1.6075$       the refractive index along the lens axis  
 $A^{1/2} = .339 \text{ mm}^{-1}$       the quadratic constant

The lens length is 9.26 mm, and its diameter is 1.8 mm.

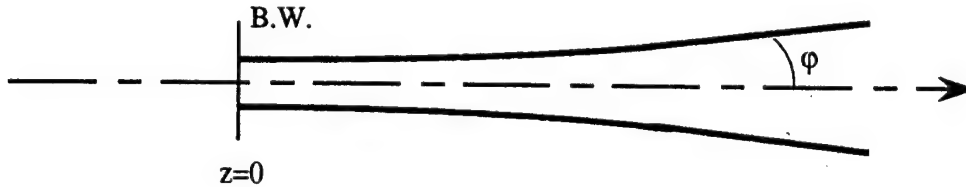


## I-1 Laser beam characteristics in the device.

The purpose of this part is to calculate the evolution of the beam diameter during its propagation through the AOM. In particular, we will determine the optical beam diameter at the plane where the acoustooptic interaction takes place. This is an important parameter because it is directly related to the transducer length as we will see later. A Gaussian beam is conventionally described by the radius of curvature of the wave front and the half beam diameter (measured at  $1/e$  of the maximum amplitude),  $R(z)$  and  $\omega(z)$  respectively (see the figure below).



The coordinate "z" has its origin at the Beam-Waist, which is the plane where the radius of curvature is infinite (the Gaussian beam is then reduced to a plane wave). It can be shown that when the distance from the Beam-Waist is large, the angular divergence of the beam is constant:



This far field angle is given by  $\phi = \lambda / (\pi n \omega_0)$ , where  $\omega_0$  represents half the beam width at the Beam-Waist, and  $n$  the refractive index of the propagation medium.

Taking into account that there is a Beam-Waist at the output face of the input fibre, and that the propagation medium is air ( $n = 1$ ), we can calculate the half beam diameter at the output face by using the numerical aperture (N.A.) of the fibre:

$$N.A. = \frac{\lambda}{\pi \omega_0} \quad \Rightarrow \quad \omega_0 = \frac{\lambda}{\pi (N.A.)} = 1.84 \mu m \quad (1)$$

In order to calculate the beam characteristics (radius of curvature and half diameter) in the graded index lens, we have to consider the propagation of a Gaussian beam through interfaces and

through an anisotropic medium [1,2]. For Gaussian beams, a complex parameter involving the radius of curvature and the half diameter is usually defined as follows:

$$\frac{1}{q(z)} = \frac{1}{R(z)} - j \frac{\lambda_0}{\pi n \omega^2(z)} \quad (2)$$

where  $n$  is the refractive index of the considered medium.

Therefore, the beam characteristics at any coordinate are deduced from the knowledge of the complex parameter. The evolution of this complex parameter depends on the characteristics of the medium (length of the medium, refractive index distribution, interfaces, ...). These characteristics are used to define the "ray transfer matrix" of the medium whose components are A, B, C, and D. The ABCD law gives the output complex parameter  $q_{out}$  as a function of the input one  $q_{inp}$ :

$$q_{out} = \frac{A q_{inp} + B}{C q_{inp} + D} \quad (3)$$

We can then calculate the radius of curvature and the half beam diameter during the propagation through the graded index lens. The result is shown on figure 1. These numerical results lead to the maximum beam diameter at the centre of the graded index lens:

$$\Phi = 402 \mu\text{m}$$

## I-2 Bragg angle condition.

The diffraction efficiency (proportion of the incident light effectively diffracted by the ultrasonic waves) reaches its maximum value when the optical beam is incident at the Bragg angle on the acoustic grating. In a medium whose refractive index is  $n_0$  (the graded index lens), the Bragg angle is defined as follows:

$$\sin(\theta_0) = \frac{\lambda_0}{2 n_0 \Lambda} \quad (4)$$

where  $\lambda_0$  is the optical wavelength  
 $\Lambda$  is the acoustic wavelength  
 $\theta_0$  is the Bragg angle.

We decide to build a piezoelectric transducer resonating at 400 MHz, generating an acoustic wavelength of  $\Lambda = V_{\text{ZnO}} / f_0 = 13.25 \mu\text{m}$  ( $V_{\text{ZnO}} = 5300 \text{ ms}^{-1}$  is the acoustic velocity in ZnO, and  $f_0$  is the resonant frequency). Therefore, the Bragg angle is  $\theta_0 = 14.8 \text{ mrad}$ .

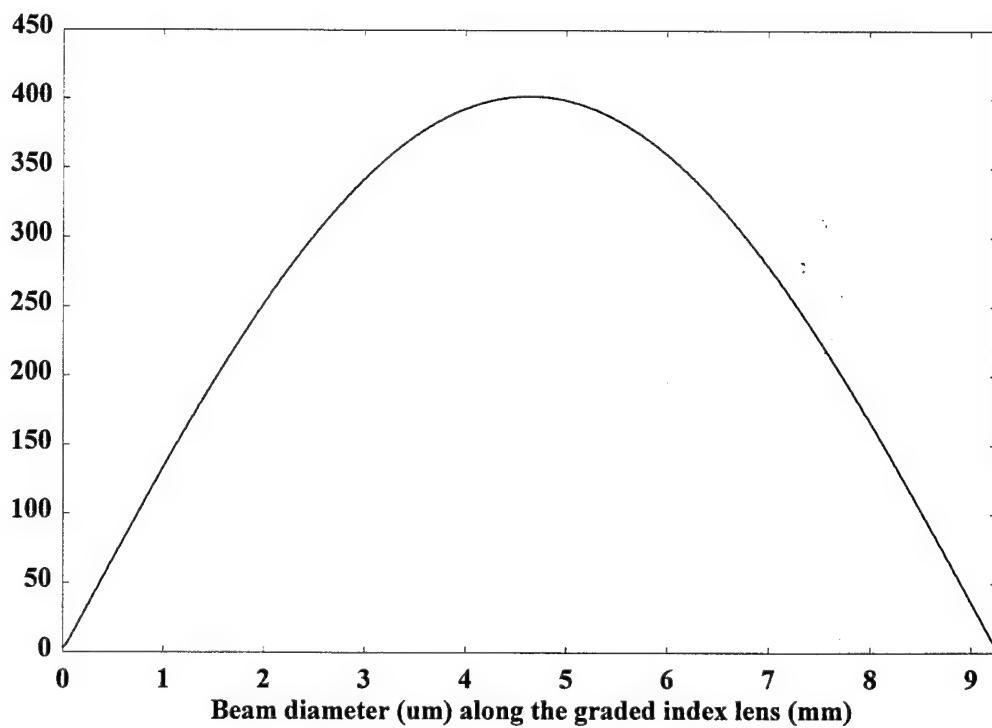
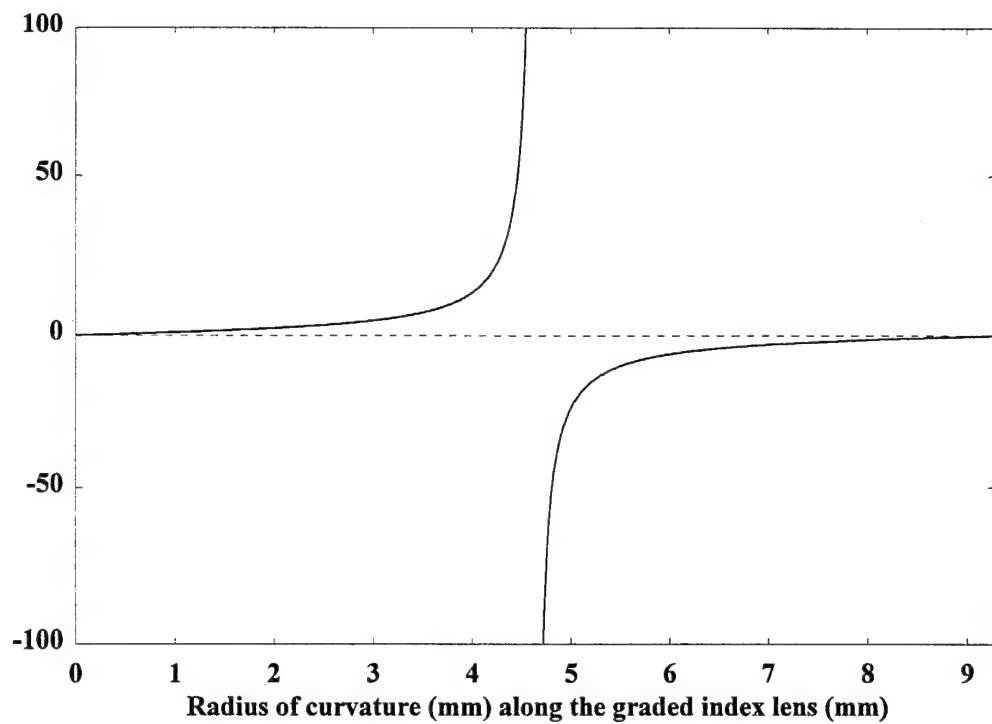
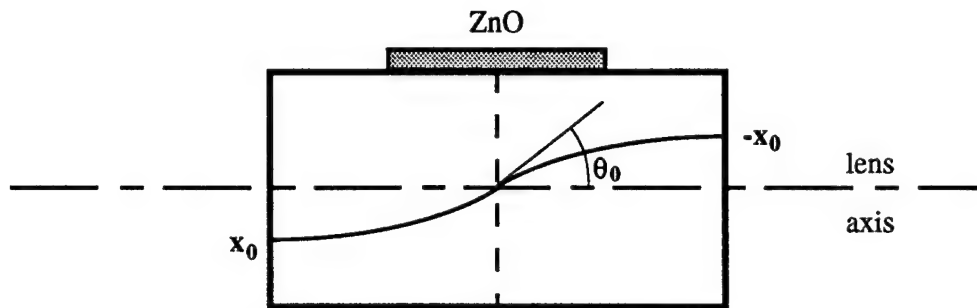


Figure 1: Evolution of the radius of curvature (upper curve) and beam diameter (lower curve) in the graded index lens.

To obtain the maximum diffraction efficiency, the optical beam has to be incident at the Bragg angle at the interaction plane, i.e. the centre of the graded index lens where the acoustic energy is focused by the cylindrical structure of the AOM. Therefore, the input fibre off-axis position has to be calculated so that the above condition is realized. The following figure is an illustration of that Bragg angle condition (only the central plane wave component of the Gaussian beam has been drawn).



The off-axis position  $x_0$  of the input fibre is related to the Bragg angle and to the quadratic constant of the graded index lens. It is calculated by using the ray transfer matrix, and it is given by:

$$x_0 = - \frac{\text{tg}(\theta_0)}{\sqrt{A}} = - 0.05 \text{ mm} \quad (5)$$

Taking into account the symmetry of the device, the distance between the two output fibres is:

$$\Delta = - 2 x_0 = 0.1 \text{ mm}.$$

### I-3 Transducer dimensions

The ZnO piezoelectric transducer will be deposited directly on the curved surface of the graded index lens by RF planar magnetron sputtering. The transducer dimensions are important because they determine the acoustooptic behaviour of the device.

- \* The transducer thickness defines the resonant frequency.
- \* The transducer width determines the spatial extension of the acoustic field in the interaction region, hereby controlling the diffraction efficiency.
- \* The transducer length dictates whether the device operates in the Bragg (single diffracted beam) or in the Raman-Nath regime (multiple diffracted beams)
- \* The transducer area is related to the electrical impedance of the device which should match as closely as possible the transmission line impedance.

### Transducer thickness.

If we decide to build a transducer resonating at 400 MHz, the transducer thickness is then given by:

$$d = \frac{\Lambda}{2} = \frac{V_{\text{ZnO}}}{2f_0} \quad (6)$$

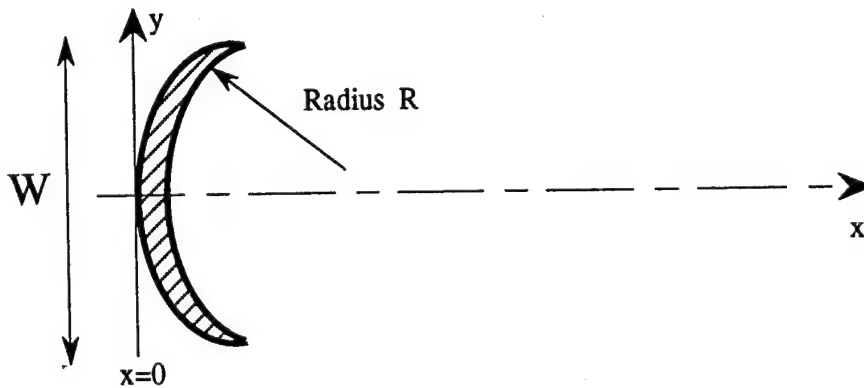
where  $\Lambda$  is the acoustic wavelength  
 $V_{\text{ZnO}}$  is the velocity of sound in the ZnO  
 $f_0$  is the resonant frequency.

Assuming an acoustic velocity of 5300 m/s, the transducer thickness and the acoustic wavelength are respectively:

$$d = 6.625 \mu\text{m} \quad \text{and} \quad \Lambda = 13.25 \mu\text{m}$$

### Transducer width.

We have decided to build a cylindrical AOM to focus the acoustic energy where the acoustooptic interaction takes place. We have now to calculate the width  $W$  of the transducer so that the focused acoustic field will exhibit the same spatial extension as that of the optical field. It is shown in the literature [3] that the acoustic strain amplitude  $S$  can be obtained using a Fresnel diffraction integral. We consider the following transducer:



Assuming that  $S$  is independent of  $z$  because of the transducer length, the acoustic amplitude at the focal plane ( $x = R$ ) is given by:

$$S(R, y) = S_0 \frac{W}{\sqrt{R \Lambda}} \exp(j K y^2 / 2 R) \frac{\sin(K W y / 2 R)}{K W y / 2 R} \quad (7)$$

with  $K$  the acoustic wave vector.

Therefore, the acoustic intensity at the focal plane is:

$$\|S(R, y)\|^2 = S_0^2 \frac{W^2}{R \Lambda} \frac{\sin^2(K W y / 2 R)}{(K W y / 2 R)^2} \quad (8)$$

The condition for the acoustic field to exhibit the same spatial extension as the optical beam can be expressed as:

$$\|S(R, \phi/2)\|^2 = \frac{1}{2} \|S(R, 0)\|^2 \quad (9)$$

where  $\phi$  is the maximum beam diameter in the graded index lens.

Hence, the transducer width is given by:

$$W = \frac{2 R X_0}{K \phi / 2} \quad (10)$$

where  $X_0 = 1.39156$  is defined by:  $\sin^2(X_0) / X_0^2 = 1/2$ .

The transducer width is then:

$$W = 26.3 \mu\text{m}$$

#### Transducer length

Defining the transducer length is more difficult. A compromise must be made between different quantities related to the transducer length.

**Firstly**, in order to obtain a high diffraction efficiency, the optical diffraction has to match the acoustic diffraction. This is because a Gaussian optical beam is formed by the addition of different elementary plane wave components propagating with different wave vector directions (this is called the "angular spectrum" of the Gaussian beam). In the simplest case where all the acoustic waves have the same wave vector, only one of the optical wave components will be incident with the Bragg angle at the interaction region. The other components will be incident with another angle leading to a lower diffraction efficiency. The diffraction matching condition consists of choosing the transducer length so that both acoustic and optical angular spectrum exhibit the same extension. The acoustic diffraction angle is given by  $\delta\theta = \Lambda / 2L$  where  $L$  is the transducer length. The optical diffraction angle is  $\delta\phi = 2\lambda_0 / \pi n_0 \phi$ . Therefore, the transducer length is given by:

$$L = \frac{\pi n_0 \Lambda \Phi}{4 \lambda_0} \quad (11)$$

This relation leads to a transducer length  $L = 10.6$  mm which is unacceptable because it is longer than the graded index lens length (9.26 mm). Moreover, it is shown in the literature [4] that the diffraction efficiency increases as the ratio:  $a = \delta\phi / \delta\theta$  increases. But, if "a" is too large, the modulator bandwidth is reduced. The best compromise consists of choosing  $1.5 < a < 2$ . This condition leads to a transducer length  $15.9 < L < 21.25$  mm. Therefore, it is impossible to find a transducer length satisfying the diffraction matching condition.

**Secondly**, the transducer impedance should match the transmission line impedance ( $50\Omega$ ). If not, a large amount of the incident electric energy will be reflected by the transducer resulting in a dramatic deterioration of the diffraction efficiency. Due to its very small width, we assume that the transducer is planar. Therefore, at the resonant frequency, its electric impedance is given by:

$$Z = \frac{k_t^2 Z_{a0} V_{ZnO}}{\pi^2 f_0^2 \epsilon Z_{a1} W L} \quad (12)$$

where	$k_t = 0.28$	is the ZnO piezoelectric coupling constant
	$Z_{a0} = 36 \times 10^6 \text{ kg/m}^2\text{s}$	is the acoustic impedance of ZnO
	$Z_{a1} = 13.13 \times 10^6 \text{ kg/m}^2\text{s}$	is the acoustic impedance of the graded index lens
	$V_{ZnO} = 5300 \text{ m/s}$	is the velocity of sound in ZnO
	$f_0 = 400 \text{ MHz}$	is the resonant frequency
	$\epsilon = 8.8 \epsilon_0$	is the permittivity of ZnO
	$W = 26.3 \text{ }\mu\text{m}$	is the transducer width
	$L$ to be determined	is the transducer length

Keeping  $Z = 50\Omega$  leads to a transducer length equal to 7.05 mm. Therefore, we have "a" = 0.66 which is quite low, due to the compromise we have to make.

*Finally*, we have to build a device operating in the Bragg regime leading to a single diffracted beam. The first order diffraction efficiency is then higher than in the Raman-Nath regime (multiple diffracted beams). In order to determine the operating regime, the following parameter is used:

$$Q = \frac{2 \pi \lambda_0 L}{n_0 \Lambda^2} \quad (13)$$

The limit  $Q \gg 1$  places the device in the Bragg regime. According to a transducer length equal to 7.05 mm, the corresponding  $Q$  value is 99. Therefore, the device is expected to operate in the Bragg regime.

To conclude, we summarize the dimensions of the device in the following table.

Transducer thickness	Transducer width	Transducer length
$d = 6.625 \mu\text{m}$	$W = 26.3 \mu\text{m}$	$L = 7.05 \text{ mm}$

#### I-4 Acoustooptic interaction

Two very important parameters for acoustooptic modulators are the diffraction efficiency and the rise time. It is important to evaluate the diffraction efficiency of the acoustooptic modulator as a function of the applied acoustic power. As we will see later, the diffraction efficiency is a pseudo-periodic function of the applied acoustic power. In this part, we will calculate the applied acoustic power required to maximise the diffraction efficiency. Another important factor we are going to evaluate, is the rise time of the device. It is usually defined as the time required for the intensity of the diffracted light pulse to increase from 10 % to 90 % of its maximum value.

#### Diffraction efficiency

Assuming that there is no momentum mismatch between the incident light and the acoustooptic propagation vectors (the acoustic and optical diffractions are supposed to be matched), in the case of a Bragg regime operation, the diffraction efficiency is given by [5]:

$$\eta = \frac{I_1}{I_0} = \sin^2(\sqrt{\alpha}) \quad (14)$$

where  $I_0$  is the intensity of the direct undiffracted beam  
 $I_1$  is the intensity of the first order diffracted beam

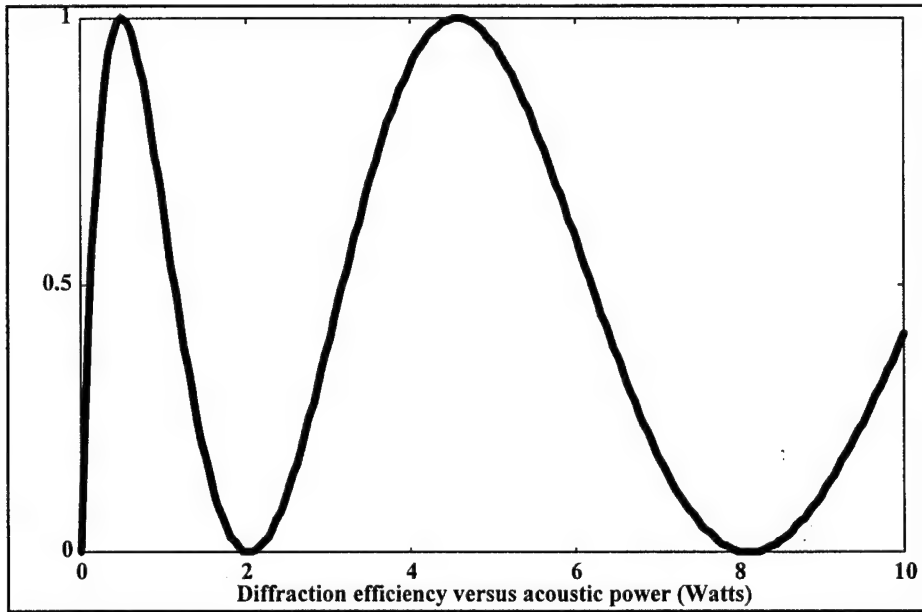


and  $\alpha$  accounts for the acoustooptic properties of the interaction medium (graded index lens), the transducer geometry, and the acoustic power at the interaction region. It is defined as:

$$\alpha = \frac{\pi^2}{2\lambda^2} \frac{n^6 p^2}{\rho V_{bs}^3} \frac{L}{W} P_a \quad (15)$$

where  $P_a$  is the acoustic power at the interaction region  
 $V_{bs} = 5970 \text{ m/s}$  is the acoustic velocity in borosilicate glass (graded index lens)

The quantity  $(n^6 p^2 / \rho V^3)$  is called the  $M_2$  figure of merit, and is related to the acoustooptic properties of the interaction medium. The following figure shows the evolution of the diffraction efficiency with the acoustic power at the interaction region.



We can see the pseudo-periodic variation of the diffraction efficiency with acoustic power. The first maximum is obtained for a very low acoustic power (around 0.5 W). But we have to consider that the above plot refers to the acoustic power at the interaction region. While it is the acoustic power applied to the transducer that is important. The available acoustic power at the interaction region depends strongly on the AOM structure, i.e. a cylindrical or a planar geometry. A cylindrical structure is supposed to be more interesting because the acoustic energy is focused on the optical beam. In the device we are studying, the transducer width is smaller than the optical beam diameter. Therefore, we can expect the applied acoustic power to be larger than the available power at the interaction region. In section II, we will compare the available power for both cylindrical and planar geometry. We will then define a criterion suggesting what kind of geometry we have to consider.

### Rise time

The rise time of the diffracted light pulse is approximately proportional to the time required for the acoustic beam to cross the optical beam. In our case, we can consider that the rise time does not depend on the transducer length because the Bragg angle is so small that the acoustic waves are almost parallel to the optical beam. The rise time is given by [4]:

$$t_r = 1.3 \frac{\phi}{2 V_{bs}} \quad (16)$$

Assuming an acoustic velocity in borosilicate glass equal to 5970 m/s, the rise time is then equal to:

$$t_r = 43.8 \text{ ns}$$

### 1-5 Optical coupling losses

In this section, we are going to estimate the optical coupling losses through the device. We have to take into account the Fresnel reflections at the interfaces and the optical coupling between the graded index lens and the output optical fibres.

#### Fresnel losses.

Since the Bragg angle is very small, we consider the case of a normal incidence. We call  $n_1$  the refractive index of the fibre core. Therefore, the power transmission coefficient for one interface is:

$$T = \frac{4 n_0 n_1}{(n_0 + n_1)^2} \quad (17)$$

The total power transmission through the two interfaces is then:

$$T^2 = 0.9976$$

### Coupling losses.

The coupling efficiency between a Gaussian beam and an optical fibre is given by [6]:

$$\eta_c = \xi \exp\left(-\xi \left[ \frac{x_0^2}{2} \left( \frac{1}{\omega_1^2} + \frac{1}{\omega_0^2} \right) + \frac{\pi^2 \theta^2 (\omega^2(z) + \omega_0^2)}{2 \lambda_0^2} - \frac{x_0 \theta z}{\omega^2} \right] \right) \quad (18)$$

where  $x_0$  is the lateral misalignment  
 $\theta$  is the angular misalignment  
 $\xi$  is a function defined as:

$$\xi = \frac{4}{\omega_1^2 \omega_0^2 \left[ (1/\omega_1^2 + 1/\omega_0^2)^2 - (\pi^2 / \lambda_0^2 R_1^2) \right]} \quad (19)$$

$R_1$  is the radius of curvature of the Gaussian beam where the coupling takes place  
 $\omega_1$  is the half diameter of the Gaussian beam at the Beam-Waist  
 $\omega_0$  Is the beam spot size of the fibre, given by:

$$\frac{\omega_0}{a} = 0.65 + 1.619 / V^{3/2} + 2.879 / V^6 \quad (20)$$

$a$  the core radius  
 $V$  the normalized frequency

We assume that there are no misalignments. The coupling efficiency is then reduced to  $\xi$ . We also assume that coupling losses only occur between the graded index lens and the output fibres. We use the ABCD law to calculate the radius of curvature  $R_1$  and the half diameter at the Beam-Waist. Numeric calculations lead to:

$$R_1 = -0.541 \text{ mm} \quad \omega_1 = 1.839 \text{ } \mu\text{m} \quad \omega_0 = 3.56 \text{ } \mu\text{m}$$

Therefore, the coupling efficiency is:

$$\xi = 0.665$$

The total optical losses are then equal to:

$$\frac{I_{output}}{I_{input}} = T^2 \xi = 0.6634 \quad \Rightarrow \quad losses = - 1.78 \text{ dB}$$

But we have to keep in mind that because of lens aberrations, the minimum waist size may be larger than what we calculate with ABCD law, leading to higher optical losses.

## I-6 Conclusion.

In this section, we have presented theoretical studies about the basic graded index AOM we intend to build. We have seen that it was necessary to make some compromises in order to satisfy as well as possible the different parameters we have to take into account. The optical losses through the device remain relatively low, due to the reduced number of optical components needed to build this AOM. Nevertheless, the rise time is still important due to the relatively large optical beam diameter at the interaction region. In further sections, we will present different AOM geometries leading to a shorter rise time by reducing the beam diameter at the interaction region.

We also have seen that the acoustic power required to obtain 100% diffraction efficiency seems to be very low. We have to keep in mind that the acoustic power we have considered is not the power applied to the transducer, but the available acoustic power where the interaction takes place. This available power depends on the transducer geometry. In the next section, we will discuss the effective acoustic power according to the transducer geometry. In particular, we will show that it is not always a cylindrical geometry is not always worthwhile.

## II CRITERION TO CHOOSE PLANAR OR CYLINDRICAL GEOMETRY.

We have seen in the last section that it was possible to obtain 100% diffraction efficiency with an acoustic power at the interaction region of about 0.5 Watts. But we have to keep in mind that what is important is not the acoustic power at the interaction region, but the acoustic power applied to the piezoelectric transducer.

In this part, we are going to compare the available acoustic power at the interaction region for both cylindrical and planar piezoelectric transducers. We will determine a criterion suggesting which transducer geometry leads to the maximum available acoustic power in the interaction region. The acoustic losses can be neglected because they are the same for both cylindrical and flat transducer (the dimensions of the experimental set-up remain the same).

Equation (14) shows that the diffraction efficiency is given by:

$$\eta = \frac{I_1}{I_0} = \sin^2(\sqrt{\alpha})$$

where  $\alpha$  is a quantity involving the acoustooptic properties of the interaction medium, the transducer geometry, and the acoustic power at the interaction region, and is defined as:

$$\alpha = \frac{\pi^2}{2\lambda_0^2} M_2 \frac{L}{W} P_a$$

where :  $P_a$  is the available acoustic power where the interaction takes place  
 $L$  is the length of the transducer  
 $W$  is its width.  
 $M_2$  is the acoustooptic figure of merit of the interaction medium.

## II-1 Cylindrical transducer.

For a cylindrical transducer, the available acoustic power is multiplied by a factor ( $W^2/R\Lambda$ ) in comparison with a planar transducer, as shown in equation (8). Let  $P_{cyl}$  be the acoustic power applied to the cylindrical transducer. Equation (15) becomes:

$$\alpha = \frac{\pi^2}{2\lambda_0^2} M_2 \frac{LW}{R\Lambda} P_{cyl} \quad (21)$$

Therefore, the power required to obtain 100% diffraction efficiency is (using equation (14)):

$$P_{cyl}^M = \frac{\lambda_0^2}{2M_2} \frac{R\Lambda}{LW} \quad (22)$$

The length  $L$  of the transducer is determined by matching the acoustic and the optical diffraction as explained in the last section. According to [4], the best transducers are those for which the ratio  $a = \delta\phi / \delta\theta$  is equal to 1.5. Thus, the length is given by:

$$L = \frac{a \pi n_0 \Lambda \phi}{4 \lambda_0} \quad (23)$$

For a cylindrical transducer, the width is given by equation (10). Therefore, the power required to obtain 100% diffraction efficiency is:

$$P_{cyl}^M = \frac{\lambda_0^3}{M_2 a n \Lambda X_0} \quad (24)$$

## II-2 Planar transducer.

Since we do not take into account the acoustic losses, the available acoustic power where the interaction takes place is the same as the power applied to the transducer. Let  $P_{flat}$  be the acoustic power applied to the planar transducer. According to equation (14), the power required to obtain 100% diffraction efficiency with a planar transducer is:

$$P_{flat}^M = \frac{\lambda_0^2}{2M_2} \frac{W}{L} \quad (25)$$

The transducer length remains the same as that of a cylindrical geometry (the same diffraction matching condition). In order to compare the behaviour of the two transducer geometries, we will choose the width so that both planar and cylindrical transducers exhibit the same electric impedance. Of course, since the lengths remain the same for both cases, this condition leads to the same value for the transducer width (see equation (12)). The power needed for 100% efficiency operation is then:

$$P_{flat}^M = \frac{\lambda_0^3 R X_0}{\pi^2 M_2 a n \omega_0^2} \quad (26)$$

## II-3 Criterion to choose the transducer geometry.

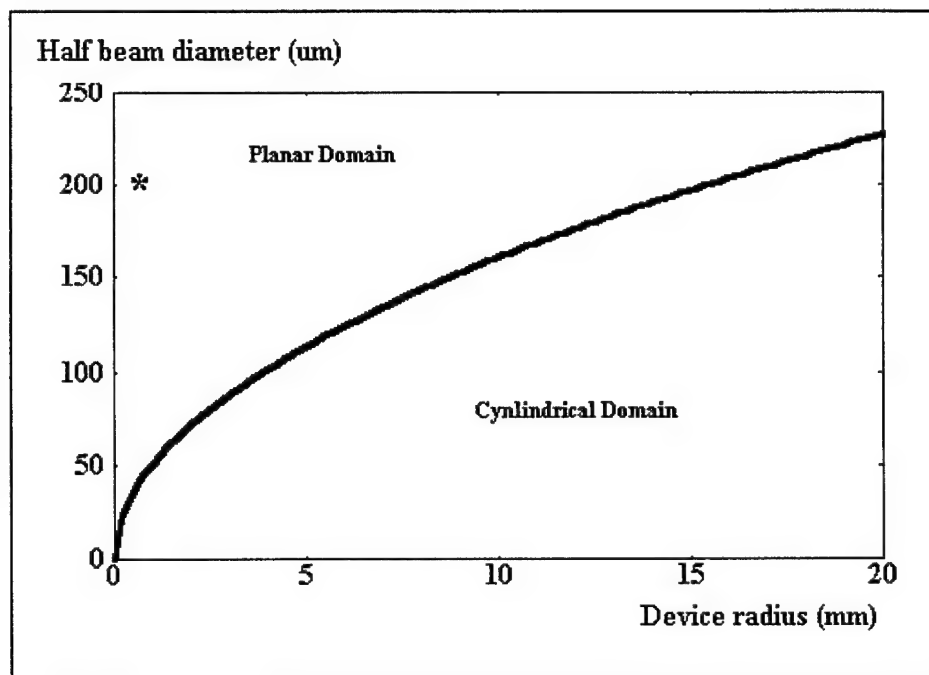
In this section, we define the net gain of the device as:

$$G = \frac{P_{flat}^M}{P_{cur}^M} = \frac{X_0^2}{\pi^2} \frac{R \Lambda}{\omega_0^2} \quad (27)$$

where  $X_0$  is defined by equation (10).

It will be worth using cylindrical geometry only if the net gain  $G$  is greater than 1 (that means that the required power for 100% efficiency operation is lower for a cylindrical than for a planar

transducer). Conversely, if the net gain is less than 1, we will have to choose a planar geometry. The following figure shows the optical half beam diameter at the interaction region as a function of the acoustooptic device diameter in the case where  $G$  is equal to 1. The acoustic wavelength is  $\Lambda = 13.25 \mu\text{m}$



The half space above the curve corresponds to a net gain less than 1 where the planar geometry is better. The half space below the curve corresponds to devices where cylindrical structure is preferable. The star corresponds to the device presented in the last section. It is clear that we have to use a planar transducer in this case.

#### II-4 Conclusion.

In this section, we have established a criterion to choose the geometry necessary for our acoustooptic devices. We have shown that for the device presented in the last section, the planar geometry will lead to a lower applied power for the same diffraction efficiency.

It must be noted that the criterion we have presented is valuable only if the transducer areas are the same for both geometries. If not, it will be necessary to take into account the different compromises that will have been made when designing the devices.

The next section will deal with the study of the same device presented in the last section, but involving a planar transducer.

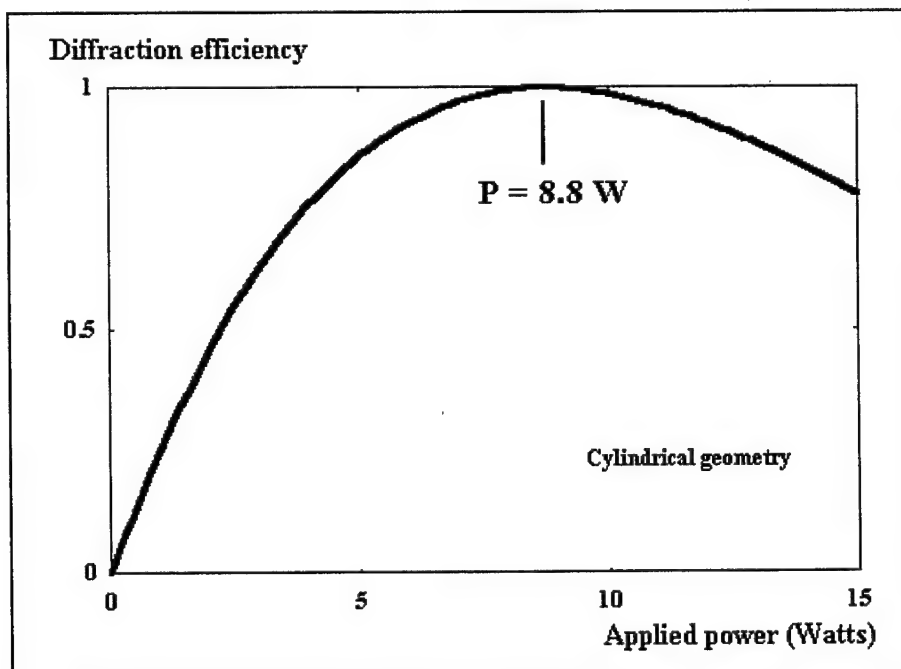
### III COMPARISON BETWEEN THE REQUIRED ACOUSTIC POWER FOR BOTH GEOMETRIES.

We have seen in the previous section that it is better to use a planar geometry if the half diameter of the optical beam is large compared to the device radius. In particular, it appears that the device we have presented in section I requires a lower applied power in a planar than in a cylindrical geometry, to obtain 100% diffraction efficiency. We have to keep in mind that the criterion established below is only valuable if the transducer areas remain the same for both geometries.

In this part, we consider the graded index device presented in section I, and we compare the power required to obtain 100% efficiency in both geometries. For both cases, the thickness  $d$  of the transducer will be the same as that of the device in section I. We will have to determine the transducer width and length in order to find the best compromise between the electrical impedance of the transducer, the  $Q$  parameter (related to the diffraction operation regime), and the "a" parameter (related to the diffraction efficiency).

#### III-1 Diffraction efficiency in a cylindrical geometry.

In section I, we have already determined the transducer dimensions in a cylindrical geometry. In order to determine the power required to obtain 100% diffraction efficiency (we call it the 100% power), we have to consider equation (14) with the quantity  $\alpha$  defined by equation (21). The curve below shows the result for that cylindrical geometry.





The 100% power is then equal to 8.8 Watts, which is rather higher than the 0.5 Watts we have calculated in the first section. In the previous section, we have seen that it was preferable to use a planar than a cylindrical transducer. The problem is that the criterion is only valuable when the transducers exhibit the same dimensions in both geometries. Now, we are going to determine the 100% power for a planar geometry. Firstly, we have to calculate the transducer dimensions in this case.

### III-2 Transducer dimensions in a planar geometry.

In this case, the transducer thickness remains the same, but its width has to be equal to the optical beam diameter. Therefore, we have:

$$W = 402 \mu\text{m}$$

We have seen before that keeping the parameter "a" equal to 1.5 leads to a transducer length larger than the half pitch graded index lens length. Another way to determine the transducer length is to match the electric impedances. By using equation (12), we find:

$$L = 0.46 \text{ mm}$$

Such a length leads to an "a" parameter equal to 0.04 which is rather small. We will then have to find a compromise between the electric impedance matching, the diffraction matching, and the Q parameter. Figure 2 shows the electric impedance of the transducer (keeping the transducer width equal to 402  $\mu\text{m}$ ), the Q parameter, and the a parameter as a function of the transducer length. We choose to consider the following compromise:

$$L = 5.24 \text{ mm} \quad Z = 4.4 \Omega \quad a = 0.493 \quad Q = 74$$

The device will then operate in the Bragg regime. Of course, since the electric impedance is very small, we will have to build a matching circuit in order to reduce the amount of electric energy that will be reflected by the transducer. The problem of impedance matching will be discussed later.

### III-3 Acoustooptic interaction in a planar geometry.

Since the optical beam diameter at the interaction region remains the same, the rise time does not change. We still have:

$$t_r = 43.8 \text{ ns}$$

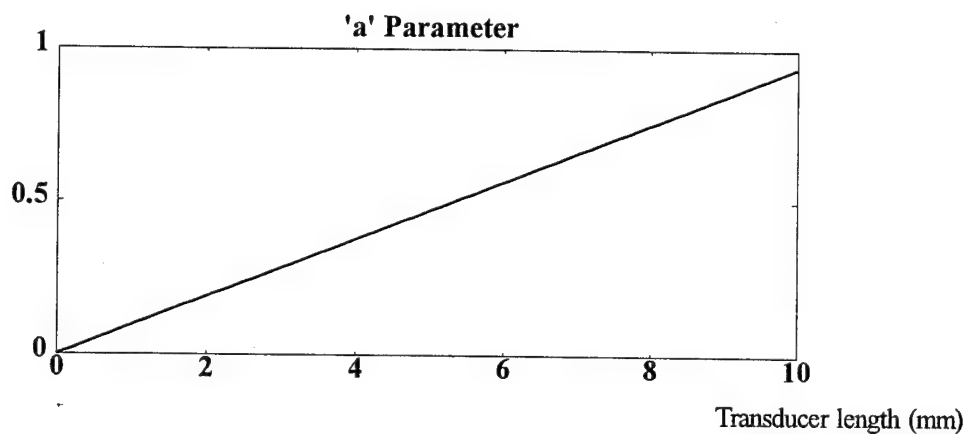
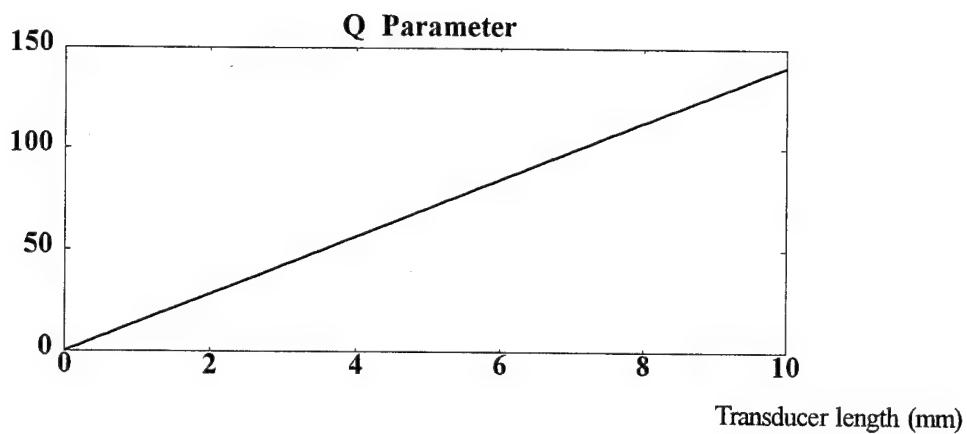
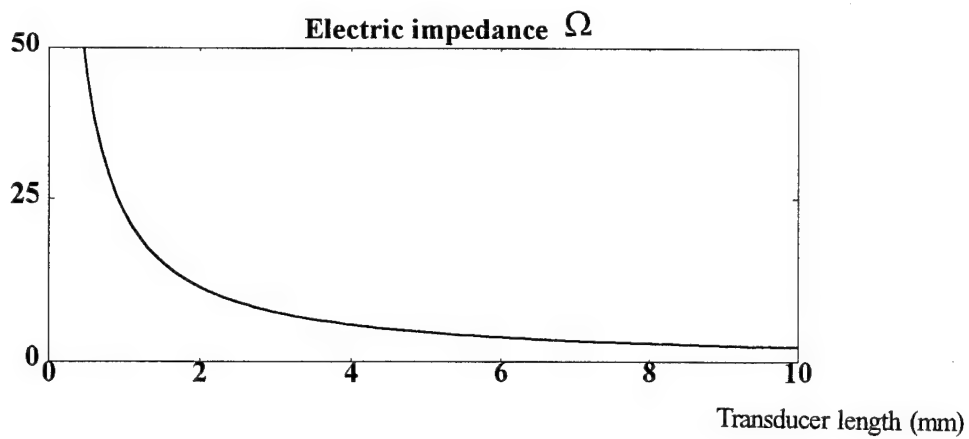
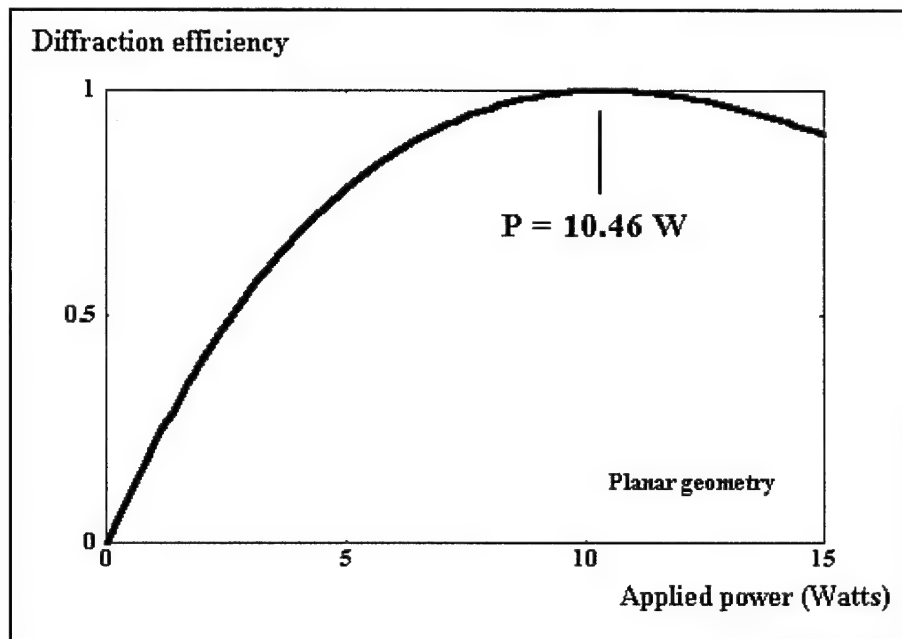


Figure 2: Compromise between the electric impedance, the Q, and "a" factors in the case of a planar geometry

In a planar geometry, the available acoustic power at the interaction region is equal to the acoustic power applied to the transducer (we do not have to consider the acoustic losses to compare the different geometries because they are the same for both cases). Therefore, we calculate the diffraction efficiency by using equations (14) and (15). The curve below shows the evolution of the diffraction efficiency with the applied acoustic power.



The 100% power is then equal to 10.46 W which is larger than the 100% power in a cylindrical geometry.

#### III-4 Conclusion.

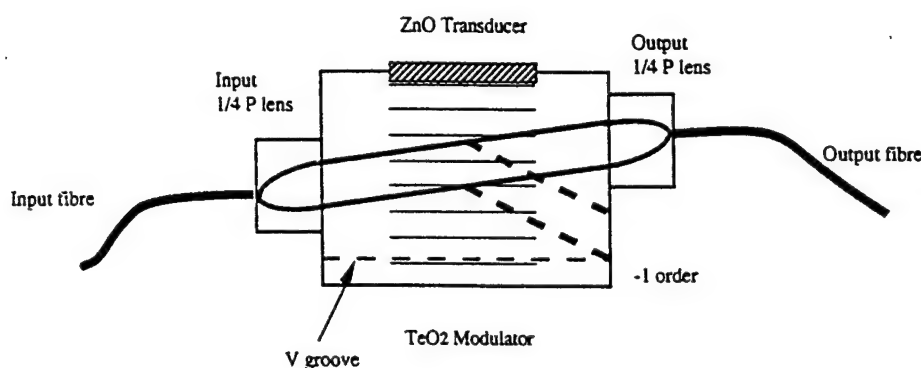
Clearly, the 100% power is higher for a planar than for a cylindrical geometry. This illustrates that the criterion we established in the last section is only valuable when transducer dimensions remain the same. The problem is that from one geometry to another one, we always have to change the transducer dimensions to find a compromise between different quantities. Therefore, each time we will have to study a new device configuration, we will have to compare the 100% power corresponding to both planar and cylindrical geometries.

However, the most important problem concerns the applied power, which is rather high. This is due to the relatively low  $M_2$  figure of merit of borosilicate glass. In order to reduce the 100% power, we have to use a high  $M_2$  interaction medium. In the next section, we will study a device involving a  $\text{TeO}_2$  rod as the interaction medium. The  $\text{TeO}_2$  figure of merit is about 3 times higher than that of borosilicates, therefore, the 100% power is lower.

#### IV DESIGN OF THE $\text{TeO}_2$ DEVICE

As previously stated, this section deals with the study of a device involving a  $\text{TeO}_2$  rod as the interaction medium. Graded index  $\text{TeO}_2$  rods are not commercially available, so we will define a slightly different device involving two quarter pitch graded index lenses attached to both faces of the  $\text{TeO}_2$  modulator. This intermediate solution allows the use of a high  $M_2$  AOM while keeping the imaging properties of graded index lenses. This device is then inherently compatible with optical fibre technology. The problem to find graded index high  $M_2$  material will be discussed at the end of this report. A possible solution could be to build in house graded index lenses.

The device we propose to study is illustrated in the following figure.



The V groove on the bottom of the modulator is used to avoid spurious acoustic reflections, which could induce a standing wave operation.

$\text{TeO}_2$  is an uniaxial birefringent crystal with the following acoustooptic characteristics:

$$\begin{aligned}\rho &= 5990 \text{ kg/m}^3 \\ V_{ac} &= 4260 \text{ m/s} \\ n_z &= 2.4112\end{aligned}$$

$$\begin{aligned}Z_{ac} &= 25.5 \times 10^6 \text{ kg/m}^2\text{s} \\ n_x &= n_y = 2.2585 \\ p &= 0.1\end{aligned}$$

The modulator we intend to use is 15 mm in length, with a radius of  $R = 2.5$  mm. Since the  $M_2$  figure of merit involves the quantity  $n^6$ , we choose an AOM configuration in which the light propagates along the x or y axis, polarized along the z axis, to use the higher refractive index for acoustooptic interaction.

The input quarter pitch graded index lens maintains the laser beam at a constant diameter in the modulator ( $\phi = 402 \mu\text{m}$ ). The optical losses through the device are slightly higher than in the previous case, as a result of the increased number of interfaces. The losses have been calculated

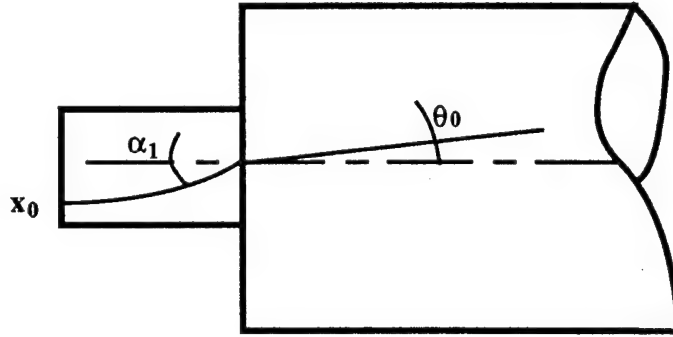
to be -2.13 dB. Since the  $\text{TeO}_2$  refractive index differs from this of borosilicate glass, the Bragg angle, and therefore the off-axis position of the input fibre, which we must calculate, will also differ (we consider that the input lens axis coincides with the modulator axis).

#### IV-1 Bragg angle condition and off-axis position.

For a  $\text{TeO}_2$  AOM resonating at 400 MHz, the Bragg angle can be calculated from equation (4) as:

$$\theta_0 = 9.9 \text{ mrad}$$

In the modulator, the laser beam must propagate at the Bragg angle with respect to the modulator axis. If we consider the following figure (where only the central plane wave component is drawn),



the off-axis position of the input fibre is given by:

$$x_0 = - \frac{n_z}{n_0} \frac{\text{tg}(\alpha_1)}{\sqrt{A}} \quad (28)$$

where the angle  $\alpha_1$  is related to the Bragg angle by the Snell-Descartes law:

$$\sin(\alpha_1) = \frac{n_z}{n_0} \sin(\theta_0) \quad (29)$$

The input fibre off-axis position is then:

$$x_0 = - 0.07 \text{ mm}$$

#### IV-2 Transducer dimensions in a cylindrical geometry.

Since the resonant frequency remains the same, the thickness  $d$  of the transducer is:

$$d = 6.625 \mu\text{m}$$

The transducer width is calculated so that the focused acoustic beam exhibits the same spatial extension as the optical beam. Using equation (10), and considering a modulator radius equal to 2.5 mm, we find:

$$W = 73 \mu\text{m}$$

As we did in section III-2, we have to find a compromise between the  $Q$ ,  $a$ , and  $Z$  to choose the length  $L$  of the transducer. We decide to choose the following compromise:

$$L = 4.36 \text{ mm} \quad Z = 15 \Omega \quad a = 0.3 \quad Q = 41$$

We have now to determine the transducer dimensions for planar geometry.

#### IV-3 Transducer dimensions in a planar geometry.

In a planar geometry, the transducer width is equal to the optical beam diameter. Therefore the width is:

$$W = 402 \mu\text{m}$$

In this case, the compromise is more difficult to choose because the electric impedance of the transducer is very low, due to the high value of the acoustic impedance of  $\text{TeO}_2$ :

$$Z_{\text{ac}} = 25.5 \times 10^6 \text{ kg/m}^2\text{s} \quad \text{for } \text{TeO}_2$$

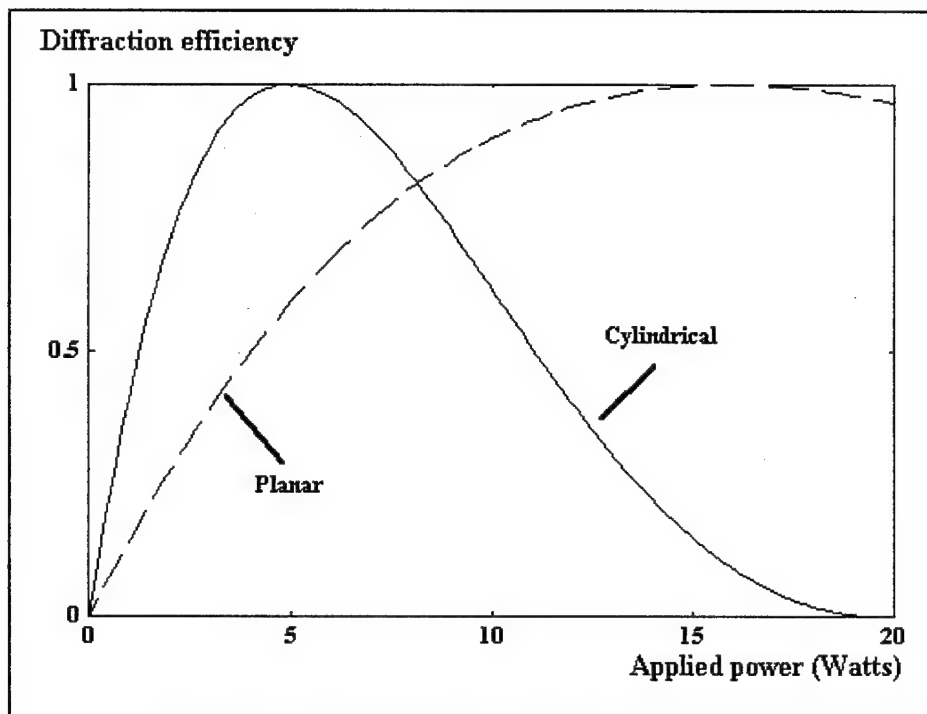
$$Z_{\text{ac}} = 13.13 \times 10^6 \text{ kg/m}^2\text{s} \quad \text{for borosilicate.}$$

Therefore, we choose the following compromise;

$$L = 1.19 \text{ mm} \quad Z = 10 \Omega \quad a = 0.075 \quad Q = 11$$

#### IV-4 Comparison of the 100% power for both geometries.

To calculate the 100% powers, we use equations (14) and (21) for the cylindrical geometry, and equations (14) and (15) for the planar geometry. The following curves represent the evolution of the diffraction efficiency for both geometries.



The 100% powers are 4.9 and 16 Watts for cylindrical and planar geometries respectively.

#### IV-5 Conclusion.

The curves above are another good illustration of what we stated concerning the geometry criterion. For the  $\text{TeO}_2$  device, the criterion established in section II indicates that the planar geometry leads to a lower 100% power while the curves above indicate the contrary. This is because the transducer dimensions depend on the geometry, due to the different compromises we have to consider. For the cylindrical geometry, in spite of a lower available acoustic power where the interaction takes place, the length allowed by the compromise can be larger. Therefore, the  $\alpha$  parameter defined by equation (21) for the cylindrical geometry is higher than the same quantity defined by equation (15) for the planar geometry.

Nevertheless, the 100% power in a cylindrical geometry is still large. The required 4.9 Watts are due to the "a" parameter which is much lower than 1.5. The problem of finding a suitable compromise is due to the fact that we have to choose a transducer length that matches as well as possible both diffraction angles and electric impedances. In the next section, we propose to solve that problem by using a modulator exhibiting curvatures along two perpendicular directions. The curvature whose axis is parallel to the optical beams will be used to focus the acoustic energy. We call it the *longitudinal curvature*, and the radius of curvature R. The curvature whose axis is perpendicular to the acoustooptic interaction plane will be used to match the diffraction angles. We call it the *transversal curvature*, and the radius of curvature r.

We will also decrease the rise time by using 0.29 pitch graded index lenses that will focus the optical beam on the centre of the TeO<sub>2</sub> AOM.

## V DESIGN OF THE ADVANCED DEVICE

This section studies in detail the device involving two perpendicular curvatures. Previous sections have shown that the main difficulty consists of choosing a suitable compromise between the different parameters we have defined. In particular, since the transducer width is fixed by the optical beam diameter and the geometry, it is impossible to find a transducer length matching both the required diffraction angle and the electrical impedances.

If we consider that the transducer also possesses a transversal curvature, the acoustic diffraction angle is given by  $\delta\phi = L / 2r$  [4]. Therefore, since the transducer width is fixed, the electrical matching condition defines the transducer length, and fulfilling the diffraction condition determines the modulator transversal radius of curvature.

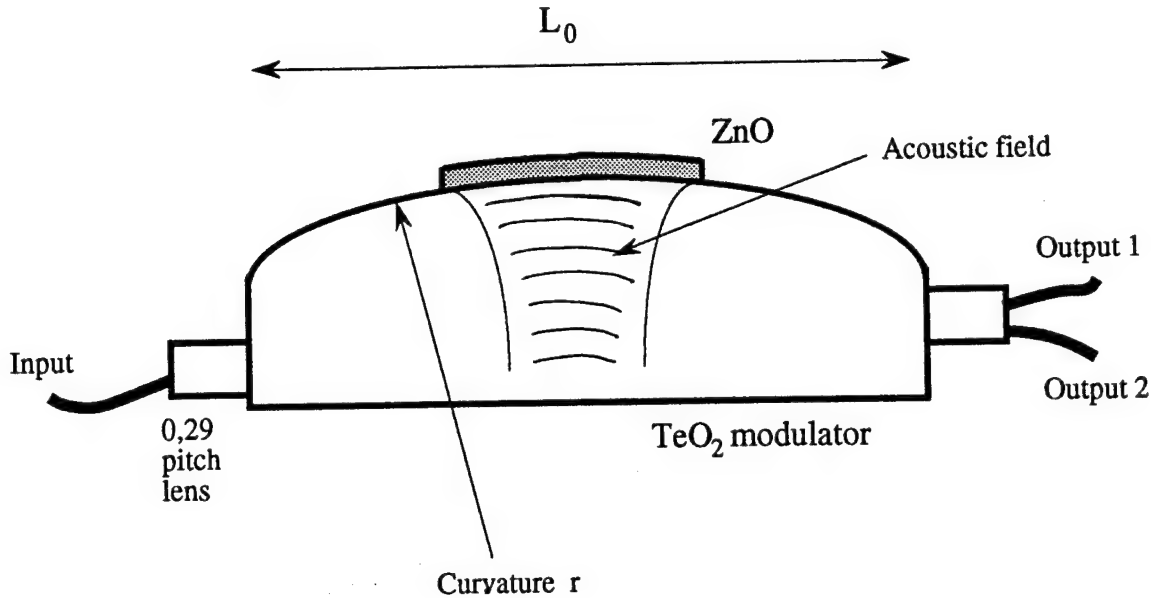
We also propose to reduce the rise time of the device by using 0.29 pitch graded index lenses. However, we will have to calculate the modulator length so that the optical beam is focused directly to the centre of the device, bearing in mind that the device is expected to be compatible with fibre technology. Therefore, the space between the two output fibres will have to be equal to a fibre diameter ( $\Delta = 125 \mu\text{m}$ ), and the optical coupling losses must be as low as possible.

We will see further that the resonant frequency has to be changed, and that we will have to use an asymmetric AOM.



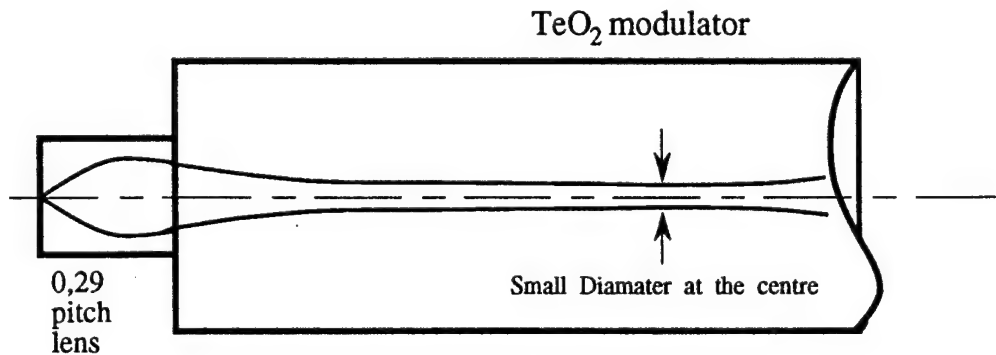
## V-1 General presentation of the device

The device we intend to study is illustrated below.



For the moment, we consider that the acoustooptic interaction takes place at the centre of the AOM. We will have to calculate the modulator length  $L_0$  that corresponds to an optical Beam-Waist situated at a distance  $L_0 / 2$  from the input face of the modulator. We will also have to choose between the cylindrical (longitudinal curvature) or the planar geometry.

We will not present all the calculations we did to calculate the modulator length, and the optical beam diameter at the interaction region. These values can be calculated by using the ABCD law, and by considering the ray transfer matrix corresponding to the space between the input fibre and the inside of the TeO<sub>2</sub> modulator. The figure below shows the evolution of the optical beam in the device when using 0.29 pitch graded index lenses.



We consider that there is a Beam-Waist at the centre of the AOM to determine its length. The radius of curvature of the optical beam is then infinite at a distance  $L_0 / 2$ , leading to the following values:

$$\begin{aligned} \text{Modulator length} & L_0 = 34.42 \text{ mm} \\ \text{Beam diameter at the centre } \phi & = 14.788 \text{ } \mu\text{m}. \end{aligned}$$

#### V-1-1 Transducer geometry, and modulator transversal curvature.

In this part, we determine the geometry that we will have to consider. Then, we calculate the transducer dimensions and the modulator transversal curvature, for a resonant frequency of about 666 MHz ( $\Lambda = 7.96 \text{ } \mu\text{m}$ ) as we will see further. If we consider a cylindrical geometry (longitudinal curvature  $R = 2.5 \text{ mm}$ ), the transducer width, given by equation (10), is equal to:

$$W = 1.192 \text{ mm}$$

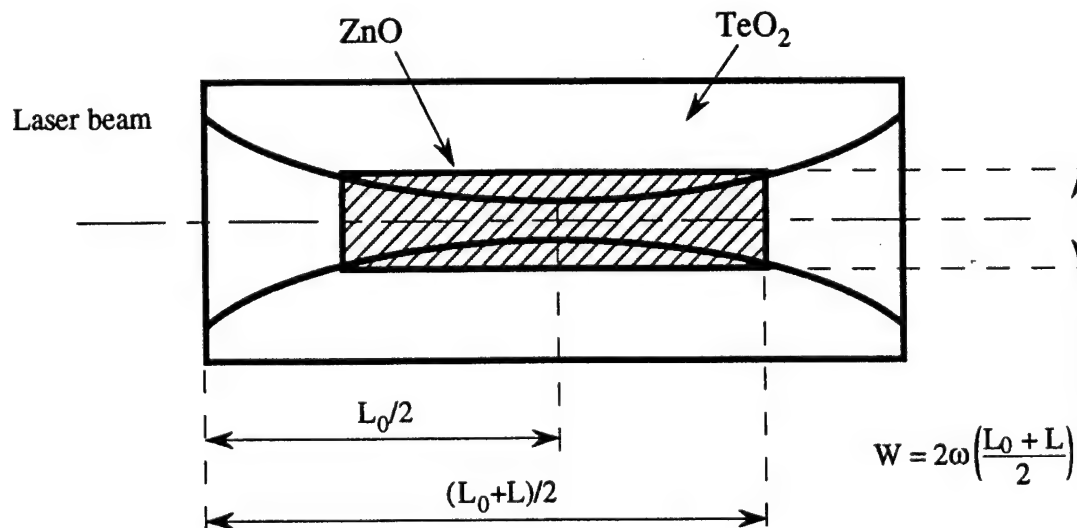
The electric matching condition, equation (12) leads to the transducer length:

$$L = 28.9 \text{ } \mu\text{m}.$$

Firstly, such a length leads to  $Q = 0.75$  placing the device in the Raman-Nath regime. Secondly, according to [4] the diffraction condition for a transducer exhibiting a transversal curvature  $r$  leads to the following "a" parameter:

$$a = \frac{4 \lambda_0 r}{\pi \phi n_z L} \quad (30)$$

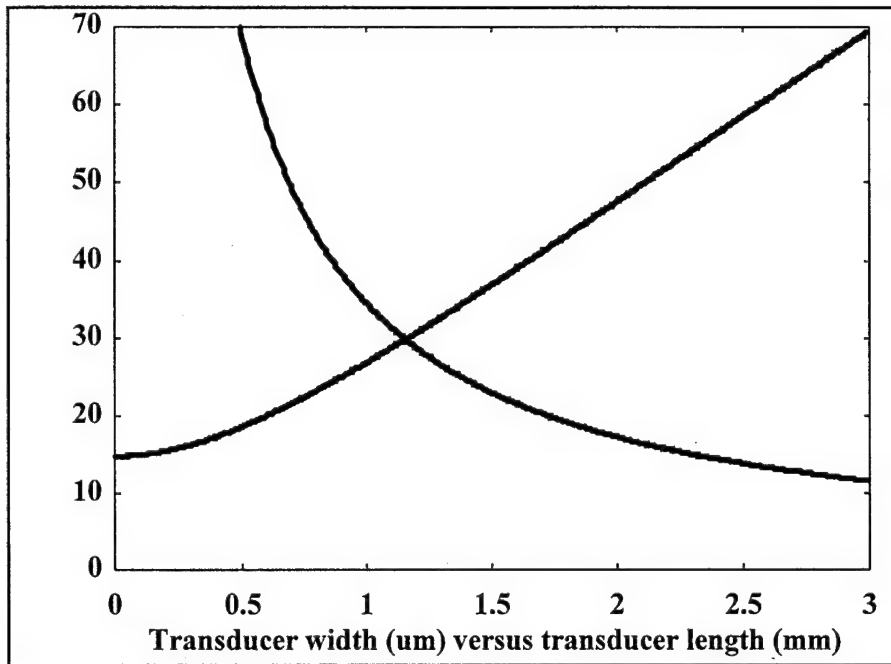
Therefore, keeping  $a = 1.5$ , the transversal curvature is  $r = 1.92 \text{ mm}$ . It will be very difficult to deposit oriented ZnO on such a curved surface. Consequently, we choose the planar geometry. We consider the following figure that represents a top view of the device.



Now, we have to calculate the width  $W$  and the length  $L$  of the transducer so that:

- the width  $W$  is equal to the beam diameter at a distance  $(L_0 + L) / 2$
- the area ( $WL$ ) of the transducer leads to an electric impedance equal to  $50 \Omega$

We use the ABCD law to calculate the evolution of the optical beam diameter in the modulator, and equation (12) to determine the electric impedance. The following figure shows the width as a function of the length for the two conditions above.



The transducer dimensions that verify these conditions are given by the intersection between the two curves, leading to:

$$\begin{aligned} L &= 1.15 \text{ mm} \\ W &= 30 \mu\text{m} \end{aligned}$$

Therefore, equation (30) leads to the modulator transversal curvature:

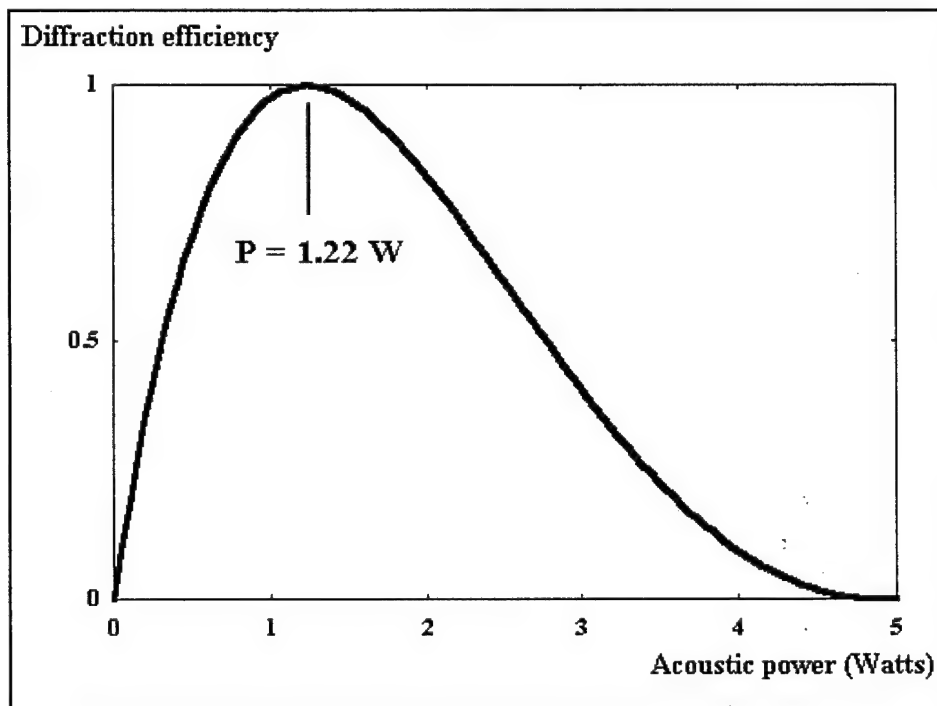
$$r = 76.32 \text{ mm}$$

### V-1-2 Acoustooptic interaction.

To calculate the rise time, we consider that the optical beam diameter varies from 14.788 to 30  $\mu\text{m}$  in the interaction region. Therefore, by using equation (16), the rise time is:

$$2.26 \text{ ns} < t_r < 4.58 \text{ ns}.$$

The curve below shows the evolution of the diffraction efficiency with the applied acoustic power. For this calculation, we used equation (15) in the planar transducers regime.



The 100% power is about 1.22 Watts, which is a great improvement.

The device we have presented is supposed to be the most interesting ; very low rise time, low 100% power, and no compromise between the different transducer characteristics. Unfortunately, we will see further that the main problem concerns the optical coupling between the output lens and the output optical fibres. In particular, we will see that we have to choose the resonant frequency of the device so that the space between the two output fibres is equal to  $\Delta = 125 \mu\text{m}$  (equal to a fibre diameter). We will see that it is possible only by considering an asymmetric device.

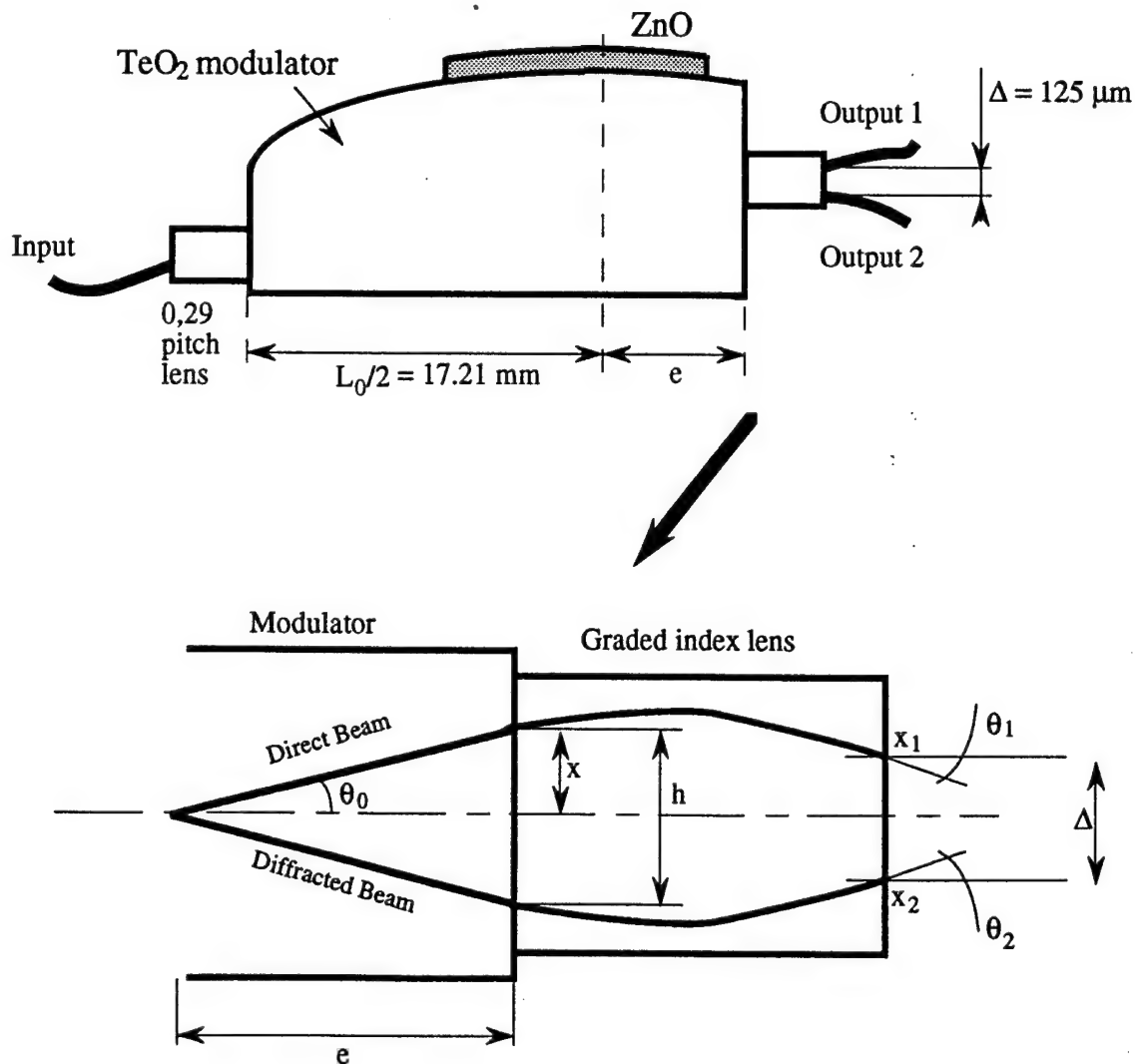
## V-2 Determination of the resonant frequency.

We now calculate the resonant frequency required to allow an output fibres separation of 125  $\mu\text{m}$ . The Bragg angle can be related to the separation of the output beams by the ray transfer matrix of the device. Let us determine the Bragg angle required to obtain  $\Delta=125 \mu\text{m}$ . The relation between these two quantities is:

$$\frac{\Delta}{\text{tg}(\theta_0)} = L_0 \cos(d\sqrt{A}) + \frac{2n_z}{n_0\sqrt{A}} \sin(d\sqrt{A}) \quad (31)$$

Equation (31) leads to a Bragg angle equal to  $85^\circ$  which, of course is not acceptable.

Now, we consider the asymmetric device shown below.



$\Delta$	is the distance between the two output beams corresponding to a fibre diameter.
$x_1, x_2$	are the output beam positions (subscripts 1 and 2 refer to the direct and the diffracted beam respectively)
$\theta_1, \theta_2$	are the angles of the above beams with respect to the device axis
$\theta_0$	is the Bragg angle
$e$	is the "working" distance from the centre of the interaction region and the output face of the modulator
$h$	is the distance between the two beams at the output face of the modulator.

#### V-2-1 Coupling losses due to a non normal incidence at the output plane.

In section I, we have calculated the coupling losses between the graded index lens and the output fibre. Equation (18) shows that the coupling efficiency is higher when there is no misalignment. That means that the best coupling is obtained when the output angles ( $\theta_1$  and  $\theta_2$ ) are equal to zero. By using the ray transfer matrix, it can be shown that the direct beam position  $x$  (see figure above) for which the output angles are equal to zero is given by:

$$x = \frac{\operatorname{tg}(\theta_0)}{\operatorname{tg}(d\sqrt{A})} \frac{n_z}{n_0\sqrt{A}} \quad (32)$$

Using a 0.29 pitch graded index lens leads to a negative value for  $x$ , which is unacceptable (the direct beam has to be above the diffracted beam). In further section we will have to take into account the coupling losses due to a non normal incidence on the output fibres. To keep the calculation relatively simple, we choose a device configuration in which the output angles are equal. This condition leads to:

$$h = 2x$$

We have calculated the coupling losses by using equation (18). Figure 3 shows these coupling losses as a function of the output angle. It is evident that we will have to choose a configuration in which the output angle is less than 3 or 4 degrees.

Coupling losses (dB)

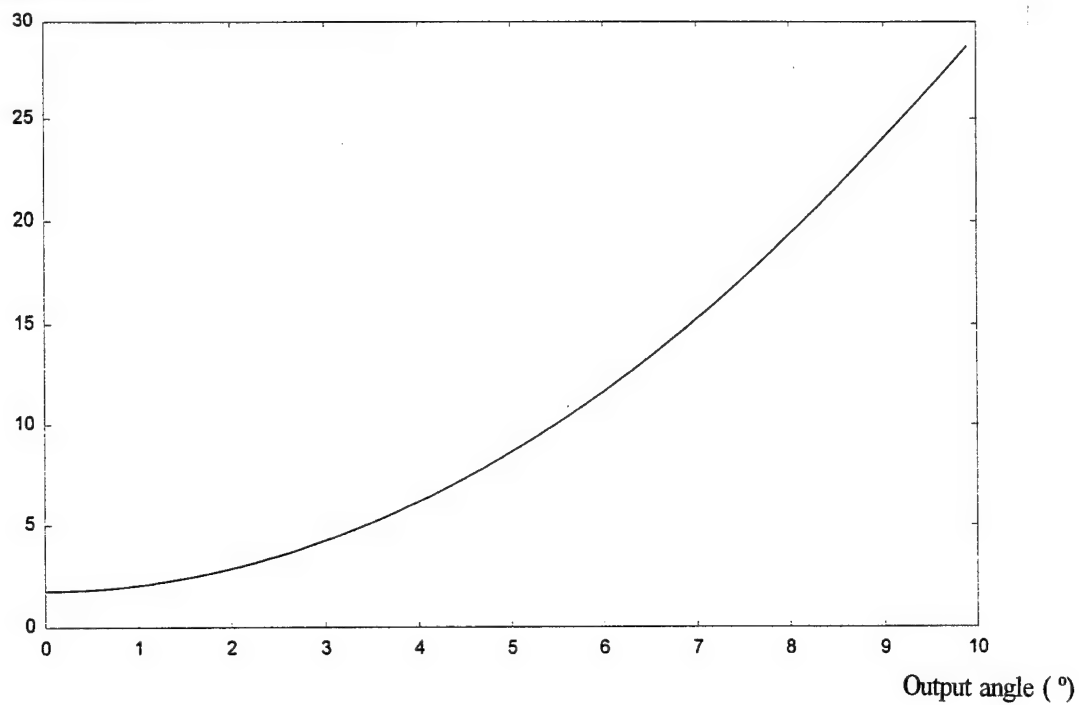


Figure 3: Coupling optical losses as a function of the output angle

Resonant frequency (MHz)

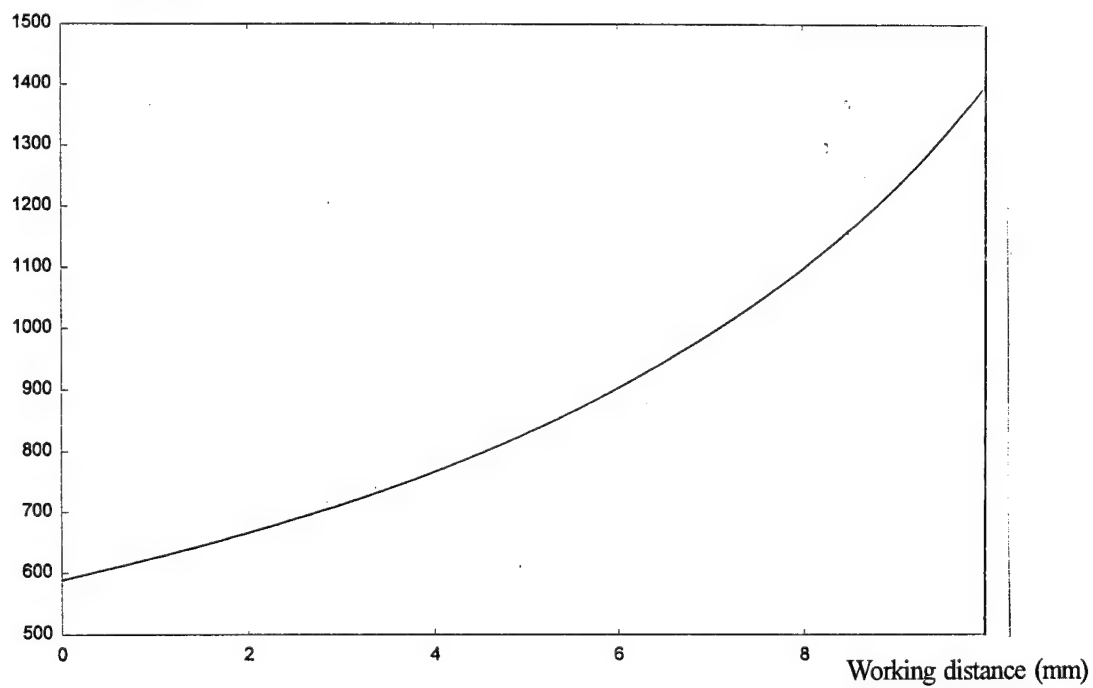


Figure 4: Resonant frequency as a function of the working distance

### V-2-2 Determination of the resonant frequency.

It can be shown that the resonant frequency is related to the distance  $\Delta$  and the working distance "e" by:

$$f_0 = \frac{\Delta n_z V_{ZnO}}{\lambda_0 [ e \cos(d\sqrt{A}) + (n_z/n_0\sqrt{A}) \sin(d\sqrt{A}) ]} \quad (33)$$

Figure 4 shows the resonant frequency as a function of the working distance "e" between the interaction region and the output face of the modulator. Before choosing a suitable resonant frequency, we calculate the output angle as a function of the resonant frequency. This output angle is given by:

$$\theta = \frac{\lambda_0 f_0}{2 n_z V_{ZnO}} [ e \sqrt{A} \sin(d\sqrt{A}) - \frac{n_z}{n_0} \cos(d\sqrt{A}) ] \quad (34)$$

Figure 5 shows the output angle as a function of the resonant frequency for different values of the working distance. It can be seen that whatever the frequency is, and for a wide range of working distances, the output angle remains small, and therefore, the coupling losses due to an angular misalignment are low (figure 3). According to a transducer length equal to 1.15 mm, we choose to use a working distance equal to 2 mm, leading to the following device characteristics.

- resonant frequency	$f_0 = 666 \text{ MHz}$
- acoustic wavelength	$\Lambda = 7.96 \text{ } \mu\text{m}$
- transducer thickness	$d = 3.98 \text{ } \mu\text{m}$
- Bragg angle	$\theta_0 = 16.5 \text{ mrad}$

### V-3 Problem due to the beam diameter at the output face of the device.

We have established in the last section that the only possibility of having a suitable output fibres separation is to use an asymmetric AOM. We have seen that choosing a working distance of about 2 mm leads to a relatively low output angle corresponding to low coupling losses. But we have also to examine the influence of the optical beam diameter on these coupling losses. The beam diameter can be calculated by using the ABCD law.

Figure 6 shows the evolution of the beam diameter at the input face of the output fibres as a function of the working distance. It can be seen that the output beam diameter is of the order of few tens of  $\mu\text{m}$ . Therefore, the coupling losses will be very high (few tens of dB).



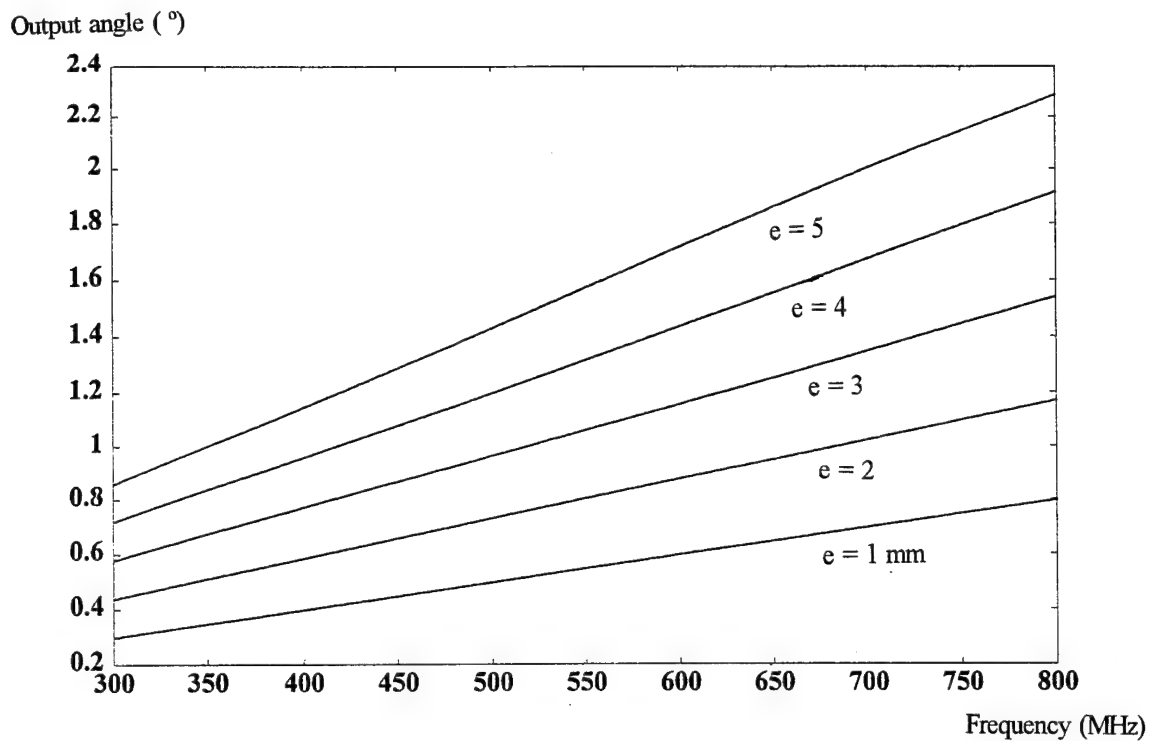


Figure 5: Output angle as a function of the resonant frequency for different values of the working distance

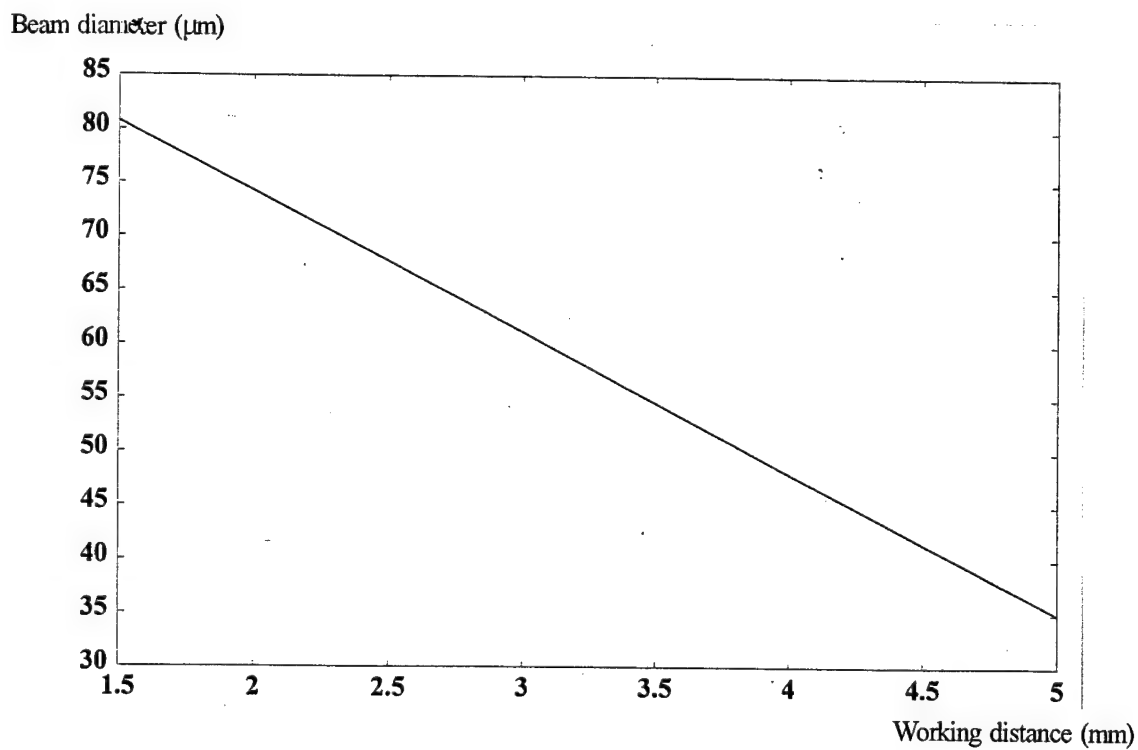


Figure 6: Optical beam diameter as a function of the working distance

#### V-4 Conclusion

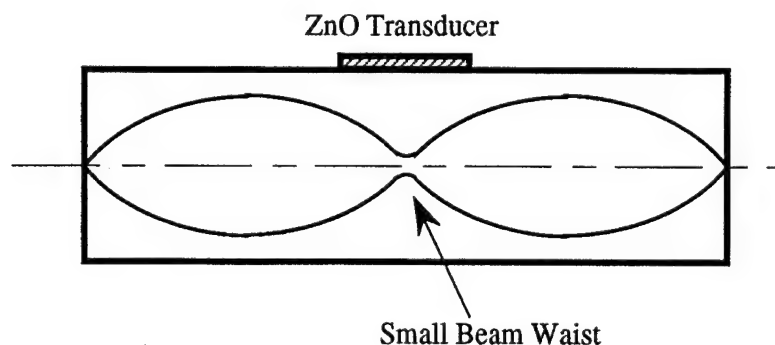
We have presented a very efficient device involving an asymmetric and transversally curved  $\text{TeO}_2$  acoustooptic modulator. The expected rise time is less than 5 ns, while the 100% power is about 1.22 Watts. The main interest of this AOM configuration is that no compromise is needed for diffraction and electric impedance matching. Unfortunately, the diameters of the output optical beams are too large to keep the coupling losses at a low value. Nevertheless, since the device is compatible with fibre technology, it is possible to use an in fibre optical-amplifier to overcome that problem.

An interesting application of this device is the Q-switching of fibre lasers. The optical coupling at the output face of the device can be improved by using a symmetric configuration with only one fibre attached to the end of the device. Then, there are two possibilities to switch the gain of the laser cavity. Either to place the output fibre so as to intercept the direct beam (the laser will operate in the 0 order) or to place it on the diffracted beam (the laser will then operate in the -1 order).

#### VI ONE PITCH LENS DEVICE - THE ACOUSTOOPTIC FREQUENCY SHIFTER

The previous sections have presented different fibre-compatible acoustooptic switcher-connectors. In particular, it appeared that the cylindrical geometry leads to a low 100% power only when the optical beam diameter is small compared to the device radius. Another interesting consequence of having a small optical beam diameter is the possibility to obtain very low rise times, leading to very high switching rates.

A way to obtain very a small optical beam diameter at the interaction region (*i.e.* centre of the device to reduce the optical coupling losses), consists of using a one pitch graded index device in which the optical beam is focused at the lens centre as illustrated below.



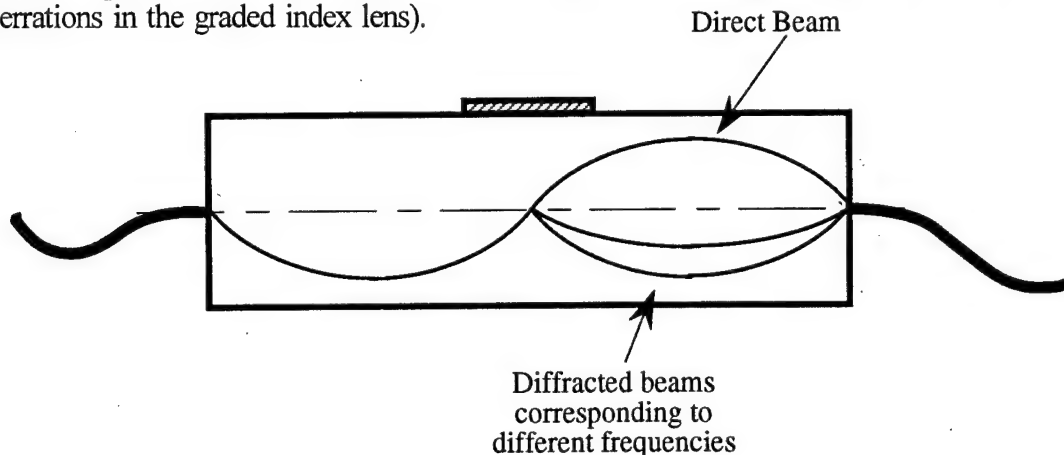
At the lens centre, the optical beam half diameter is of  $1.84 \mu\text{m}$ , leading to a rise time of 0.5 ns. The transducers dimensions will have to be determined by choosing a compromise between different quantities. Unfortunately such a 1 pitch device is unable to function as a switcher-

connector. The reason is that in a 1 pitch graded index lens, the position and angle of the optical beam at the centre of the lens (subscripts 1) and at the output face (subscripts 2) are related to the position and angle of the optical beam at the input face of the lens (subscripts 0) by:

$$\begin{aligned} x_1 &= -x_0 & x_2 &= x_0 \\ \alpha_1 &= -\alpha_0 & \alpha_2 &= \alpha_0 \end{aligned} \quad (35)$$

Therefore, the condition for the optical beam to be incident with the Bragg angle at the interaction region is to place the input fibre on the lens axis, and to angled that fibre (by polishing it) at the Bragg angle. As a result, the diffracted beam will be focused at the same point that the direct beam at the output face of the lens, *i.e.* the lens axis.

Equations (35) clearly show that it is impossible to build an acoustooptic switcher-connector by using a 1 pitch graded index lens. Nevertheless, since the output position of the diffracted beam does not depend on the acoustic frequency (*i.e.* the diffraction angle), this device can be used as an efficient fibre-compatible acoustooptic frequency shifter. The main interest of such a frequency shifter is that the frequency shifted diffracted beam is focused directly on the output fibre, regardless of the applied frequency (see figure below). Of course, the optical coupling losses will vary with the applied frequency, but since the maximum angle variation allowed by the - 3 dB bandwidth of the transducer (few hundreds of MHz) is low (less than 5 degrees) the optical coupling losses will remain at a relatively low value (neglecting the problem of optical aberrations in the graded index lens).



Estimations of the performances of this 1 pitch device which are not detailed here lead to the following characteristics.

Resonant frequency:	400 MHz
Transducer geometry:	cylindrical
Transducer length:	0.37 mm
Transducer width:	0.5 mm
Conversion efficiency:	25.6 % for 1 W applied
Conversion time:	0.5 ns
Bandwidth:	few hundreds of MHz

## VII CONCLUSION

We have presented theoretical studies of different acoustooptic frequency shifter switcher-connector devices. Transducer geometries and modulator configurations have been studied for all the different cases we have taken into account. Important results concern the geometry criterion that define whether the planar or the cylindrical geometry has to be used, the design of two devices that can be used for different applications.

In section I, we have studied a simple device involving only a half pitch graded index lens. Since the optical beam diameter is large at the interaction region, the rise time is relatively high. The 100% power is large too, due to the low  $M_2$  figure of merit of borosilicate glasses.

In section II, we have compared the available acoustic power at the interaction region to determine a criterion suggesting what kind of transducer geometry leads to the higher diffraction efficiency. This criterion is a function of the modulator radius, the acoustic wavelength, and the optical beam diameter. It must be noted that the criterion is valuable only if the electric impedances and acoustooptic matchings are the same for both geometries. If not, it will be necessary to take into account the different compromises that will have been made when designing the devices.

In section III, we have compared the 100% acoustic power for both geometries in the case of the half pitch device. It appeared that the cylindrical geometry leads to a lower 100% power, even if the geometry criterion indicates the contrary. This is due to the compromises we made, which are different for both geometries.

We have presented a device involving a high  $M_2$  figure of merit acoustooptic modulator in section IV. The use of a  $\text{TeO}_2$  modulator inserted between two 0.25 pitch graded index lenses leads to a lower 100% power. But the rise time is still large.

In section V, we propose the use of 0.29 pitch graded index lenses to reduce the beam diameter and hence the rise time. The 100% power is also greatly reduced by using an asymmetric configuration, in spite of large optical coupling losses. The main interest is that no compromise is needed when considering a transversally curved transducer.

Finally, we have quickly presented a one pitch graded index devices that can be used as an efficient frequency shifter. The interest of the method is that the frequency shifted diffracted beams are always focused on the lens symmetry axis regardless of the applied acoustic frequency. As a result, this fibre-compatible frequency shifter leads to relatively constant optical coupling losses only due to the frequency dependent output angle.

The main conclusion of these theoretical studies is that low coupling losses can be obtained by using a half pitch graded index AOM, but both rise time and applied acoustic power are high. To reduce the applied acoustic power, a high figure of merit material is needed. Therefore, the rise time can be greatly reduced by using 0.29 pitch graded index lenses. The following table summarize the characteristics of the different devices we have considered.

DEVICE (frequency)	CONFIGURATION	RISE TIME	100% POWER	COUPLING LOSSES
1/2 pitch graded index lens (400 MHz)	Cylindrical	43.8 ns	8.8 W	1.78 dB
TeO <sub>2</sub> 1/4 pitch graded index lens (400 MHz)	Cylindrical	43.8 ns	4.9 W	2.13 dB
Asymmetric TeO <sub>2</sub> (666 MHz)	long. Planar trans. Curved	< 5 ns	1.22 W	few tens

## REFERENCES

### PART I

- [1] A. Yariv, and Y. Pochi, *Optical waves in crystals : propagation and control of laser radiation*, Wiley, New-York, 1984
- [2] H. Kogelnick, T. Li, "Laser beams resonators", *Applied Optics*, Vol. 5, N° 10, 1966
- [3] M.G. Cohen, E.I. Gordon, "Focusing of microwave acoustic beams", *Journal of Applied Physics*, Vol. 38, N° 5, 1967
- [4] D. Maydan, "Acoustooptical pulse modulators", *IEEE Journal of Quantum Electronics*, Vol. QE-6, N° 1, 1970
- [5] E.H. Young Jr, S. K. Yao, "Design considerations for acousto-optic devices", *Proceedings of the IEEE*, Vol. 69, N° 1, 1981
- [6] M. Saruwatari, K. Nawata, "Semiconductor laser to single mode fiber coupler", *Applied Optics*, Vol. 18, N° 11, 1979

## PART II

### PIEZOELECTRIC THIN FILMS

#### Deposition and evaluation

In this part, we will discuss experimental studies that have been carried out on the deposition of piezoelectric thin films and the equipment which has been constructed for film characterisation.

Further on, we present studies which have been carried out to increase our understanding of the process of making high frequency zinc oxide piezoelectric transducers to the point that they can be manufactured on a routine basis. As previously stated in part I, we choose to use zinc oxide piezoelectric transducers because of their large electromechanical coupling constant. Zinc oxide films deposited by RF planar magnetron sputtering has been shown to be preferable to lithium niobate for acoustic transducers of high resonant frequency ( $>0.5$  GHz). For reasons that have been discussed in part I, it is preferable to operate our proposed devices at frequencies of several hundred MHz and above, making ZnO the most attractive option. An added advantage of sputtered ZnO is that it can be applied to non planar substrates and in particular to the cylindrical surfaces we described earlier.

We have carried out a large number of sputtering runs to established the optimum conditions for growth of ZnO films. This is not an unresearched field in that a lot of ZnO deposition has been done by various groups in the past, particularly at NRL and Stanford. However, many of the problems hindering the deposition of reproducible films remain unsolved (as manifested by the lack of commercial acoustooptic products employing these highly desirable transducers) and the extraction of any "universal" behaviour from the large amount of experimental data has not been highly developed. We are characterising the films using a number of techniques:

- X-ray analysis using a texture camera
- Scanning Electron Microscopy (SEM)
- In-situ optical monitoring of film growth

We will now discuss the production of highly oriented ZnO film and the thin film evaluation techniques we employ.

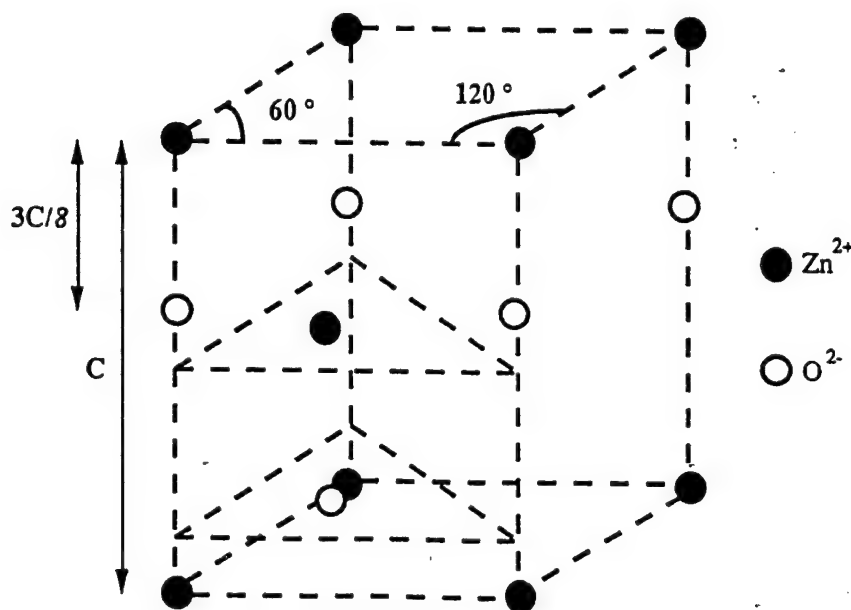
## I ZINC OXIDE THIN FILMS - THE MECHANISMS OF SPUTTERING.

As previously stated, the large electromechanical coupling constant of ZnO has commended it for the fabrication of piezoelectric transducers. It can be used for both bulk and surface waves generation. To date, a wide range of deposition techniques have been investigated. ZnO thin films have been grown by chemical vapour deposition [1], spray pyrolysis [2], reactive evaporation [3], and DC reactive sputtering [4].

In the work presented here, we use reactive RF planar magnetron sputtering because this deposition technique is capable of sustaining film stoichiometry and crystallographic orientation regardless of the substrate.

### I-1 The Zinc Oxide crystal.

Zinc Oxide belongs to the Würtzite type hexagonal system, with a 6mm symmetry. It can be considered as two close packed structures, one of zinc atoms and the other of oxygen atoms, which are  $3/8$   $c$  apart from each other, where  $c$  is the height of the three dimensional lattice. The figure below shows the crystal lattice of ZnO.





Due to its asymmetric structure, ZnO is a piezoelectric material. Adjacent atoms of Zn and O will move differently in an electric field applied parallel to the c axis. Therefore, the dimensions of the lattice (i.e. the material) will change, allowing the material to generate acoustic waves. Conversely, an electric field is induced when the material is strained.

In the ideal case where each elementary individual crystal deposited on the substrate has its c axis aligned normal to the surface, longitudinal acoustic waves can be produced, in which the particle motion in the acoustic medium is only in the direction of propagation. It is then possible to make highly efficient ZnO piezoelectric transducers by placing the film between two metal electrodes.

### I-2 The mechanism of sputtering.

Sputtering process is based on the interaction of highly energetic ions with target material.

When an ion strikes the surface of a solid, several phenomena may occur. The ion may be reflected, it can cause the target to eject an electron, it may become buried in the target (this phenomenon is called *ion implantation*), or it can cause a rearrangement in the target, which leads to the ejection of one of the target atoms. This ejection process is known as sputtering. The sputtering process is very often compared to the break in a billiard game (see figure below).



In that game, the "cue ball" (the bombarding ion) strikes the well arranged pack (the atomic structure of the target), scattering atoms target in all directions, including out of the target. These ejected atoms can move through space until they strike and condense on the surface of a receiver, which we arrange to be our substrate. By repeating the process over and over, a coating of many atomic or molecular layers of target material gradually grows on the substrate surface. The real process is of course rather different from the billiard game, but this model is not too unrealistic.

Ions are normally used as bombarding particles since they can be accelerated by an electric field. The series of collisions at the surface is known as a collision cascade. Of course, it is a matter

of luck whether this cascade leads to the sputter ejection of an atom from the target surface, or heads off into the interior of the target, dissipating the energy of the primary impact into lattice vibration. It is estimated that 1% of the incident energy goes into ejection of sputtered atoms. Rates of deposition are typically a few microns per hour, depending on the sputtering parameters.

The atoms that leave the target are able to travel to the substrate because both the target and the substrate are contained in a vacuum system where the number of gas molecules is suitably low. A large number of fast atomic sized particles bombarding the target is obtained by immersing the target in a plasma containing ions and electrons and by applying a high negative voltage to the target surface, which attracts the ions from the plasma to the target.

### I-3 Description of the RF reactive sputtering system.

Figure 1 shows a view of the RF planar magnetron sputtering equipment (Nordiko) we used in this project. The schematic of the system is shown in figure 2. A 20 cm diameter, 99.99% pure Zn target (supplied by Cesac) is the cathode of an electrical circuit, and has a high negative voltage applied to it. The substrate to be coated is placed on an electrically grounded anode a few centimetres away. These electrodes are housed in a vacuum chamber which is evacuated before deposition.

The pumping arrangement (consisting of a mechanical and a cryogenic pump) associated with the RF sputtering system performs two functions; to remove unwanted gases by pumping the chamber to a sufficiently low pressure (typically between  $10^{-6}$  and  $10^{-7}$  mbar) and to maintain the vacuum chamber at a pressure around  $10^{-2}$  mbar during the sputtering process, while the sputtering gas is continually bled through the chamber.

The target is surrounded by a ground shield, which restricts ion bombardment and sputtering to the target only. The target has to be cooled, because sputtering is a very inefficient process, and a large amount of the power input to the system is dissipated in target heating. Hence, the Zn target is indium bonded to a thick copper backing plate (which aids to maintain an uniform temperature across the target surface) and is screwed onto a water cooled electrode. Heat sink compound is also put between the backing plate and the electrode to improve cooling.

The substrate temperature influences the formation stage of the film and its final structure, and so must be controlled during deposition. The heat provides surface mobility after the atoms are deposited so that they reach the lowest thermodynamically favoured lattice positions. Heating of the substrate holder is achieved by electrical resistance heating. The temperature is measured and controlled with a thermocouple, fitted with an RF filter to remove RF components.

Figure 2 shows a shutter, that can be rotated into place between the target and the substrate. It is used during the presputtering period when the first few atomic layers of the target are removed by sputtering to clean it. When the system is opened to air, the target becomes contaminated by atmospheric pollution, by handling, or by chemical combination with the atmosphere to form oxide. This shutter prevents deposition on the substrate during the presputter cleaning. It is also used to stop the deposition at the end of the process.

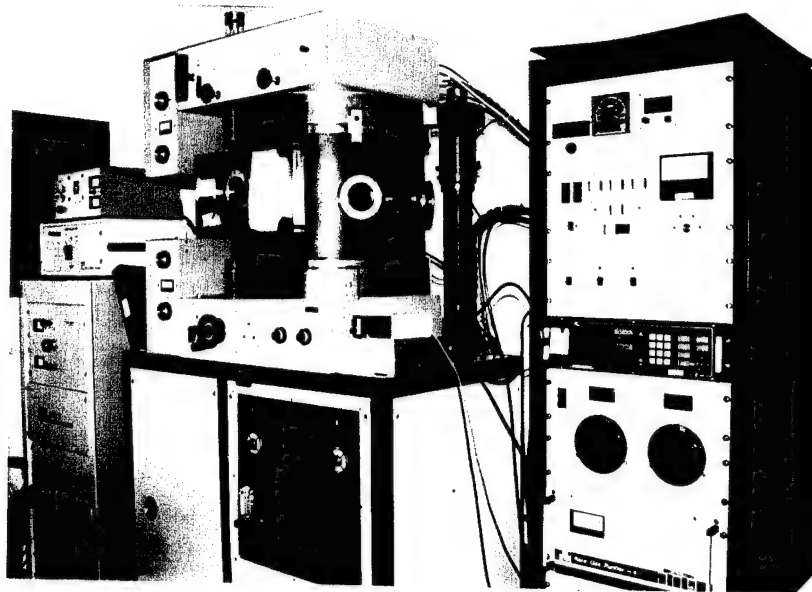


Figure 1: Photograph of the Nordiko RF planar magnetron sputtering system

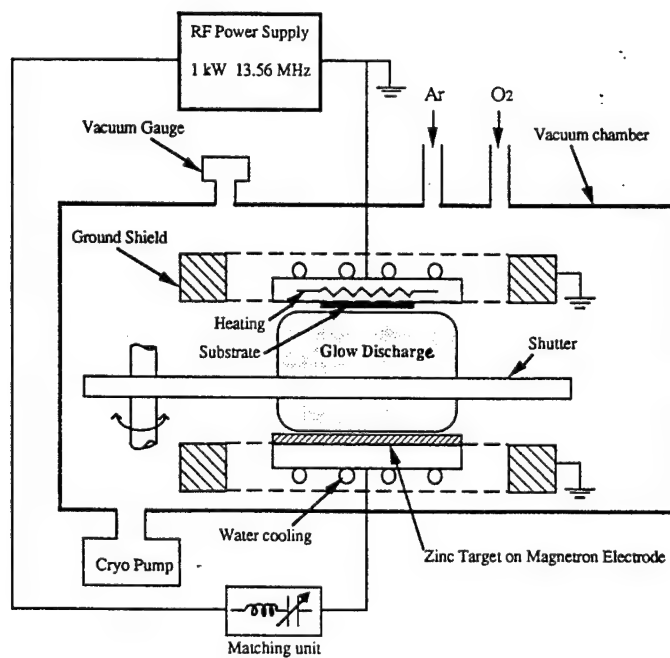


Figure 2: Schematic diagram of RF planar magnetron sputtering system

The cathode is fitted with a magnetron, which concentrates the plasma glow. A magnetic field normal to the target constrains electrons to follow a helical rather than straight-line path. This gives electrons a longer path length and increases the probability of ionizing collisions before the electrons reach the anode. Since the output impedance of the RF generator must be held constant (any impedance mismatch causes an important part of the incident RF power to be reflected back towards the supply and dissipated), and since the glow discharge impedance is much higher than of the RF generator, a tunable matching unit is situated close to the target assembly.

The controllable parameters during deposition are the RF power, the substrate temperature, and the sputtering gas pressure and composition.

Argon is introduced in the chamber to provide a medium in which a glow discharge can be initiated and maintained. The electric field accelerates electrons which collide with argon atoms, breaking some of them into argon ions and more electrons to sustain the glow discharge. The charged particles thus produced are accelerated by the electric field, the electrons tending toward the anode (causing more ionization on the way) and the ions toward the cathode, causing sputtering of the target. The atoms sputtered from the target diffuse in random directions, some of them landing on the substrate to form the thin film.

In the case of ZnO deposition from a pure Zn target, an active gas, oxygen, must be admitted into the chamber together with the sputtering gas, argon. During deposition, the oxygen combines chemically with sputtered Zn atoms to form the compound ZnO in a process now called reactive sputtering.

## II INFLUENCE OF THE SPUTTERING PARAMETERS.

In part I, we have seen that the different devices we can build involving ZnO piezoelectric transducers are greatly sensitive to the control of the resonant frequency, which is a sensitive function of the film thickness. Therefore, it is very important to evaluate the influence of the deposition parameters on the deposition rate, so that the film thickness can be accurately controlled.

To obtain efficient piezoelectric films, it is important that their "c" axis (height of the three-dimensional lattice) are normal to the substrate surface. It is therefore important to study the influence of the deposition parameters on the film structure.

To summarize, the purpose of the experimental work concerning the deposition of thin ZnO film, is to study the influence of the deposition parameters to increase the reproducibility of the film, which is still a crucial problem for building high quality AOMs involving ZnO films. The next section presents the studies that have been carried out to improve our understanding of the sputtering process.

## II-1 Description of the experimental studies.

For each deposition run, we used three gold coated silicon samples. The first will be examined using a Scanning Electron Microscope (SEM) that provides informations on the morphology and the structure of the film. The second sample will be examined with the x-ray diffraction technique to determine the degree of "c" axis orientation (the x-ray analysis is being done in collaboration with staff at Cranfield University). One major parameter which cannot easily be measured by x-ray techniques is the degree of c-axis reversal, which should ideally be small in order to obtain highly active films. In order to investigate this, we plan to exploit the link between pyroelectric and piezoelectric activity, and to measure the pyroelectric activity of the third sample using the techniques developed by Professor Pitt of the ORC [5].

The deposition runs were carried out as follow:

The substrates were cleaned using ultrasonic agitation at 50 °C in Liquid Laboratory Cleaner Micro (30 minutes), acetone (30 minutes), and isopropyl alcohol (30 minutes), and dried in a 120°C oven for 15 minutes. This cleaning process is of great importance. All the dust particles must be removed, because they act as nucleation points during the ZnO sputtering process, that modify the surface quality and consequently the film structure.

The substrates were mounted on a substrate holder and put in the vacuum chamber. Pumpdown was initiated to reduce the chamber pressure to less than  $10^{-6}$  mbar, before the substrate heating and rare gas purifier were turned on.

When the substrate temperature had stabilized, oxygen and argon were admitted into the chamber to the required plasma pressures.

The shutter was then closed and the target cleaned by presputtering for few minutes. This presputtering is of great importance since any contaminants on the target surface can be deposited on the sample surface and start nucleation points. Figure 3 shows example of these particles after they have landed on the substrate surface. We also can see that sometimes they can be removed from the surface, and that these particles influence the surface structure. These pictures have been obtained by using a SEM, with magnitudes 6000 and 9500.

The film deposition was started by opening the shutter and rematching the RF power input

The deposition parameters that have been carefully controlled are the input RF power, the sputtering gas pressures, and the substrate temperature. The following table gives the detail of the deposition parameters we used for the few first samples.

WAFER	RUN	SAMPLE	Bottom EI.	Top EI.	RF Power	Temp. (C)	Ar (mT)	O2 (mT)	RATE
1	1	1	Cr/Au (100 nm)	Al (100 nm)	450	300	8	1.5	19.92
-	-	2	-	none	450	300	8	1.5	19.92
-	-	3	-	none	450	300	8	1.5	19.92
-	2	4	-	none	400	300	8	1.5	14
-	-	5	-	none	400	300	8	1.5	14
-	-	6	-	Al (100 nm)	400	300	8	1.5	14
-	-	7	-	none	350	300	8	1.5	11.58
-	3	8	-	Al (100 nm)	350	300	8	1.5	11.58
-	-	9	-	none	350	300	8	1.5	11.58
-	4	10	-	none	500	300	8	1.5	20.36
-	-	11	-	none	500	300	8	1.5	20.36
-	-	12	-	Al (100 nm)	500	300	8	1.5	20.36
2	5	13	-	Cr/Au (100 nm)	350	300	8	1.5	11.11
-	-	14	-	Cr/Au (100 nm)	350	300	8	1.5	11.11
-	6	15	-	none	350	300	10	1.875	11.54
-	-	16	-	Cr/Au (100 nm)	350	300	10	1.875	11.54
-	-	17	-	none	350	300	10	1.875	11.54
-	7	18	-	none	350	300	20	3.75	9.3
-	-	19	-	none	350	300	20	3.75	9.3
-	-	20	-	none	350	300	20	3.75	9.3
-	8	21	-	none	350	300	12	2.25	11.54
-	-	22	-	none	350	300	12	2.25	13.15
-	-	23	-	none	350	300	12	2.25	12.42
-	9	24	-	none	350	300	12	2.25	11.37
-	-	25	-	none	350	300	12	2.25	11.76
-	-	26	-	none	350	300	12	2.25	11.78

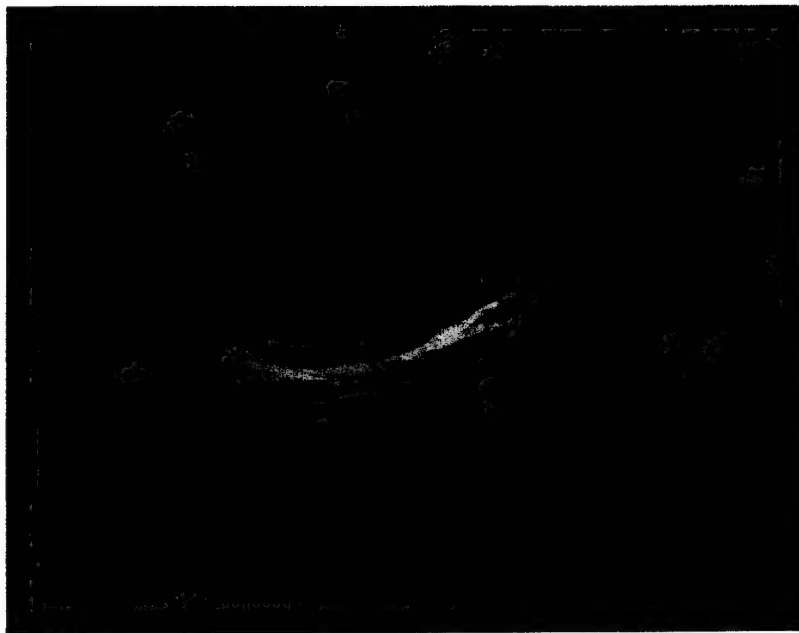
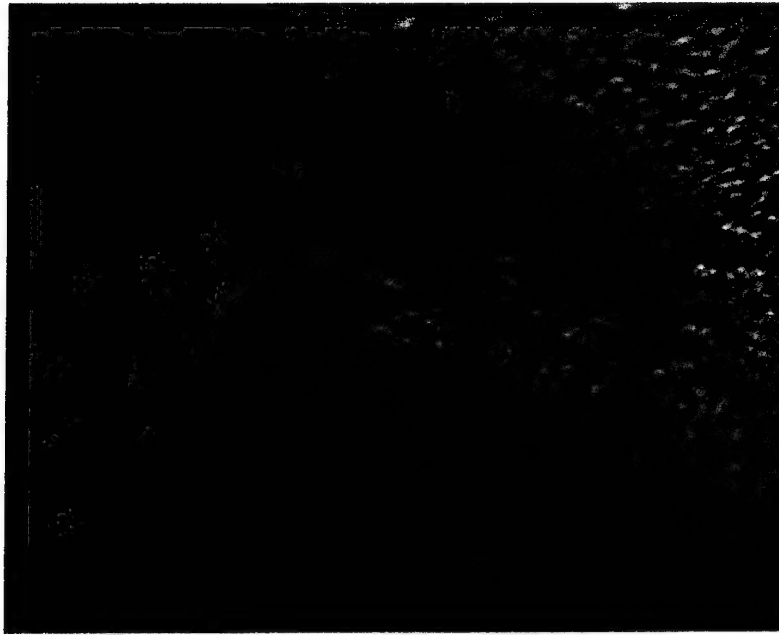


Figure 3: Effect of dust particles sputtered on the substrate

## II-2 Influence of RF power on deposition rate.

As previously stated, it is important to accurately control the deposition rate in order to increase the reproducibility of the films. This control is also important because the film thickness is directly related to the resonant frequency which is a key point for acoustooptic modulators.

Since thin films grown by RF sputtering are formed by atoms that have been ejected from the target, the energy of the bombarding particles is directly related to the number of Zn atoms landing on the substrate surface. The energy of the bombarding particles can be controlled by varying the input RF power.

The Nordiko sputtering equipment we use for ZnO deposition provides RF powers of up to 1000 Watts. Deposition runs have been carried out with powers varying from 350 to 500 Watts. It has been noted that the glow discharge is more difficult to initiate when using an RF power lower than 350 Watts, depending, of course, on the sputtering gas pressure. Around that threshold, the plasma is less homogeneous, and the energy distribution in the glow discharge region varies randomly. In contrast, an RF power higher than 500 Watts can result in excessive target heating. Since we did not want to thermally damage the Zn target, we never exceeded 500 Watts input power.

We also think that a lower deposition rate allows the deposited particles more time to reach the lowest thermodynamically favoured lattice positions (this can also be achieved by increasing the substrate temperature which results in a higher surface mobility).

Nevertheless, it has been shown [6] that the density of reactive species in the vicinity of the cathode (the Zn target) is reduced at higher discharge power, but the velocity of the species is increased. Therefore, contamination of the target with reactive species can be reduced by using a higher RF power, which will also improve the probability of collision (via the increased velocity), leading to a higher deposition rate. Consequently, we have chosen the compromise of using RF powers in the range 350-500 Watts.

During the first set of deposition runs, the other parameters were kept constant.

Substrate temperature:	300 °C
Ar pressure:	8 mTor
O <sub>2</sub> pressure:	1.5 mTor

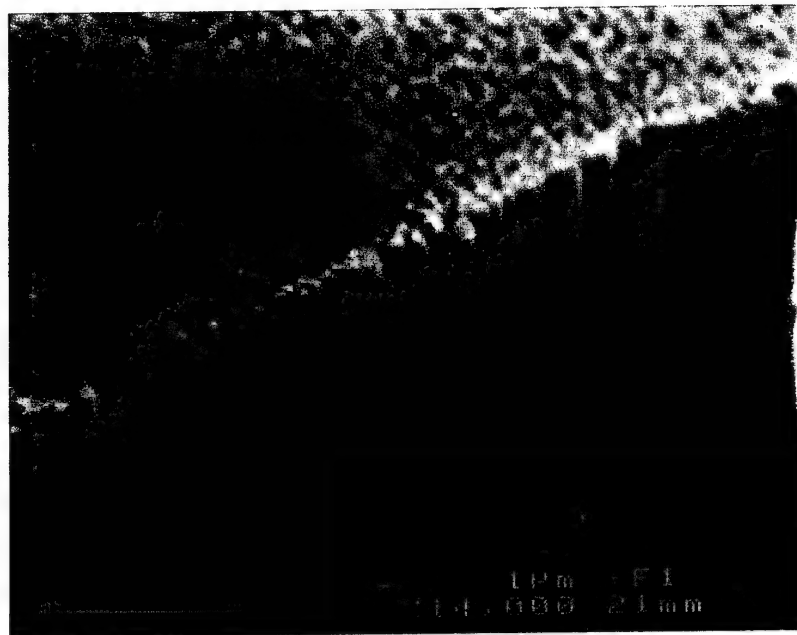
and we monitored the deposition rate as a function of the input RF power, as shown in the following diagram.

The deposition rate varies from 10 to 21 nm/mn while the input RF power increases from 350 to 500 Watts. It must be noted that the increase of the deposition rate at high powers points out the importance of a good stability of the power supply as well as a close control of the substrate temperature as we will see in further sections. The films that have been obtained during these first few runs all exhibit a hexagonal columnar structure as it can be seen from figure 4.

Figure 4-a shows a SEM picture of a film grown by using an RF input power of 350 Watts. The crystallites (columns) are all well oriented, and they are constant in form and dimensions.



a)

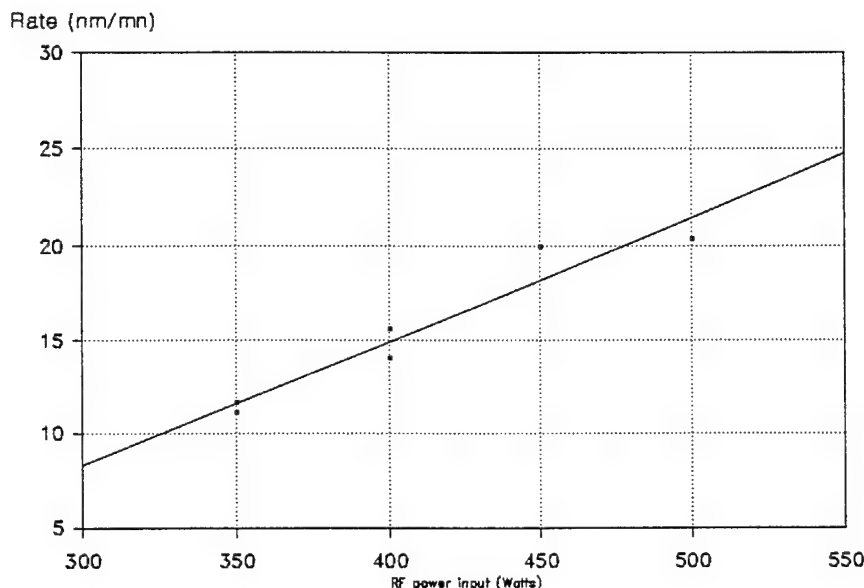


b)



Figure 4: SEM picture of ZnO sputtered films

- a) Film obtained with an RF power equal to 350 Watts
- b) Amorphous layer



In figure 4-b, we can see an amorphous layer at the beginning of the film. This amorphous layer can be attributed to several factors. Firstly, the sputtering condition are not the same at the beginning of the film growth. This is because the neighbourhood of the sputtered species is different at the beginning. During deposition of the initial layer, atomic interactions occur between the substrate lattice and the sputtered species, while there are only interactions between sputtered species after the first atomic layers have been deposited. However, we think that the most important reason for this amorphous layer is due to the non constant substrate temperature at the beginning of the process, leading to a varying surface mobility, and thus to a change in film structure (see the section concerning temperature calibration).

As previously stated, all the films grown in the first few deposition runs exhibit a well oriented structure. X-ray analysis of the films has confirmed the SEM results. We therefore conclude that the best films those obtained using 350 Watts input RF power. We will then used this RF power examining the influence of the sputtering gas pressure on the film quality.

### II-3 Influence of sputtering gas pressure.

Sputtering gas pressure is another important parameter to study in order to grow high quality ZnO films. The argon pressure is directly related to the number of zinc atoms that can be ejected from the target. In order to grow films exhibiting a suitable stoichiometry, it is important that the amount of oxygen atoms in the vicinity of the substrate surface is greater than or equal to

the amount of sputtered zinc atoms landing on the substrate. Previous research carried out in the ORC have shown that good results are obtained by using a ratio of about 85% of argon to 15% of oxygen.

Another important phenomenon occurs as result of the oxygen pressure [7]. Oxygen reduces electron bombardment of the substrate by acting as an electron trapping medium in the plasma. It is advantageous for the substrate, but, at the same time, it reduces the sputtering yield from the target, thereby reducing the deposition rate. Furthermore, high oxygen pressure results in oxygen atoms being absorbed by the target, which further reduces the deposition rate.

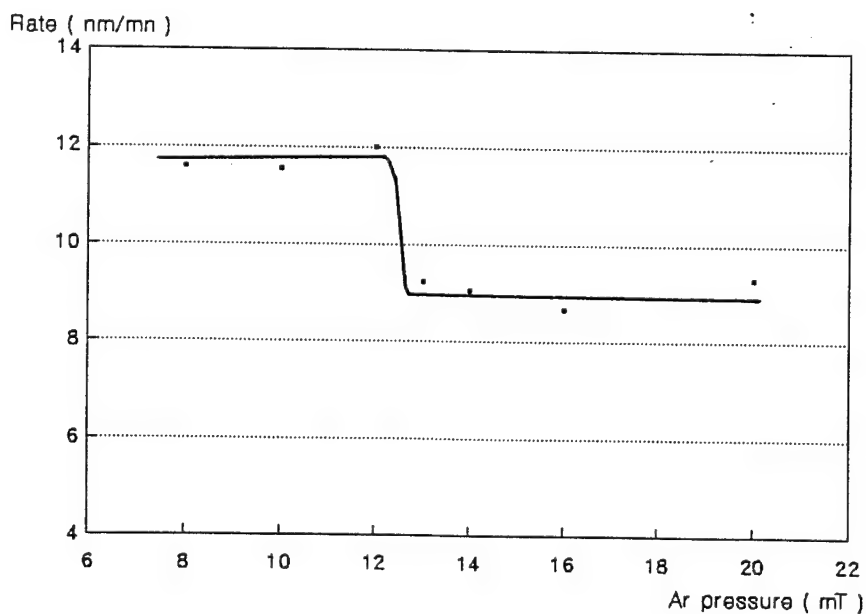
During our experiments, we have also noted that when the oxygen pressure is too high, some ZnO powder is deposited on the target surface. Those small grains are then broken by the plasma, and sputtered toward the substrate surface causing the defects shown in figure 3.

Some workers have reported the existence of a threshold in the deposition rate versus the argon pressure. It is said that films grown with rates just below or just above that threshold are of better quality than the others.

For this second set of runs, the argon pressure has been increased from 8 mTor to 20 mTor, keeping the ratio 85% argon / 15% oxygen and the other parameters constant.

Substrate temperature: 300 °C  
Input RF power: 350 W.

The curve below shows the deposition rate as a function of the argon pressure, illustrated that we too observe a threshold, at an argon pressure of 12.5 mTor.



According to SEM observations, the best films we had were grown with rates just below (10 mTor), and just above (16 mTor) *i.e.* either side of the threshold

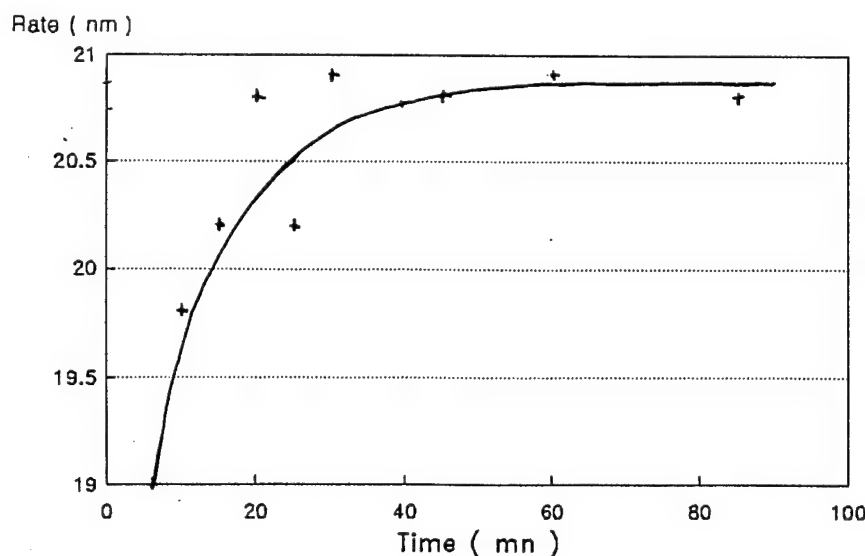
## II-4 Control of the substrate temperature

During all of the first runs, we noticed that the deposition rate was not constant during the first hour. This can be explained by considering that the film density varies during the deposition of the initial layers, as we will see in the next section. Another important problem we have noted in the deposited films is the existence of an amorphous layer at the interface between the substrate surface and the polycrystalline film. As aforementioned, the sputtered species see a different surrounding after a few atomic layers have been deposited. Since we have observed amorphous layers of a few hundreds of nanometres thick, the time over which this amorphous film evolves can be related to the time over which the substrate temperature is known to stabilise after deposition commences.

In the following section, we relate the film density to the deposition rate. This variation in density we have observed could also be related to the amorphous layer. The next section deals with the temperature control of the substrate. We will see that the temperature variation during the initial stage of the sputtering process can explain the variation in the structure of the initial layers.

### II-4-1 Evolution of the film density during the first hour of the deposition process.

During the first deposition runs, we noticed that the deposition rate varied during the first 50 mn. The following curve shows the evolution of the deposition rate over the first 90 mn.



The variation of the deposition rate can be related to a variation in the film density as follows. We consider an area  $S$  of the substrate surface. During the film growth, the increase in film volume is given by  $dV = S \times dh$ , where  $dh$  is the elementary increase in film thickness. Since the input RF power and the sputtering gas pressure are constant, we consider that the amount of zinc and oxygen in the vicinity of the substrate surface remains constant. We call  $\rho$ , and  $M$  the density and the mass of the film material. Let  $r_{ZnO}$  be the mass of zinc and oxygen atoms arriving on the substrate per unit of time. We have then  $r_{ZnO} = dM/dt$ . We call  $R$  the deposition rate, such that:

$$R = \frac{dh}{dt} = \frac{1}{S} \frac{dV}{dt} = \frac{1}{S} \frac{d}{dt} (M/\rho) = \frac{r_{ZnO}}{\rho S} - \frac{M}{\rho^2 S} \frac{d\rho}{dt} \quad (1)$$

The second relation we need involves the variation of the density with time. We have:

$$\rho = M/V = M/Sh \quad \Rightarrow \quad \frac{d\rho}{dt} = \frac{1}{S} \frac{d}{dt} (M/h) = \frac{r_{ZnO}}{Sh} - \frac{RM}{Sh^2} \quad (2)$$

Combining equations (1) and (2), we can write the deposition rate as a function of the density:

$$R = \frac{r_{ZnO} h}{\rho V + M} \quad (3)$$

And then, we calculate the variation of the deposition rate as a function of the variation of the density:

$$\frac{dR}{d\rho} = - \frac{r_{ZnO} h V}{(\rho V + M)^2} \quad (4)$$

Equation (4) shows that when the deposition rate increases, the density of the film decreases. We postulate that during the first 50 mn, the film consists of an amorphous layer whose density is higher than that of the polycrystalline film. This means that only the upper part of the film is polycrystalline ZnO, and that only this upper layer exhibits piezoelectric activity. Since the effective film is thinner, the resonant frequency is higher than expected, an effect we have previously observed at the ORC.

#### II-4-2 Control of the substrate temperature.

We have seen that the film structure varies during the first 50 mn of deposition, and we postulate that it is due to the substrate temperature which is not constant during the beginning of deposition. The exact substrate temperature has been checked by using a second type K thermocouple in contact with the copper plate on which the substrate is clipped. Two sets of interrogative experiments have been carried out.

##### *Substrate temperature and stabilization time without applied RF.*

Firstly, we measured the substrate temperature as a function of the set-point temperature. The result is shown on figure 5. It appears that the real substrate temperature is roughly equal to the of the set-point temperature. This is probably because the massive metallic structure that is around the heater absorbs a large amount of the available energy, and because the set-point thermocouple is located in the vicinity of the heater.

It has also to be noted that the stabilized temperature depends slightly on the initial chamber pressure. For example, with an initial pressure of about  $10^6$  mbar and a set-point temperature of 200 °C, the stabilized temperature is 102 °C. With an initial pressure of about  $5 \times 10^7$  mbar and the same set-point temperature, the stabilized temperature is about 98 °C.

Since the metallic structure around the heater absorbs a large amount of energy, the time needed for the substrate temperature to be stable is of the order of few hours. Figure 6 shows the stabilization time as a function of the set-point temperature. For set-up temperatures above 100 °C, the stabilization time varies linearly with the temperature.

##### *Effect of the applied RF power on the substrate temperature.*

The second experiment was carried out with a set-up temperature of 200 °C, corresponding to a real temperature equal to 102 °C. The admission of sputtering gases had almost no effect on the substrate temperature. In a first set of measurements, the substrate temperature decreased from 102 to 100 °C, but in a second set, the temperature remained constant.

After the admission of argon and oxygen to the chamber, the RF power was switched on, and set at 100 W, then 300 W, and finally 500 W. At each step, the temperature was measured as a function of time. Figure 7 shows the result. The discontinuities that can be observed when the RF power is changed are due to RF interferences between the RF generator and the thermocouple electronics. This is because the thermocouple is in contact with the RF circuit anode (the plate on which the substrate is clipped). Figure 8 shows the effect of RF power on the thermocouple reading. These measurements taken as quick as possible, before the substrate temperature increased. Then, we used this calibration curve to correct the curve shown in figure 7. Figure 9 shows the result.

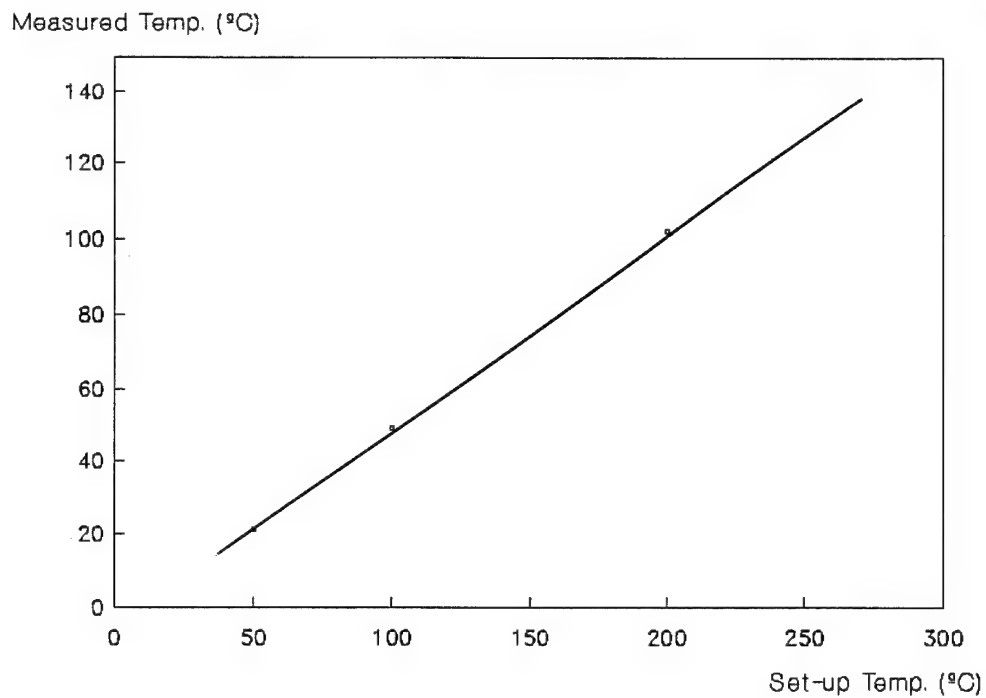


Figure 5: Measured temperature versus set-up temperature

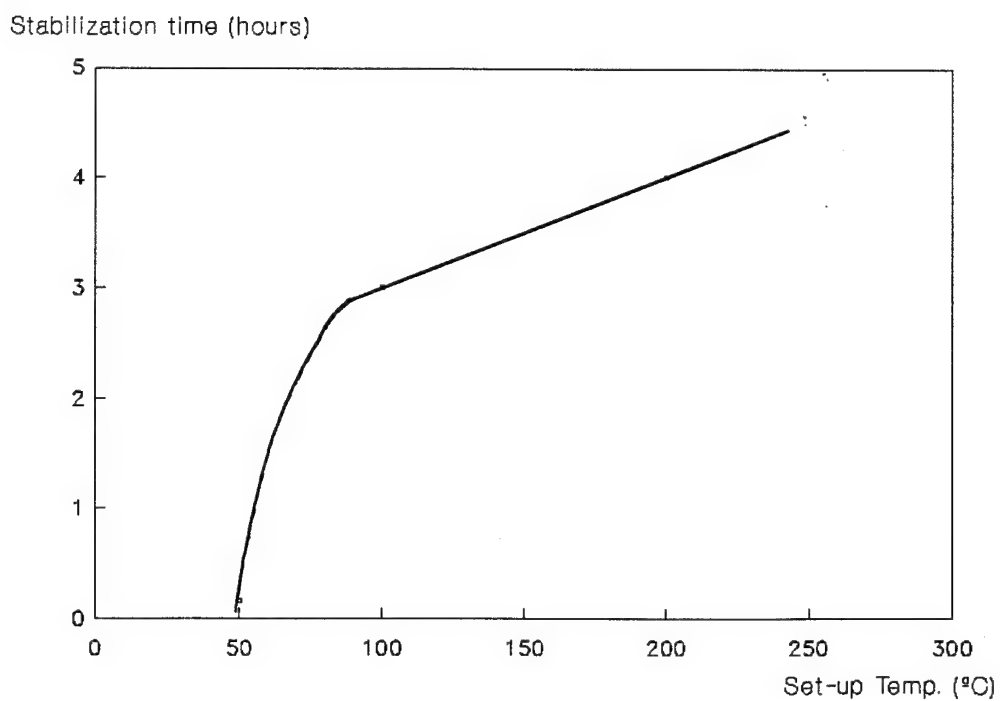


Figure 6: Stabilization time versus set-up temperature

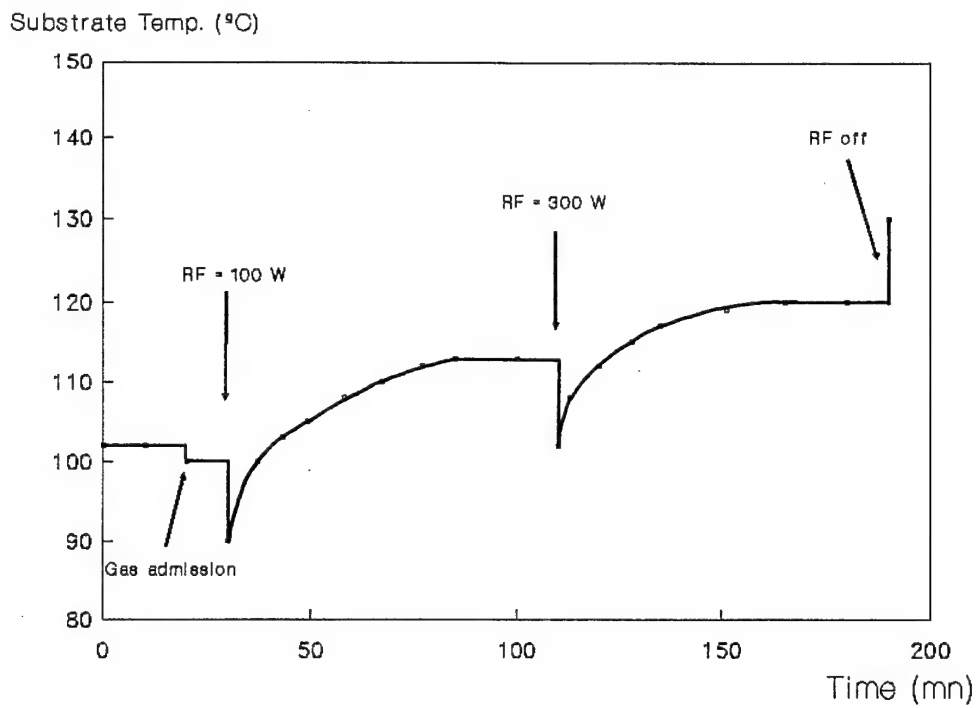


Figure 7: Substrate temperature versus time when changing the input RF power

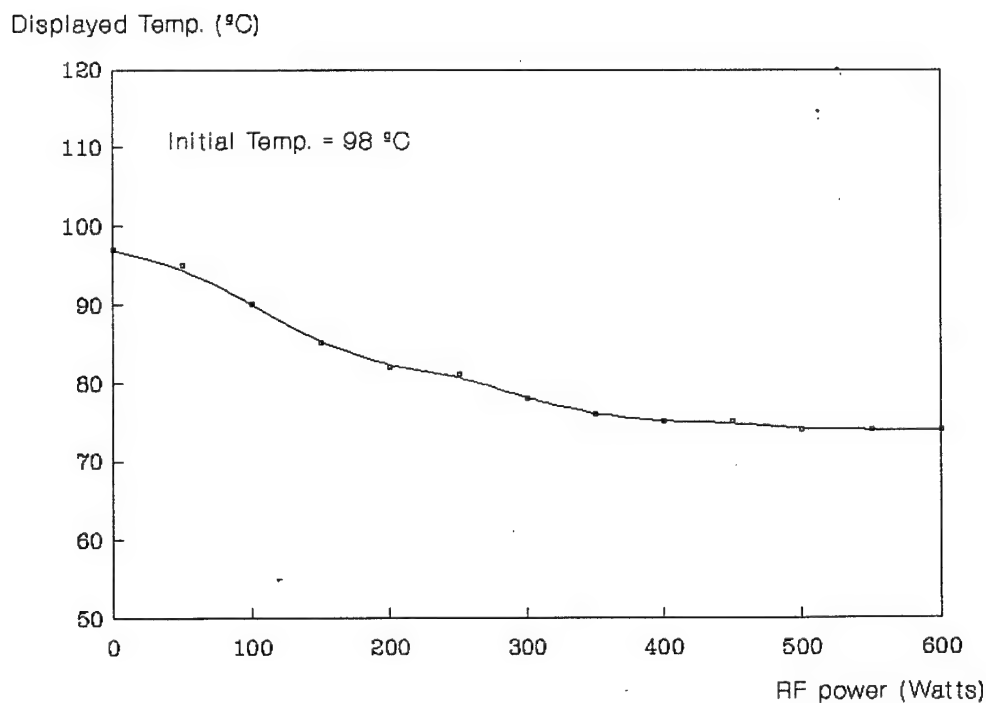


Figure 8: Effect of RF interferences on the thermocouple indication



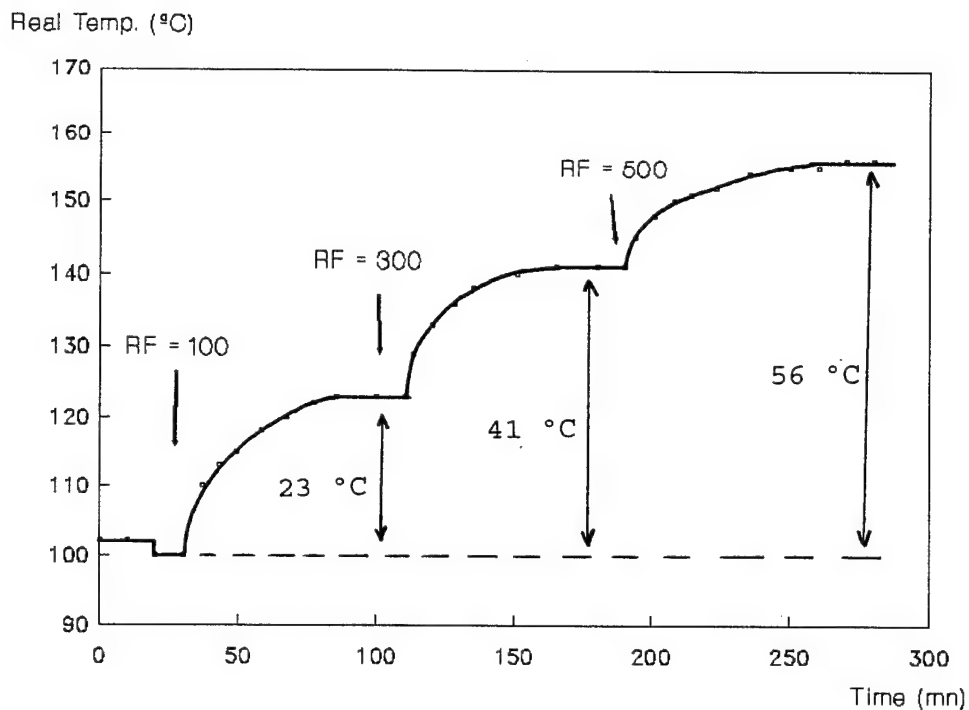


Figure 9: Calibrated curve showing the effect of plasma heating.

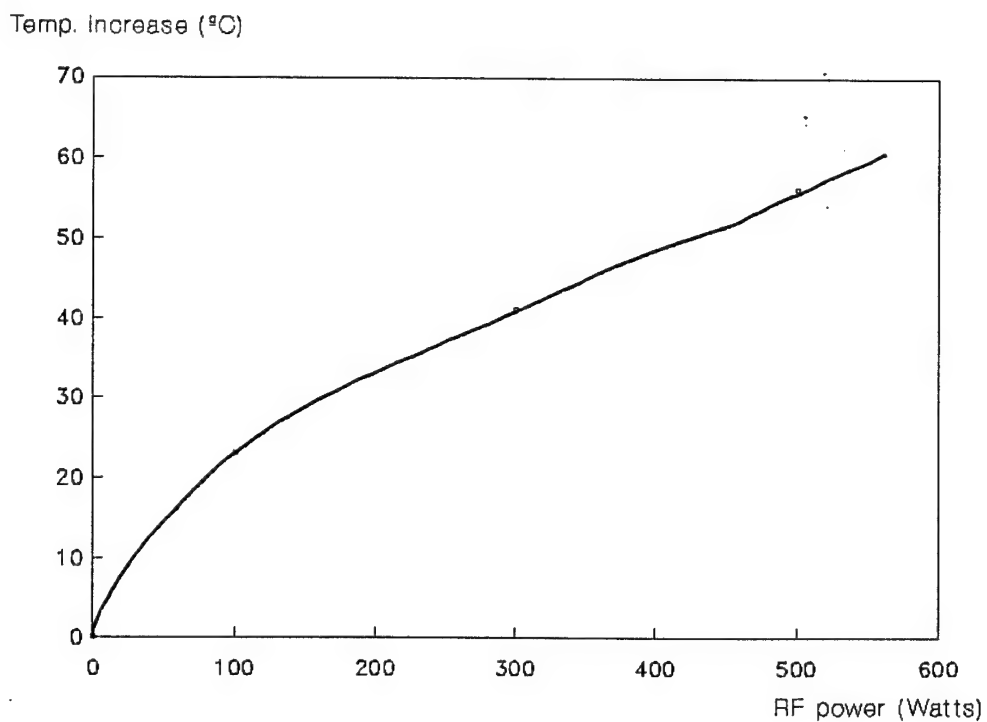


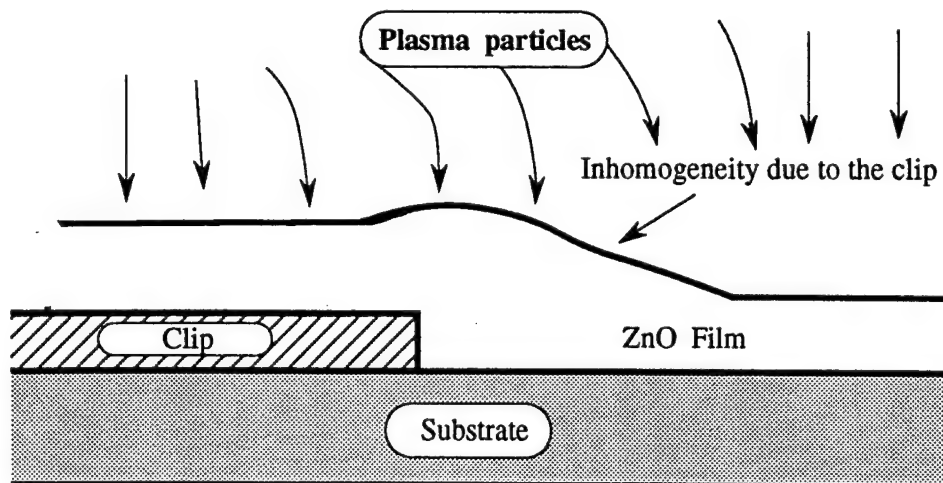
Figure 10: Temperature increase due to the plasma versus RF power

The plasma increases the substrate temperature from 23 °C for 100 W, to 41 °C for 300 W, and 56 °C for 500 W. Figure 10 shows the increase in substrate temperature due to the plasma energy as a function of the applied RF power.

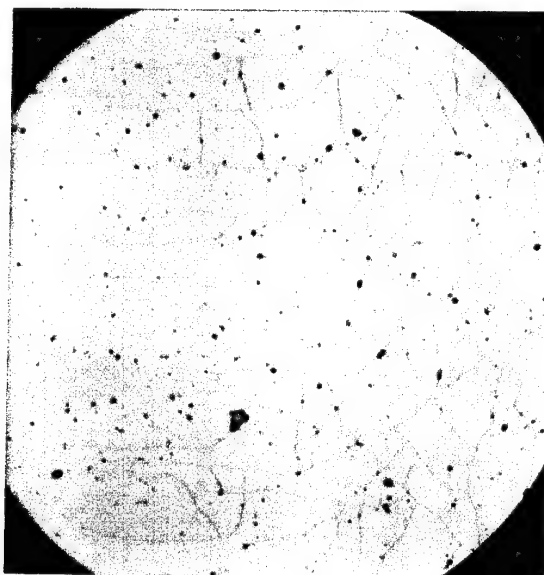
An important result that comes from these measurement is that about 50 mn are needed for the substrate temperature to stabilise after the RF power has been applied. This stabilization time remains roughly the same for switching the RF power from 0 to 300 W, as for 100 to 300 W. This very long stabilization time leads to the varying film structure during the first hour of deposition. We think that the film density (i.e. the deposition rate) variation we have observed is due to that temperature variation at the beginning of the process. A way to overcome that problem could be to use a very small shutter, very close to the substrate, so that the plasma would heat the plate and also the substrate without any film to be deposited on it.

### II-5 Problems we met during sputtering.

We have noticed that an important proportion of the ZnO films we deposited were cracked. Figure 11-a shows such a film. We tried to overcome the problem by changing the deposition parameters (principally the ratio argon/oxygen), and after a considerable number of runs, it appeared that the problem of cracks was due to the cooling process we used to cool down our substrate after deposition. We thought that it was useful to let the samples cool down during few hours in the vacuum, before venting the machine. In fact, the uncracked films correspond to the runs where the chamber was ventilated as soon as the sputtering was finished. We have not yet well understood why films do not crack when they are cooled down suddenly, but we think it is because of the inhomogeneity of the film thickness at the vicinity of the clips we use to attach the sample to the substrate holder. The figure below is an illustration of that kind of shadow effect due to the direct substrate environment.



a)



b)

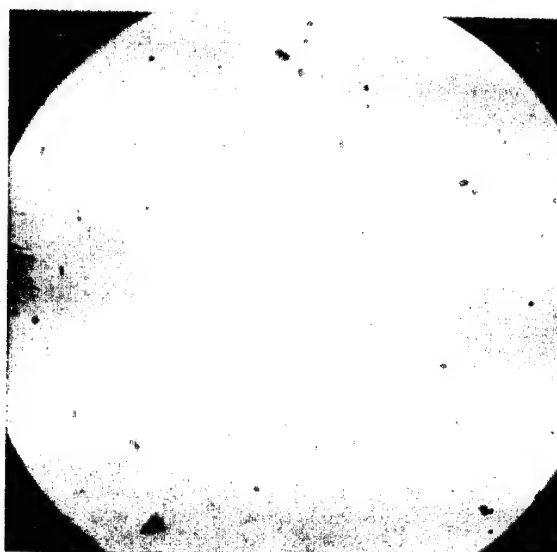


Figure 11: Effect of cooling process

- a) Cracks observed when slowly cooling the substrate
- b) Film uncracked after quickly venting the chamber

We think that since the film thickness is not homogeneous, stresses appear in the film while cooling down. We have observed that cracks were perpendicular to the clips in the vicinity of them. When the film cools down slowly, internal stresses have time to change the film structure inhomogeneously, causing cracks. Conversely, if the film cools down quickly, the structure has no time to change, and the film is suddenly fixed in its first structure and does not crack (the same process as used for the fabrication of temper steel !). Figure 11-b shows the surface of such an uncracked film.

Another problem we met while sputtering of ZnO films concerns the measurement of the film thickness. We have noticed that the film thickness monitor attached to the sputtering equipment is not accurate enough to allow accurate thickness control. We have developed an *in situ* laser measurement of the thickness and optical losses of the film (optical losses give real time information on the film structure). The following section deals with this laser measurement system.

### III IN SITU MEASUREMENT OF FILM THICKNESS AND OPTICAL LOSSES.

We have developed a simple and accurate interferometric method for simultaneous, *in situ* measurement of both the thickness and the depth resolved optical losses of thin transparent films. The experimental arrangement is simple, requiring only a laser and a detector regardless of the substrate. The originality of the method is based on the evaluation of the optical losses from the envelopes of the laser signal, while the thickness is measured conventionally by counting the number of signal periods. Using this method, the evolution of optical losses is easily observed during deposition, leading to the possibility of a real time control of the film quality.

The film is assumed to be transparent at the interrogating wavelength,  $\lambda$ , so that a Fabry-Pérot interference signal can be obtained, leading to an *in situ* measurement of both the optical thickness of the film and the deposition rate. The physical film thickness can then be determined from a knowledge of the refractive index. Conversely, an independent measurement of thickness allows the calculation of the actual index.

The following section deals with theoretical considerations that illustrate how the thickness and the optical losses of the film can be determined. The further section concerns experimental results. In particular we describe the method used to evaluate the depth resolved optical losses in real time.

#### III-1 Theoretical considerations.

We now consider a homogeneous, isotropic, and transparent film deposited on a reflecting substrate. We assume that the optical losses due to the surface roughness remain constant during deposition.

Let  $d$  and  $n$  be the thickness and the refractive index of the film respectively. An S polarized laser beam of wavelength  $\lambda$  is incident on the film at an angle  $\theta_0$  as shown in figure 12-a (a P polarised beam is less sensitive to thickness change). In this case, the normalized power reflectivity is:

$$S = \frac{I}{I_0} = \frac{R + e^{-2\alpha p} - 2r e^{-\alpha p} \cos(\varphi)}{1 + R e^{-2\alpha p} - 2r e^{-\alpha p} \cos(\varphi)} \quad (5)$$

with  $R$  and  $r$  respectively the power and amplitude Fresnel coefficients at the vacuum  $\rightarrow$  film interface,  $\alpha$  the average losses per unit length,  $p=2d/\cos\theta_1$  the ray path through the film for a double traversal, and  $\varphi = (4\pi d/\lambda)(n^2 - \sin^2\theta_0)^{1/2}$  the phase difference between two consecutive elementary reflected rays. Figure 12-b shows the theoretical reflected signal obtained with the following parameters corresponding to orientated polycrystalline ZnO;  $n=1.923$ , deposition rate  $\approx 11.17$  nm/mn,  $\theta_0=74^\circ$ ,  $\alpha=47$  mm $^{-1}$ . The value of the refractive index we use here is lower than the bulk value, because sputtered films are generally less dense than the monocrystalline material. The increase in film thickness corresponding to one period of the reflected signal is:

$$\Delta d = \frac{\lambda}{2\sqrt{n^2 - \sin^2\theta_0}} \quad (6)$$

Therefore, the film thickness is given by the total number of signal periods. In order to calculate the optical losses, we have to consider the envelopes of the signal. Signal *maxima* occur when  $\cos\varphi = 1$ , then the film thickness is equal to  $d_k = k\lambda/2(n^2 - \sin^2\theta_0)^{1/2}$ , where  $k$  is an integer. *Minima* occur when  $\cos\varphi = -1$ , i.e.  $d_k = (2k+1)\lambda/4(n^2 - \sin^2\theta_0)^{1/2}$ . Let  $S_M$  and  $S_m$  be the envelopes of the *maxima* and *minima* respectively. The envelopes are given by:

$$S_M = \frac{R + e^{-2\alpha p} - 2r e^{-\alpha p}}{1 + R e^{-2\alpha p} - 2r e^{-\alpha p}} \quad (7)$$

$$S_m = \frac{R + e^{-2\alpha p} + 2r e^{-\alpha p}}{1 + R e^{-2\alpha p} + 2r e^{-\alpha p}}$$

Because  $r$  is negative,  $S_m$  can be equal to zero (visibility equal to 1) as shown on figure 12-c. Therefore, the average losses per unit length can be estimated by measuring the thickness  $d_0$  for which the visibility is equal to 1. From equation (7) the losses are:

$$\alpha = \frac{-\ln\sqrt{R} \cdot \cos(\theta_1)}{2d_0} \quad (8)$$

We consider next a film deposited on a transparent semi-infinite substrate whose refractive index is  $n_0$  as shown in figure 13-a. In this case, the normalized reflected intensity is:

$$S = \frac{I}{I_0} = \frac{R_1 + R_2 e^{-2\alpha p} + 2r_1 r_2 e^{-\alpha p} \cos(\varphi)}{1 + R_1 R_2 e^{-2\alpha p} + 2r_1 r_2 e^{-\alpha p} \cos(\varphi)} \quad (9)$$

where the subscripts 1 and 2 refer to the vacuum  $\rightarrow$  film and the film  $\rightarrow$  substrate interfaces respectively. Figure 13-b shows the theoretical signal obtained with the same parameters as those used for figure 12-b, with  $n_0=1.46$  (fused quartz). The increase in film thickness corresponding to one period of the signal remains the same as that of a reflecting substrate, but *maxima* now occur when  $\cos\varphi = -1$  and *minima* when  $\cos\varphi = 1$ . Hence the *maxima* and *minima* envelopes are described by:

$$S_M = \frac{R_1 + R_2 e^{-2\alpha p} - 2r_1 r_2 e^{-\alpha p}}{1 + R_1 R_2 e^{-2\alpha p} - 2r_1 r_2 e^{-\alpha p}} \quad (10)$$

$$S_m = \frac{R_1 + R_2 e^{-2\alpha p} + 2r_1 r_2 e^{-\alpha p}}{1 + R_1 R_2 e^{-2\alpha p} + 2r_1 r_2 e^{-\alpha p}}$$

It can be shown that the signal for a transparent substrate can not exhibit a visibility of 1 in the presence of loss. Therefore, the average losses of a transparent substrate are more difficult to evaluate than those of a reflecting substrate (see below). Figure 13-b also shows that the signal amplitude is lower for a transparent substrate than for a reflecting one. This is because a large part of the incident energy crosses the film, and then propagates into the substrate which is considered to be semi infinite (it is possible to calculate the reflectivity of a system involving a non infinite, or multilayer, substrate using Abeles formalism [8], but it is not the purpose of this study).

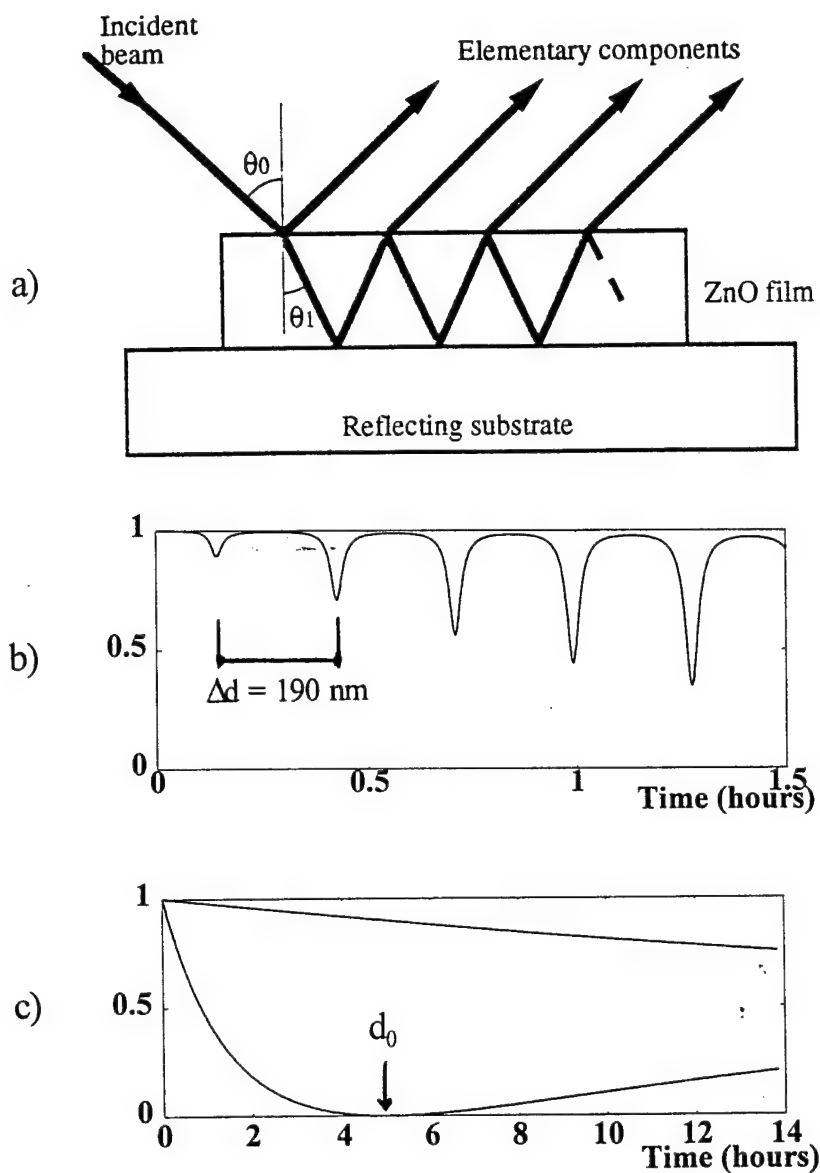


Figure 12: Theoretical results for a reflecting substrate.

- a) Schematic diagram of multiple reflections from a transparent film on a reflecting substrate.
- b) Theoretical laser signal versus time. The parameters used are:  $n=1.923$  (polycrystalline ZnO); rate=11.17 nm/mm;  $\theta_0=74^\circ$ ;  $\alpha=47 \text{ mm}^{-1}$ .
- c) Envelopes of the *maxima* and *minima*.  $d_0$  is the thickness for which the visibility is equal to 1.

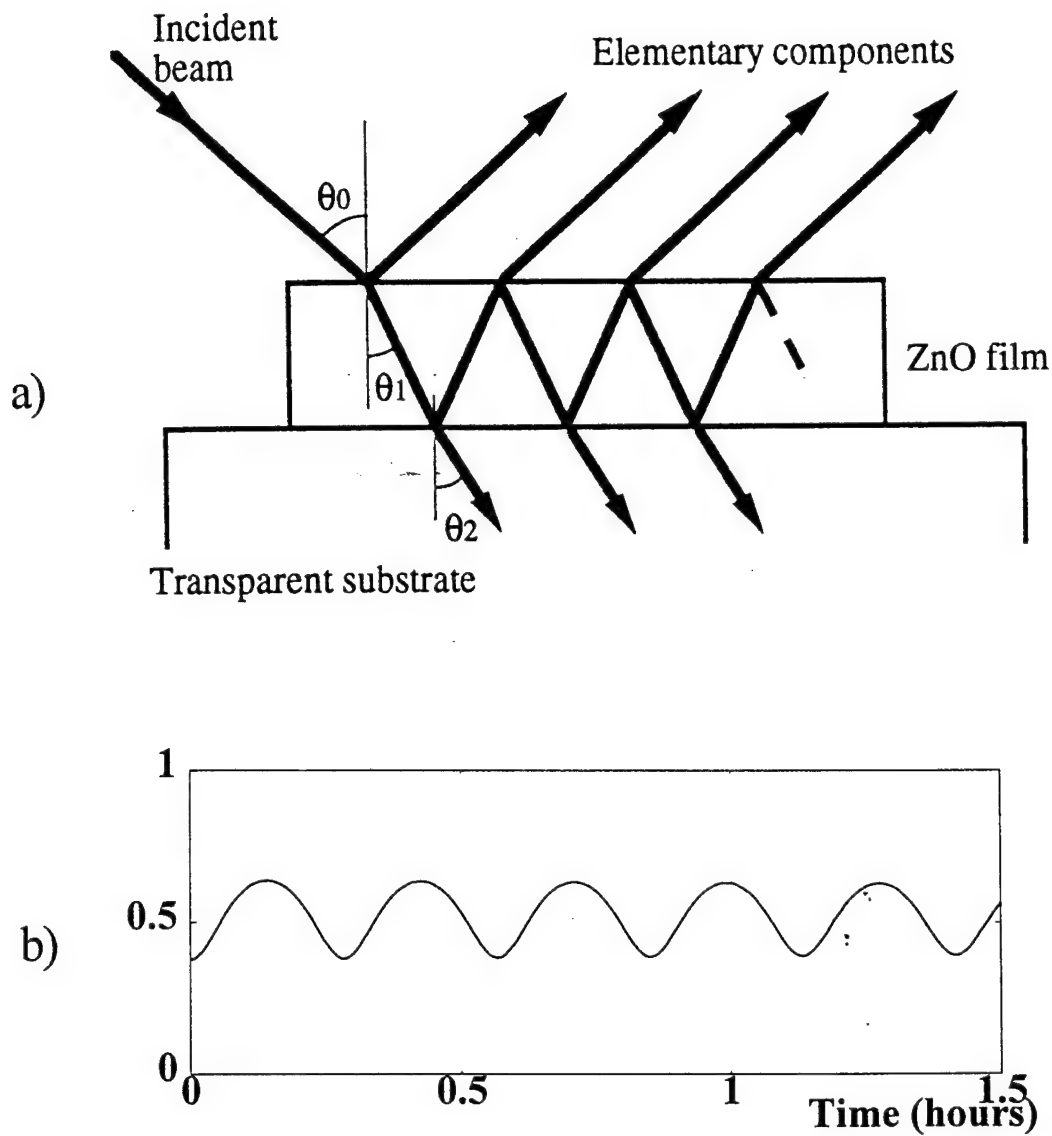


Figure 13: Theoretical results for a transparent substrate.

- a) Schematic diagram of multiple reflections from a transparent film on a transparent substrate.
- b) Theoretical laser signal versus time. The parameters used are the same than for figure 12-b, the refractive index of the substrate is  $n_0=1.46$  (fused quartz).



### III-2 Experimental results.

This optical thin film evaluation method has been used whilst sputtering zinc oxide on a variety of substrates. We have developed this technique to precisely control the thickness and to monitor the film structure during deposition. Figure 14 shows a signal recorded during the deposition of a 9270 nm thick film on a gold coated silicon wafer. For oriented polycrystalline ZnO, equation (6) implies that  $\Delta d = 190$  nm. Therefore the recorded 48.8 periods correspond to a 9270 nm thick zinc oxide film. The thickness for which the visibility is equal to 1 is  $d_0 = 3325.5$  nm, and equation (8) leads to optical losses of  $\alpha = 47$  mm<sup>-1</sup>. This experimental signal is in good agreement with the theoretical signal of figure 12. However, we acknowledge that the film structure varies during deposition, consequently the optical losses may not be considered constant. By using the envelopes of the recorded signal, we can deduce the depth-resolved optical losses as a function of film thickness. For the envelope of *maxima*, equation (7) can be written as:

$$X^2 (S_M R - 1) + X 2r(1 - S_M) + (S_M - R) = 0 \quad (11)$$

where  $X = e^{-\alpha d}$ . For each period of the recorded signal, we measure  $S_M$  and the corresponding film thickness, and the optical losses are deduced from the positive solution  $X$ . Alternatively, the same calculation can be made by considering the envelope of *minima*. Figure 15 shows the average of the real time losses calculated from the measured *maxima* and *minima* envelopes. It can be seen, that the film quality decreases for thicknesses between 1580 and 3290 nm, and then increases from 3290 to 4170 nm. The quality of the film then remains constant between 4170 and 8000 nm. Losses are very high at the beginning of the film deposition, probably because the light is greatly scattered by the initially poorly structured film. The losses of a similar film measured by spectrophotometry are consistent with those obtained using our *in situ* method as shown in the insert of figure 15. Figure 16 shows a comparison between the signals obtained with a reflecting (gold coated silicon wafer) and a transparent substrate (fused quartz), and both compare favourably with the theoretical curves of figures 12-b and 13-b.

### III-3 Conclusion.

Theoretical and experimental studies of an interferometric method for the evaluation of both thin film thickness and depth-resolved optical losses have been presented. Due to a large angle of incidence (of the order of 74° with respect to the normal), the thickness variation corresponding to a period of the signal is small, leading to a very accurate film thickness measurement. The method can be used with a large variety of substrates, and can also be applied to different deposition techniques. One possible and important application is the on-line control of deposition parameters to facilitate production of low-loss optical films and high quality acoustic transducers.

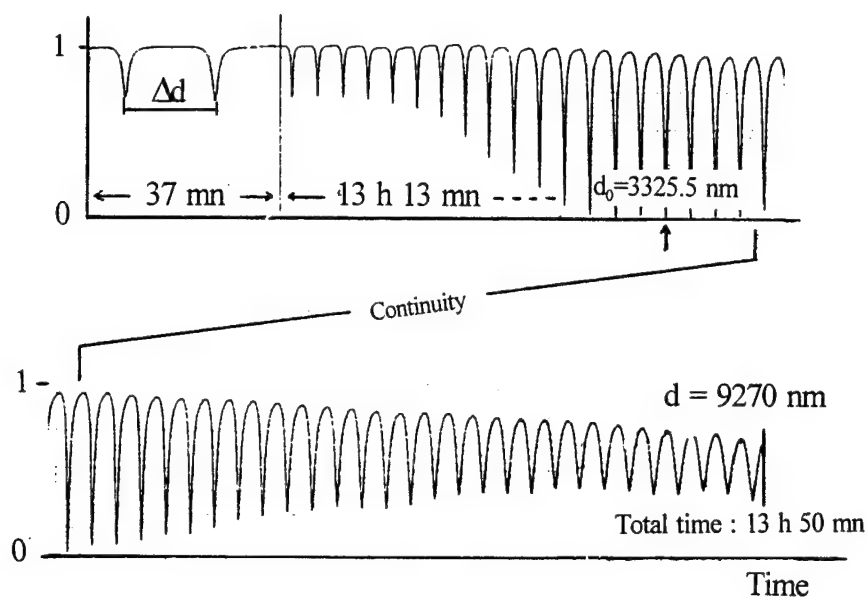


Figure 14: Experimental signal recorded while sputtering a 9270 nm thick ZnO film (48.8 periods) on a reflecting substrate. The thickness for which the visibility is equal to 1 is  $d_0=3325.5$  nm, leading to the optical losses  $\alpha=47$  mm<sup>-1</sup>.

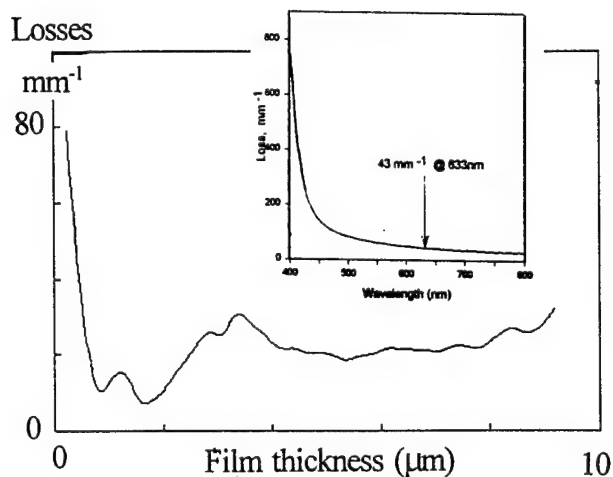


Figure 15: Real time losses versus film thickness recorded during the deposition of the film. This curve is obtained by averaging the results for envelopes of both *maxima* and *minima*. The insert shows the absorption spectrum obtained with a more lossy film. The orders of magnitude are comparable.

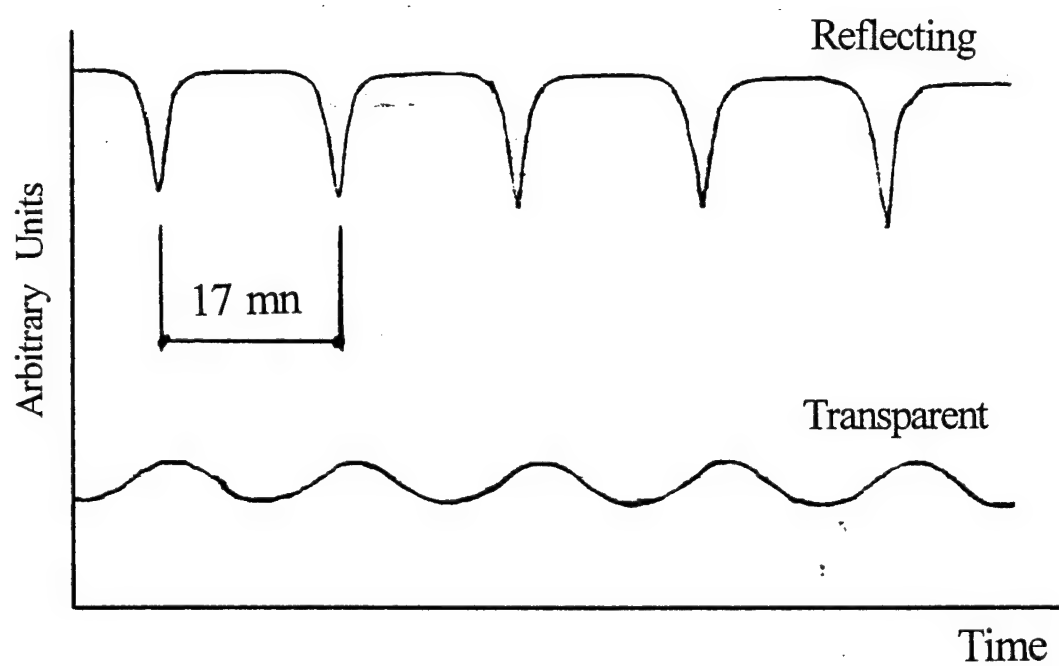


Figure 16: Comparison between experimental signals obtained with a reflecting substrate (upper curve) and a transparent one (lower curve). The signals are not drawn to the same scale.

An important result is that the optical losses are very high at the beginning of the film deposition. We think that it is due to the varying temperature at the beginning of the deposition that we have already reported. In the next section, we will discuss the problem of the initial evolution of the film structure, and in particular, we will show the influence of the plasma heating at the beginning of the deposition on the effective piezoelectricity of ZnO sputtered films.

#### IV EFFECTIVE PIEZOELECTRIC ACTIVITY OF ZINC OXIDE FILMS GROWN BY RF PLANAR MAGNETRON SPUTTERING.

We have already mentioned that to obtain films of high piezoelectric activity, it is important that their c axis (height of the three-dimensional lattice) is normal to the substrate surface. RF planar magnetron sputtering of ZnO is an efficient process for the deposition of highly oriented zinc oxide films. However, film reproducibility remains a problem despite considerable research in this field. The problem of reproducibility is mainly due to the large number of interdependent sputtering parameters; the input RF power, the sputtering gas pressures and the substrate temperature can all be tuned to vary the film's structure. When growing thin piezoelectric films, the film thickness is an important parameter as it determines the resonant frequency of the transducer. However, it is often observed that the real resonant frequency of RF sputtered piezoelectric ZnO films is higher than that predicted from knowing of the physical thickness of the film.

It is of crucial importance to understand the discrepancy between the real and the expected resonant frequency because the design of acoustooptic modulators requires accurate control over the resonant frequency. In this section, we show that the discrepancy between the measured and the expected resonant frequency is due to a poorly structured, non-piezoelectric layer which is formed at the beginning of the film growth. This initial layer results in the film thickness exhibiting piezoelectric activity being smaller than the total film thickness, and thus leads to a higher resonant frequency.

##### IV-1 Summarise of what we already know.

###### \* Problem of substrate temperature.

The structure of RF sputtered ZnO thin films depends strongly on the deposition parameters. In particular, the heat provided by the substrate temperature gives the deposited atoms extra surface mobility, allowing them to reach the lowest thermodynamically favoured lattice positions. Hence

the substrate temperature has a significant effect on the film structure. The substrate temperature is usually monitored by a thermocouple situated outside the vacuum chamber, close to the substrate holder. Since the thermocouple is not in direct contact with the substrate on which the film is deposited, the measured temperature does not correspond to the *real* substrate temperature. We monitored the *real* substrate temperature using a second RF filtered thermocouple located inside the vacuum chamber, in contact with the substrate. Time dependent temperature measurements were carried out with increasing input RF power. Figure 9 shows the evolution of the substrate temperature with time for different values of input RF power. During this measurement, the initial substrate temperature was 100 °C and the argon and oxygen pressures were 8 mTor and 1.5 mTor respectively. It can be seen that the glow discharge, initiated in the chamber to grow the ZnO film, increases the substrate temperature. An input RF power of 100 W increases the substrate temperature by about 23 °C, while the increase in temperature is 41 °C for 300 W and 56 °C for 500 W. An important observation is that it takes approximately 50 mn for the substrate temperature to stabilise. As a consequence, the film structure must vary during this initial period.

#### \* Problem of deposition rate.

The deposition parameters, *i.e.* the argon and oxygen pressures and the input RF power, are held constant during the film deposition. Consequently, the deposition rate is expected to remain constant throughout the process, provided that the film density also remains constant. On measuring the deposition rate during the beginning of the film growth, we find that this is not so. In section II-4-1, we have presented the evolution of the deposition rate over an initial period of 100 mn under the following conditions; argon and oxygen pressures 8 mTor and 1.5 mTor respectively, substrate temperature 100 °C and RF power 500 W. It can be seen that the deposition rate increases during the first 50 mn of the process, before stabilising to a constant value. Assuming that the quantity of incoming zinc and oxygen atoms remains constant, this variation in the deposition rate can be attributed to a variation in the film density. Equation (4) relates the density variation to the variation in the deposition rate. It shows that an increase in the deposition rate corresponds to a decrease in the film density. From the figure presented in section II-4-1, we can thus say that the density is initially high but decreases continuously as the temperature stabilises during these first 50 mn. At first, we attributed the higher density to the deposition of an amorphous layer at the beginning of the process, but we will illustrate that it is more a randomly oriented polycrystalline phase, than an amorphous layer.

#### \* Problem of optical losses.

In section III, we have presented an *in situ* interferometric method for measurement of both film thickness and depth resolved optical losses during the deposition. Figure 15 shows the evolution of the optical losses of a ZnO film as a function of the film thickness. This real time optical losses measurement was recorded while growing a 9270 nm thick ZnO film with a deposition rate of about 11.2 nm/mn. It appears that the optical losses are very high during the deposition

of the first 600 nm of the ZnO film. According to a deposition rate of 11.2 nm/mn, the time required for the optical losses to reach a lower and more stable value is about 54 mn (*i.e.* when the film thickness is greater than 600 nm). After that period, the film quality stabilises, and the optical losses are effectively constant. Since the initial optical losses are high, the first layer is not amorphous, as it is well known that amorphous materials usually exhibit low optical losses. Hence, we conclude that the first layers of a sputtered ZnO film consist of small, randomly oriented crystallites. Figure 17 shows an SEM picture of a 9  $\mu\text{m}$  thick film deposited on an optical fibre. The varying structure is clearly visible.

#### IV-2 Consequence for the real resonant frequency.

This depth resolved variation in the structure of sputtered ZnO films is an important problem as it implies that only a part of the films grown by RF planar magnetron sputtering contributes to piezoelectric activity. Therefore, we can define two different thicknesses: the physical thickness  $d_0$  and the piezoelectric thickness  $d_1$  which effectively induces piezoelectric activity. Let  $f_0$  be the expected, and  $f_1$  be the measured resonant frequency. The thickness of the randomly oriented layer can then be expressed as:

$$\Delta = d_0 - d_1 = \frac{v}{2} (1/f_0 - 1/f_1) \quad (12)$$

where  $v$  is the sound velocity in the transducer material ( $v = 5300$  m/s for sputtered ZnO). Figure 18 shows the  $S_{11}$  reflection coefficient obtained by testing a 9205 nm thick ZnO film with a HP 8753B network analyzer. This film was sputtered on a gold coated fused quartz disk with a deposition rate of 29 nm/mn. The device was electrically matched to achieve 39 dB coupling efficiency as shown in figure 18. The closely spaced dips are caused by acoustic resonances in the 1 mm thick fused quartz disk (the average frequency spacing between two consecutive dips is equal to the free spectral range (FSR) of the disk,  $\text{FSR} = 2.9$  MHz).

The expected resonant frequency was  $f_0 = 288$  MHz, while the measured resonant frequency was  $f_1 = 332.5$  MHz. Therefore, (from equation (12)) the thickness of the non-piezoelectric layer is  $\Delta = 1231$  nm. The deposition rate, used to grow the film in question, was equal to 29 nm/mn, implying that the initial randomly oriented 1231 nm was grown in the first 43 minutes. This period is shorter than the 50 mn required to stabilize the substrate temperature, but the discrepancy arises because the film structure evolves continuously from a poorly piezoelectric state to a highly oriented state, which is not accounted for by equation (2).

We have also observed an effective resonant frequency different than the expected one when growing a 10.6  $\mu\text{m}$  thick ZnO film on a gold coated  $\text{TeO}_2$  crystal. The expected resonant frequency was supposed to be 250 MHz. Figure 19 shows the  $S_{11}$  reflection coefficient obtained by testing this film with the network analyzer. The 32 dB coupling efficiency that can be observed shows that the real resonant frequency is 295 MHz. Therefore, the thickness of the randomly oriented layer is  $\Delta = 1.62$   $\mu\text{m}$ .



Figure 17: Scanning Electron Microscope image of thick ZnO film (x 8000 magnification). The varying film structure is clearly visible.

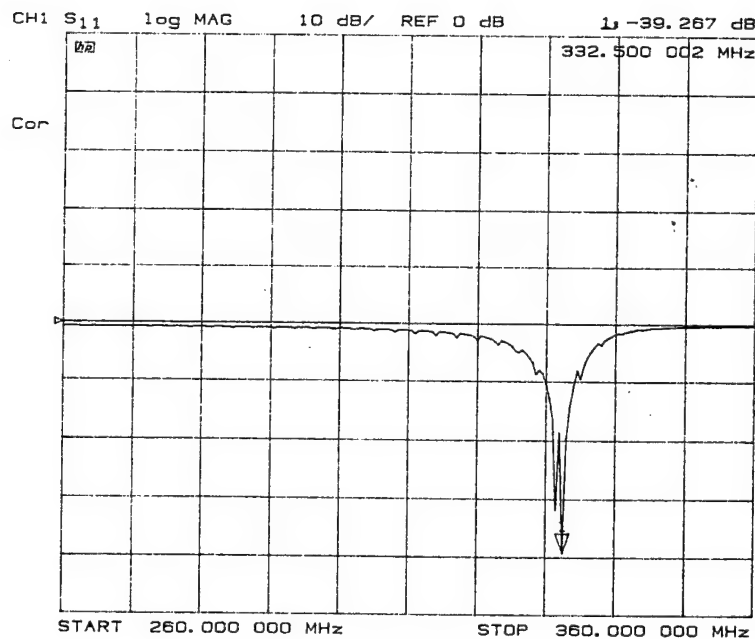


Figure 18:  $S_{11}$  reflection coefficient obtained by testing a 9205 nm thick ZnO film with a HP 8753 B network analyzer. The - 39 dB dip locates the resonant frequency, which occurs at 332.5 MHz instead of 288 MHz as expected. The closely spaced dips define the FSR of the fused quartz disk to be 2.9 MHz.

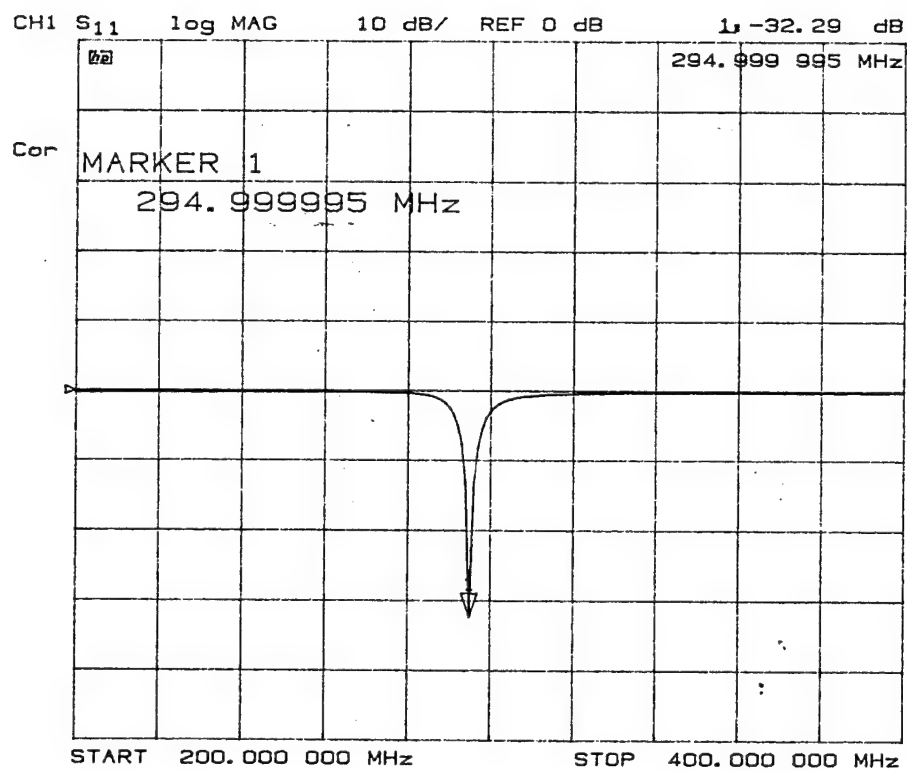


Figure 19: S<sub>11</sub> reflection coefficient obtained by testing a 10.6  $\mu\text{m}$  thick  $\text{D}$  film with a HP network analyzer. The - 32 dB dip locates the resonant frequency, which occurs at 295 MHz instead of 250 MHz as expected.



### IV-3 Conclusion.

In conclusion, we have shown that the increase in substrate temperature due to the plasma energy in sputtering systems, leads to a continuous variation in the structure of ZnO films. At the beginning of deposition, the film is randomly oriented and poorly piezoelectric, but evolves to a highly oriented and piezoelectric state when the substrate temperature has stabilised. Therefore, the effective piezoelectric thickness of the film is less than its physical thickness, leading to a higher resonant frequency. Real time measurements of the substrate temperature, the deposition rate, and the optical losses of ZnO films during deposition all indicate that the film structure evolves over the first 50 mn. SEM images of the initial layer corroborated our prediction, and network analyzer measurements of the resonant frequency provided further confirmation. The initial evolution of the structure of sputtered thin films, caused by plasma heating, is an inherent problem of RF sputtering deposition. The responsivity of the temperature controller to temperature increases at the substrate is slowed by the large thermal inertia of commonly used substrate backing plates. Consequently, the temperature controller is unable to compensate for plasma heating. It is therefore important to consider our above observations to improve ZnO film reproducibility, and in particular to control the real resonant frequency which is the key factor in the design of acoustooptic devices.

## V FABRICATION OF ANNULAR ZnO TRANSDUCERS ON OPTICAL FIBRES.

### V-1 Introduction.

An advantage that piezoelectric Zinc Oxide transducers have over their Lithium Niobate equivalents is that ZnO transducers can easily be configured on curved surfaces. The ultimate test for this property is to deposit ZnO on the highly curved surface of an optical fibre. This configuration also yields a very interesting device; under RF excitation the annularly deposited ZnO film acts to phase modulate light in the fibre core [9].

ZnO fibre transducers have previously been reported [10] but phase modulation is only reported in a fibre with a transducer over 180° of the fibre surface [11]. An efficiency of 1.48rad/√Watt was achieved in this configuration. But as this device operates in the travelling wave regime it will not be as efficient as the annular transducer.

### V-2 Deposition of ZnO on highly curved surfaces.

Deposition of a uniform ZnO film on a fibre required a rotating fibre chuck to be installed in the sputtering chamber. The fibre chuck is shown in figure 20 and consists of a chuck which is rotated by a shaft driven by a motor located outside the chamber.

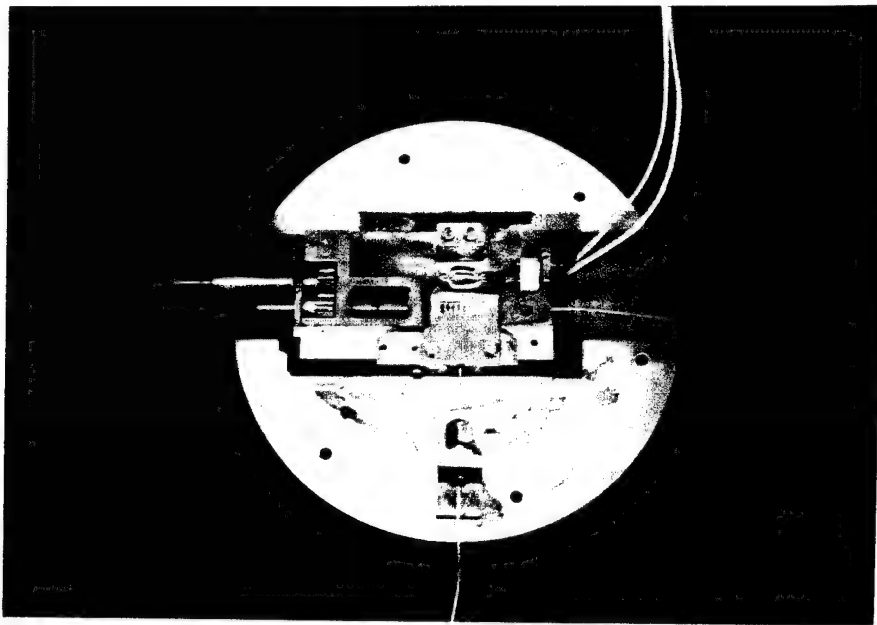


Figure 20: Fibre chuck used to deposit ZnO on an optical fibre.

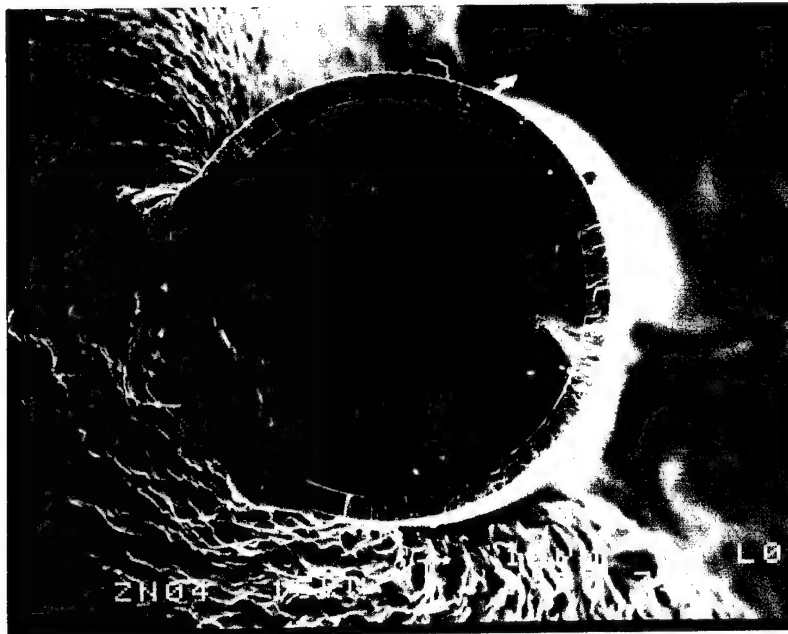


Figure 21: Crosssection of a ZnO coated optical fibre

The fibre is heated incandescently by a halogen lamp to a temperature of 175°C during ZnO deposition. An RF filtered thermocouple, located close to the fibre provides feedback to a temperature control unit which regulates the temperature by altering the current delivered to the bulb. This system allows for accurate and very responsive control of the fibre temperature during thin film deposition. The fibre chuck also facilitates masking of the fibre to allow the definition of a variety of transducer configurations. The fibre that we use is either a standard silica fibre with the coating stripped in the transducer region, or a fibre which has previously been electroplated with a 5µm coating of gold. Both fibres are single moded at 1550nm.

The fabrication of a ZnO transducer requires the following processing steps. The fibre is stripped of its coating and mounted in the fibre chuck in the sputtering chamber which is then evacuated down to less than  $10^{-6}$  mTorr. The fibre is rotated at 3 rpm whilst a 30nm chrome layer is deposited (this improves the adhesion of the gold to the silica fibre) and subsequently a 1 to 2 µm gold layer is grown. The very thick gold layer strengthens the fibre, protecting it from fracture caused by the contraction of the cooling ZnO layer after deposition. The masks on the fibre chuck are then changed and the chamber is pumped down ready for the sputtering of the ZnO. For this step the rotation of the fibre is reduced to 3 rph as sputtering rates are much slower than evaporation. The sputtering gases are introduced to the chamber (10mTor Argon and 1mTor of Oxygen) and the fibre is heated to 175°C. Once the temperature has stabilised the plasma is struck with a power of 450 Watts. For the initial 40 minutes a shutter shields the fibre from the plasma. This presputtering period removes contaminants from the target surface and allows the deposition rate to stabilise. After the shutter has been opened then the deposition continues until the desired film thickness has been achieved. Note that due to the rotation of the fibre the deposition times are increased by a factor of  $\pi$  and an 18 hour run is required to achieve an 8µm film with a resonant frequency of 350 MHz.

The crosssection of a fibre coated with ZnO is shown in figure 21, where the columnar structure of the ZnO film is visible. The final step is to change the masks to define the top gold electrode which is evaporated to a thickness of 500nm. Figure 22 shows a 1mm wide gold electrode on a Zinc Oxide coated fibre.

The fibre is glued into a perspex groove and gold contact wires are bonded to the top and bottom electrodes. Adhesion of the wires and damage to the electrodes can be a problem particularly if the electrodes are less than 500nm thick. However if a low bonding power and little tension on the wire are used these problems can be overcome. Once the bond wires are in place the transducer is electrically matched at its resonant frequency.

### V-3 Conclusion.

In this section, we have demonstrated the possibility of depositing piezoelectric ZnO films on highly curved surfaces. The ultimate case of deposition on an optical fibre has been investigated. The main result concerns the thickness of the gold electrodes that has to be thick enough to protect the fibre fracture due to the contraction of the cooling ZnO film. The interest of this experimentation is to show that ZnO films can be deposited on a wide variety of surface curvatures, allowing the use of such transducers in the curved devices we have presented in the previous part.

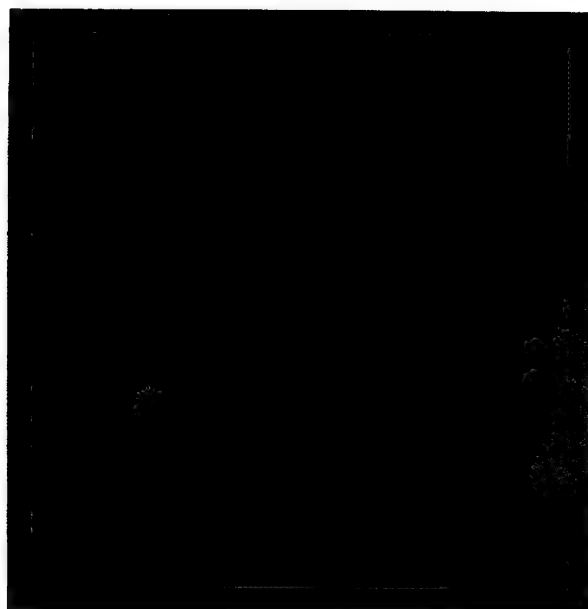


Figure 22: Microscope picture of a 1 mm wide gold electrode on a ZnO coated optical fibre.

## VI CONCLUSION.

We have presented theoretical and experimental studies concerning the deposition of piezoelectric ZnO thin films. RF planar magnetron sputtering was used to grow ZnO piezoelectric films, and the influence of the sputtering parameters were investigated in order to increase our knowledge of this specific deposition technique.

A large number of deposition runs have been carried out. Section II presents the influence of the sputtering parameters on the films structure. The main result concerns the substrate temperature that increases during the first 50 mn of deposition due to the energetic plasma particles that heat the substrate. As a result, the films structure varies during the deposition of this initial layer. When the substrate temperature has stabilised, the film structure remain constant until the end of the ZnO deposition.

We developed an *in situ* interferometric technique used to evaluate the film thickness and the depth resolved optical losses during the film deposition. This thin films evaluation technique is described in section III. Interferometric thickness measurement techniques are used for many years. The originality of the method consists of considering the envelopes of the interference signal to determined the depth resolved optical losses of the film during the deposition. Since these optical losses are directly related to the film quality, this *in situ* evaluation technique is of great interest when growing several microns thick films. The main result obtained using this technique is that the optical losses are very high at the beginning of the deposition process, which corroborate what we have observed when measuring the substrate temperature.

We stated that these high optical losses at the beginning of the film growth are due to the formation of a poorly structured initial layer when the substrate temperature increases. Consequently, the *effective* piezoelectric thickness of the ZnO transducer is less than its *physical* thickness, leading to a higher resonant frequency. The effective piezoelectric activity of sputtered ZnO films has been presented in section IV. SEM images, as well, as network analyzer measurements of the resonant frequency provided further confirmations.

Section V dealt with the deposition of oriented ZnO on highly curved surfaces. The ultimate test was to deposit ZnO on optical fibres. By using a rotating fibre chuck, we succeeded in depositing highly oriented ZnO on such curved surfaces. The main conclusion concerns the need of thick gold electrodes to protect the fibre fracture due to the contraction of the cooling ZnO film.

## REFERENCES

### PART II

- [1] S.K. Tiku, C.K. Lau, K.M. Lakin, "Chemical vapor deposition of ZnO epitaxial films on sapphire" *Applied Physics Letters*, Vol. 36, N° 4, 1980
- [2] J. Aranovich, A. Ortiz, R.H. Buhe, "Optical and electrical properties of ZnO films prepared by spray pyrolysis for solar cell application", *Journal of Vacuum Science Technology*, Vol. 16, N° 4, 1979
- [3] A. N. Chernets, N. L. Kringsberg, "Preparation and properties of thin films of ZnO for hypersonic transducers", *Thin Solid Films*, Vol. 18, 1973
- [4] G. Perluzzo, C. K. Jen, E.L. Adler, "Characteristics of reactive magnetron sputtered ZnO films", *Ultrasonic Symposium*, 1989
- [5] M. Wybierala, C. W. Pitt, "Examination of the relationship between the acoustic transduction properties of thin film zinc oxide and its pyroelectric coefficient", 3<sup>d</sup> Year Progress Report for "SUPELEC" project, UCL, 1981
- [6] S.M. Rossnagel "Dynamic interactions in the physical properties of magnetron deposition systems", *Material Science and Engineering*, A 140, 1991
- [7] C.W. Pitt, F.R. Gfeller, R.J. Stevens, "RF sputtered thin films for integrated optical components", *Thin Solid Films*, Vol. 26, 1975
- [8] M. Born, and E. Wolf, *Principles of Optics*, 6<sup>o</sup> Ed., Pergamon Press New-York
- [9] H.F. Taylor, "Acoustooptic Modulators for Single-Mode Fibres", *J. Lightwave Tech.*, Vol. LT-5, 1987, pp 990-992.
- [10] F.S. Hickernell, "The Characteristics of Coaxial ZnO Thin-Film BAW Transducers on Optical Fibers", *Proc. IEEE Ultrason. Symp.*, 1988, pp417-420.
- [11] A.A. Godil, D.B. Patterson, B.L. Heffner, G.S. Kino, B.T. Khuri-Yakub, "All-Fiber Acoustooptic Phase Modulators Using Zinc Oxide Films on Glass Fibre", *J. Lightwave Tech.*, Vol. 6, 1988, pp 1586-1590.

## PART III

### EXPERIMENTAL RESULTS CONCERNING THE PIEZOELECTRIC ACTIVITY OF ZnO FILMS

In this part, we present the different techniques that have been investigated to determine the piezoelectric activity of our ZnO thin films, and to evaluate the scale of the acoustooptic interaction achieved in each of the devices that we fabricated. Experimental studies were carried out in various directions.

Firstly, we constructed a pulse-echo rig which was used to estimate the piezoelectric behaviour of the thin ZnO films we proposed to use in the acoustooptic modulators. This pulse-echo technique measures the efficiency of the transducer as a converter of electrical to mechanical energy. It involves sending bursts of an RF signal into a transducer and picking up the reflected acoustic pulses. Basically, the ratio of input to output pulses is related to the transduction losses, which give information about device quality and film orientation.

Secondly, because the conversion of electrical to mechanical energy is the key point of piezoelectric transducers, electrical impedance matching had to be fully understood. We studied the problem of electric matching by estimating the RF electrical properties of our transducers, and constructing high frequency electronic matching circuits, with the aid of an HP network analyzer.

Thirdly, we built planar acoustooptic modulators using  $\text{TeO}_2$  crystals as the interaction medium. We have already mentioned that this material is of great interest for acoustooptic interaction due to its high  $M_2$  figure of merit. The purpose of these experimental studies was to increase our knowledge of acoustooptic interaction involving ZnO thin film transducers operating at frequencies of few hundreds of MHz. It is of crucial importance to fully understand the acoustooptic interaction mechanism in the simple case of an isotropic interaction medium, before investigating the more complicated case of gradient index acoustooptic modulators.

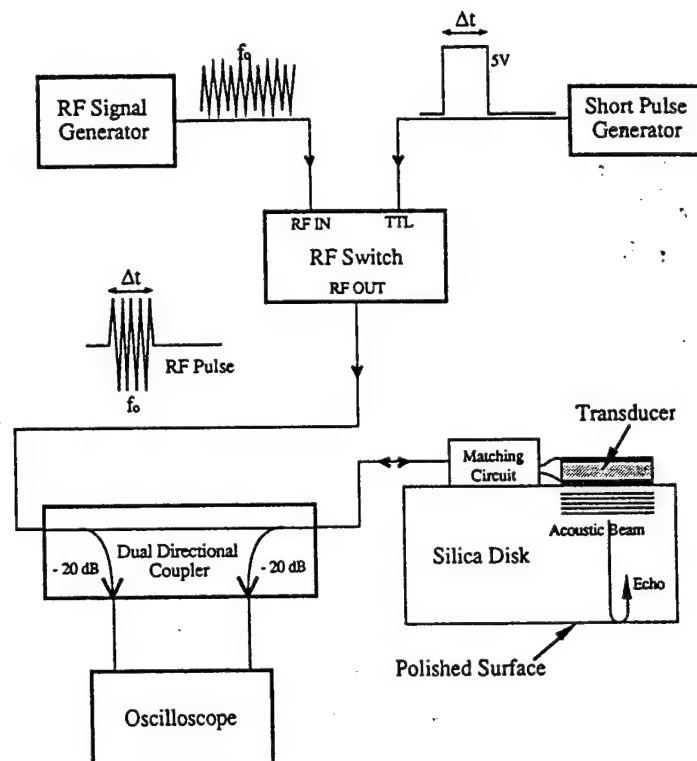
Finally, we built a in-fibre acoustooptic phase modulator, and a curved graded index acoustooptic switcher-connector.

## I PULSE-ECHO TECHNIQUE FOR INSERTION LOSSES EVALUATION

As previously stated, the piezoelectric activity of a transducer is directly related to its ability to function as a converter of electrical to mechanical energy. Unfortunately, because of transduction losses, only a part of the incident electric energy is converted to mechanical energy. Therefore, it is essential to evaluate the conversion losses of the ZnO transducers, because they give indication on the film structure, and on the piezoelectric behaviour of the transducer. The principle of pulse-echo technique is quite simple. It consists of applying an RF pulse on a transducer deposited on a well polished plate. The acoustic wave generated by the transducer is then reflected at the bottom face of the propagation medium, and induces an electric signal thanks to the inverse piezoelectric activity of the transducer. The conversion losses are estimated by measuring the relative amplitudes of the incident and reflected signals.

### I-1 Basic considerations on pulse-echo technique.

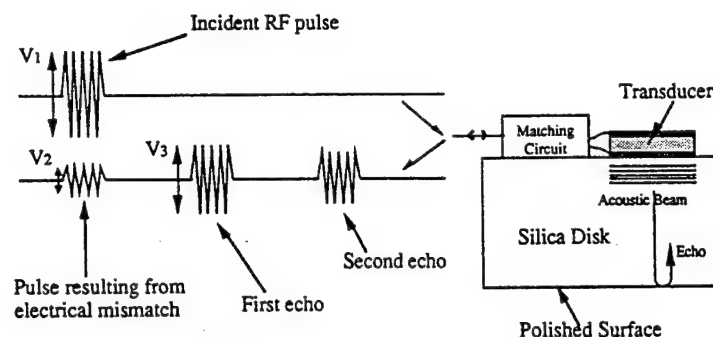
The experimental set-up is shown below.





An RF switch connected to a RF generator and triggered by a pulse generator is used to obtain short RF pulses (few tens of ns). Using a dual directional coupler, it is possible to display the incident pulse as well as the signals reflected by the transducer on a digitizing oscilloscope.

In the basic case, neglecting acoustic propagation losses, the insertion losses can be calculated as follows.



We call  $V_1$  and  $R$  the amplitude of the incident electric pulse and the radiation resistance of the transducer respectively. The electric power applied to the transducer is:

$$P_i^0 = \frac{V_1^2}{R}$$

But in the real case, a part of the incident pulse is reflected by the transducer due to electrical mismatch. Let  $V_2$  be the amplitude of that reflected pulse. The electric power effectively sent into the transducer is:

$$P_i = \frac{V_1^2 - V_2^2}{R}$$

We can then define an electric transmission coefficient  $T_e$  equal to:

$$T = \frac{P_i}{P_i^0} = 1 - \frac{V_2^2}{V_1^2}$$

This electric power sent into the transducer is converted into acoustic power via the efficiency coefficient  $\eta$ :

$$P_a = \eta P_i$$

The acoustic insertion losses are defined as  $-10 \log(\eta)$  expressed in dB / transduction. The acoustic wave travels through the plate and is reflected back to the transducer where it is converted into an electrical signal; the first echo. Let  $V_3$  be the amplitude of the first echo. Therefore, the power corresponding to that first echo is:

$$P_{out} = \eta^2 (1 - V_2^2 / V_1^2) P_i = \frac{V_3^2}{R}$$

Hence, the efficiency coefficient can be estimated by:

$$\eta = \frac{V_1 V_3}{V_1^2 - V_2^2} \quad (1)$$

## **I-2 Advanced considerations on the calculation of the transduction losses.**

In the last section, we have shown how it is possible to evaluate the transduction losses by considering the incident and the reflected electric pulses. We have assumed that there were no acoustic losses in the propagation medium, and that there were no losses when the acoustic field was reflected at the back face of the propagation medium. But, we have to keep in mind two important parameters.

Firstly, the acoustic propagation losses are proportional to the square of the frequency. Since the devices are operating in the range of few hundreds of MHz, the acoustic propagation losses can not be neglected.

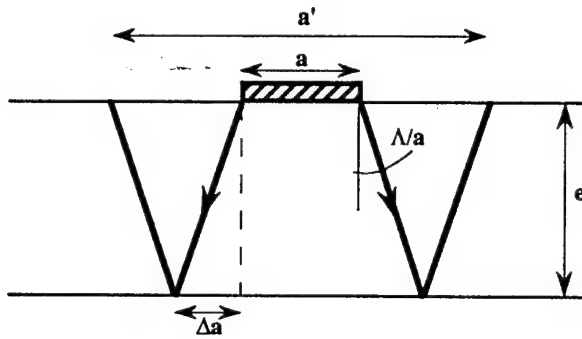
Secondly, we have considered that all the acoustic power generated by the transducer was reflected back, inducing inverse piezoelectricity. This could be true by considering there is no acoustic diffraction (the reflection at the interface plate-air is considered to be perfect). The problem is that the electrodes we use are very small. Therefore, the acoustic field is not perpendicular to the transducer plan, but exhibits an angular divergence related to the electrodes dimensions (see Part I). After reflection, only a part of the incident acoustic field will induce inverse piezoelectricity in the transducer.

In this section, we examine these effects to include them in the determination of the transduction losses.

### I-2-1 Effect of the acoustic diffraction on the reflected power.

In part I, we have already mentioned that an acoustic field exhibits an angular divergence related to the transducer dimensions. This angular divergence is due to diffraction. In the case of optical waves, diffraction occurs when the light is emitted by a aperture considered small compared to the optical wavelength (typically few microns). Since the acoustic wavelength is much larger than the optical wavelength, diffraction occurs with acoustic sources exhibiting larger dimensions.

Since the transducer dimensions are small, we have to take the problem of acoustic diffraction into account when calculating the transduction losses. In the following, we consider only rectangular transducers. The following figure represents an acoustic field propagating in a medium whose thickness is  $e$ .



It can easily be seen that because of diffraction, only a part of the emitted acoustic field induces inverse piezoelectricity after reflection at the end of the device. Let  $a$  be the extension of the acoustic field emitted by the transducer. The diffraction angle is  $\Lambda/a$ . Therefore, the extension of the reflected acoustic field is:

$$a' = a + 4\Lambda a$$

The electrodes we use are rectangular ( $a \times b$ ). The emitted acoustic power  $P_a$  is induced by a surface  $S_0 = a \times b$ . After one double traversal, the same acoustic power is contained in a larger surface  $S'_0 = a' \times b'$ . Neglecting the term involving  $\Lambda^2$ , this new surface is:

$$S'_0 = S_0 [1 + 2\Lambda e (1/a^2 + 1/b^2)]$$

The acoustic power inducing inverse piezoelectricity is then  $P'_0 = P_0 \times (S_0 / S'_0)$ . Therefore, we define an acoustic reflection coefficient as follows:

$$R_a = \frac{P'_0}{P_0} = \frac{1}{1 + 2 \Lambda e (1/a^2 + 1/b^2)} \quad (2)$$

The following table gives the value of  $R_a$  for the different electrode sizes we intend to use. We have  $e = 1 \text{ mm}$ , and  $\Lambda = 18.4 \text{ } \mu\text{m}$ .

Electrode	Dimensions (mm)	Reflection coefficient
1	$0.5 \times 0.573$	<b>0.794</b>
2	$0.5 \times 0.644$	<b>0.809</b>
3	$0.5 \times 0.716$	<b>0.820</b>
4	$0.5 \times 0.788$	<b>0.829</b>
5	$0.5 \times 0.859$	<b>0.835</b>

The above table shows how it is important to consider the acoustic diffraction when the electrodes are small.

### I-2-2 Acoustic propagation losses.

The second problem to consider concerns the acoustic propagation losses. When an ultrasonic wave propagates in a medium, it produces a periodic series of warmer compressed regions, and cooler rarefied regions [1]. The energy is conducted away from the ultrasonic wave and is transferred to the thermal modes of the medium, producing entropy. Since entropy-producing mechanisms are not reversible, this result in the attenuation of the ultrasonic wave. Because the energy transfer is periodic, the acoustic attenuation depends on the acoustic frequency. Generally, acoustic losses are defined as follows.

$$\gamma = \Gamma / f^2 \quad \text{expressed in dB/cm.GHz}^2$$

where  $\gamma$  and  $\Gamma$  are the frequency dependent and intrinsic attenuation respectively.

After a propagation length  $L$ , the acoustic power is attenuated as:

$$P(L) = P(0) \times 10^{-(\gamma f L/10)} \quad (3)$$

with  $L$  expressed in cm, and  $f$  in GHz.

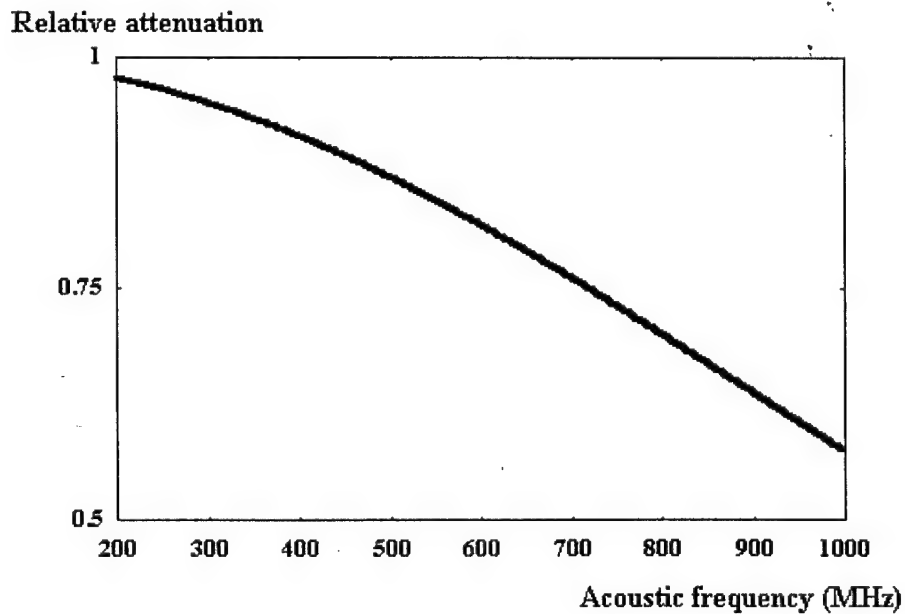
For fused silica (material on which the transducers are tested) the losses are:

$$\gamma = \Gamma / f^2 = 12 \text{ dB/cm.GHz}^2$$

The silica slabs we use are 1 mm thick. Therefore, the acoustic power attenuation (ratio  $P(L) / P(0)$ ) for a double traversal is;

0.966	at	250 MHz
0.87	at	500 MHz
0.73	at	700 MHz.

The curve below shows the evolution of the acoustic attenuation as a function of the frequency.



### I-2-3 Transduction losses.

If we take into account the acoustic diffraction and the propagation attenuation, the efficiency coefficient defined in equation (1) can then be expressed as:

$$\eta = \frac{V_1 V_3}{V_1^2 - V_2^2} \sqrt{1 + 2 \Lambda e (1/a^2 + 1/b^2)} 10^{(\gamma f e/5)} \quad (4)$$

### I-3 Experimental results.

ZnO transducers have been deposited on fused silica disks. Both faces of the disks are perfectly polished and cleaned. The bottom electrode (in direct contact with the silica disk) consists of a 200 nm thick aluminium layer. ZnO film was then sputtered (typically to a few  $\mu\text{m}$  thickness, corresponding to resonant frequencies of a few hundreds of MHz). Top electrodes (of about 200 nm Cr/Au) of different areas were evaporated through a copper etched mask. Figure 1 shows microscope pictures of the copper etched mask, and electrodes evaporated through it.

The device was then ready to be mounted in an electrical housing. This housing was design around the need to have the silica disk backed with air, in order to improve the acoustic reflection at the end of the device. Figure 2 shows a schematic diagram of the device. The transducer was glued into the central cylindrical hole. SMA connectors coupled the input signal to any necessary matching circuit (the problem of electric matching will be discussed further). One of the many devices we built is shown in figure 3. In order to measure the transduction losses of the transducers, we constructed the pulse-echo rig shown on figure 4.

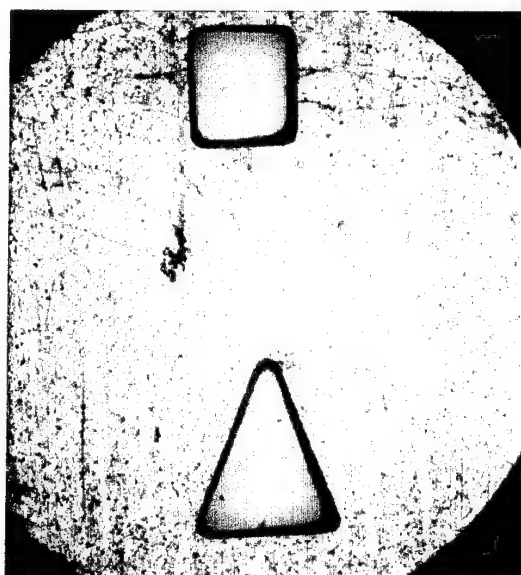
Figure 5 shows an oscilloscope trace of the incident and reflected pulses obtained when testing an electrically matched transducer resonating at 761.6 MHz. The amplitudes of the different voltages are:

$$V_1 = 36.2 \text{ mV} \quad V_2 = 13 \text{ mV} \quad V_3 = 9.9 \text{ mV}$$

The transducer characteristics are:

Resonant frequency	$f = 761.6 \text{ MHz}$
Acoustic wavelength	$\Lambda = 6.96 \mu\text{m}$
Electrode width	$a = 250 \mu\text{m}$
Electrode length	$b = 2.8 \text{ mm}$

a)



b)

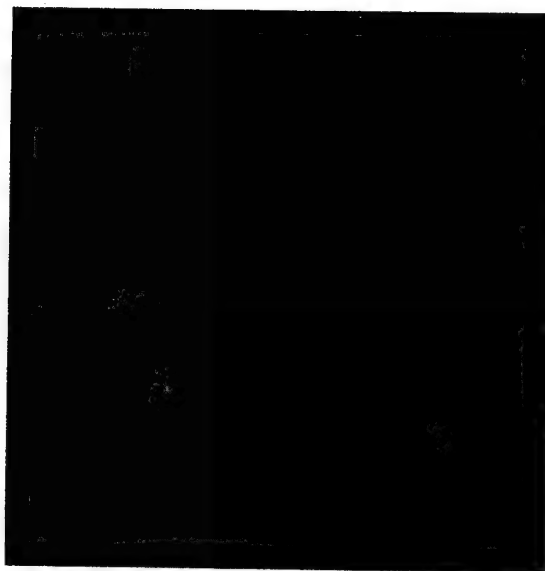


Figure 1: Top electrodes evaporation  
a) Copper etched mask  
b) Gold electrodes ( $0.5 \times 0.57$  mm)

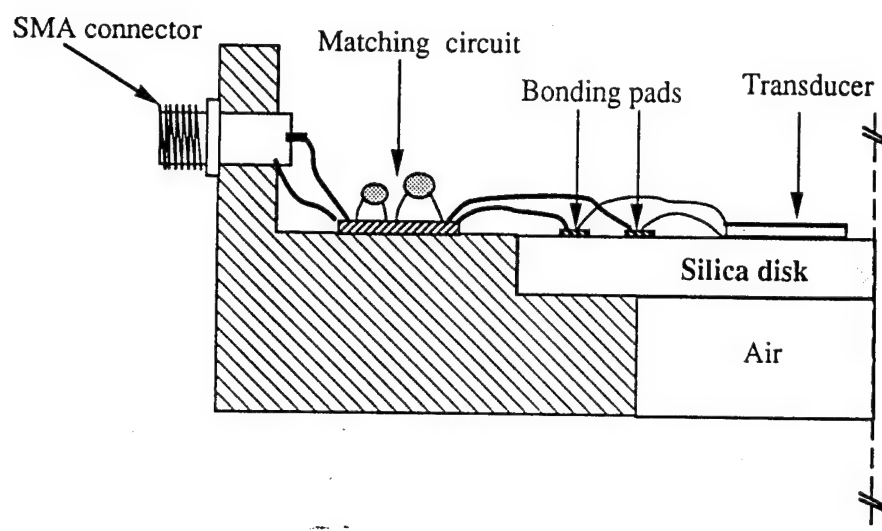


Figure 2: Schematic diagram of the device used for pulse-echo measurements

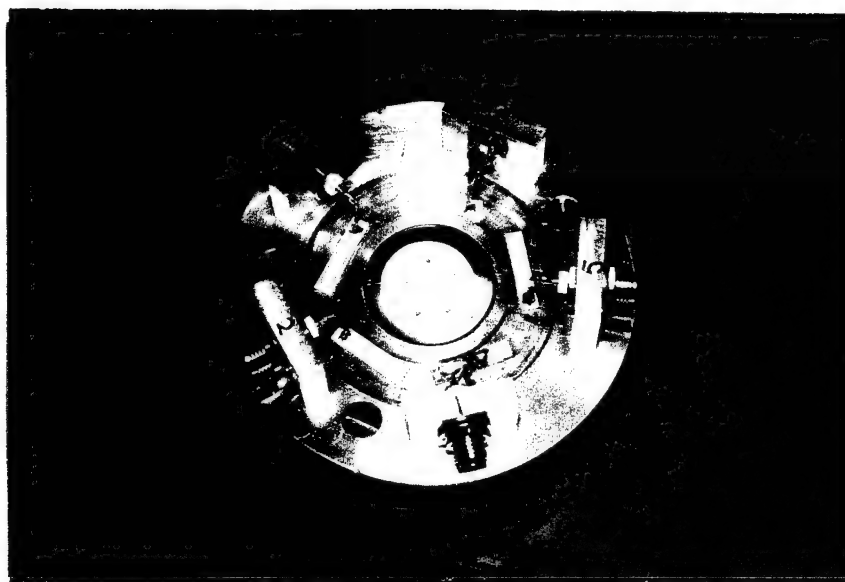


Figure 3: Example of device built for pulse-echo measurements (in this case we have evaporated circular electrodes)



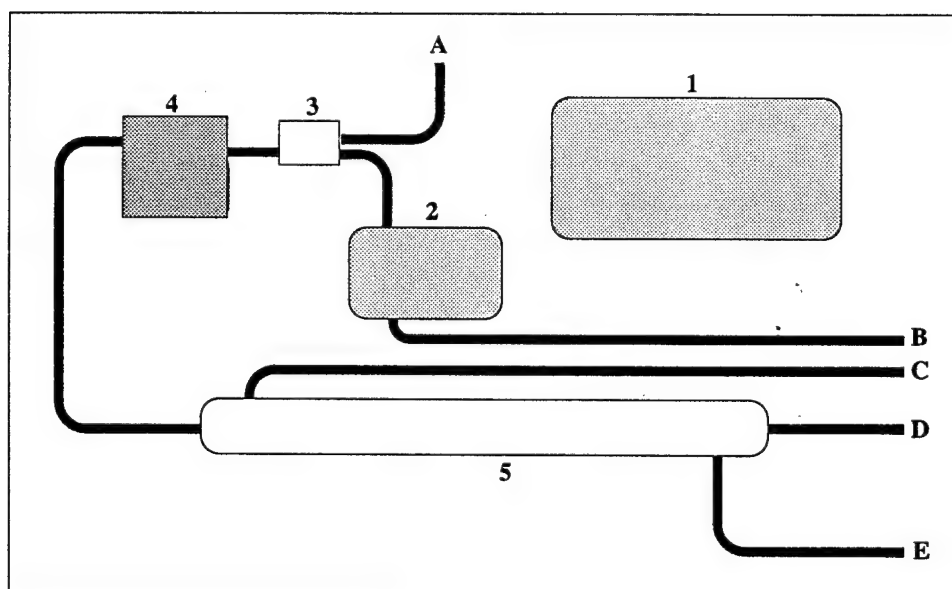
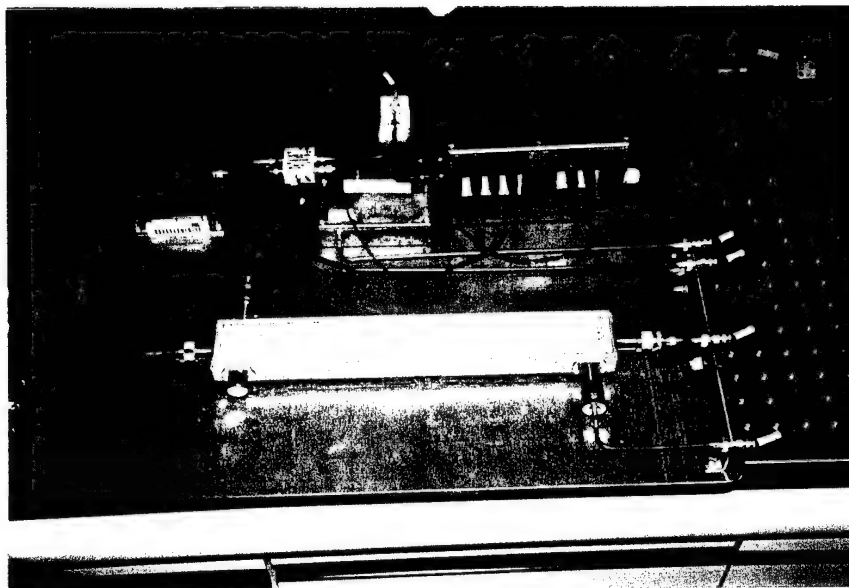


Figure 4: View of the pulse-echo experiment we built

- |                                |                                   |
|--------------------------------|-----------------------------------|
| 1- Main electric supply        | 2- Pulse generator                |
| 3- RF switch                   | 4- RF amplifier                   |
| 5- Dual directional coupler    |                                   |
| A- RF input                    | B- Trigger output                 |
| C- Incident pulse (to scope)   | D- Incident pulse (to transducer) |
| E- Reflected pulse ( to scope) |                                   |

Therefore, equation (4) leads to the efficiency coefficient:

$$\eta = 0.478$$

And then the transduction losses are:

$$- 10 \log (\eta) = 3.2 \text{ dB}$$

We conclude that the transducers we build exhibit very low losses.

We have also tested an unmatched transducer to evaluate the effect of acoustic attenuation and acoustic diffraction. The result is shown on figure 6 where several successive echoes can be seen. The ZnO film was  $9.205 \mu\text{m}$  thick (expected resonant frequency equal to 288 MHz). Because of the non piezoelectric layer we discussed in the previous part, the real resonant frequency is 332.5 MHz. The electrode dimensions were  $0.5 \times 0.573 \text{ mm}$ . Theoretically, the losses due to acoustic attenuation and diffraction are:

$$\text{theoretical losses} \quad 1.15 \text{ dB per double traversal}$$

On figure 6, the voltages corresponding to the two first echoes are  $V_3 = 8 \text{ mV}$ , and  $V_4 = 7 \text{ mV}$  respectively. Therefore, the power attenuation between those two consecutive pulses is:

$$\eta = \frac{V_4^2}{V_3^2} = 0.766$$

leading to:

$$\text{measured losses} \quad 1.16 \text{ dB per double traversal}$$

which is in good agreement with the theoretical value.

Moreover, the average time gap (336.5 ns) between two successive reflected pulses leads to an acoustic velocity in fused silica of 5944 m/s which is also in good agreement with the theoretical value of 5970 m/s.

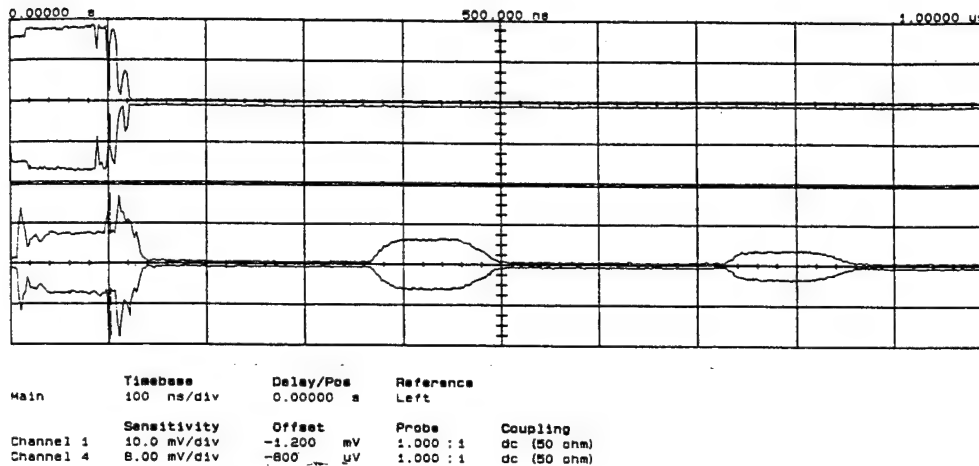


Figure 5: Experimental result obtained with an electrically matched transducer. In this case, the transduction losses are 2.84 dB.

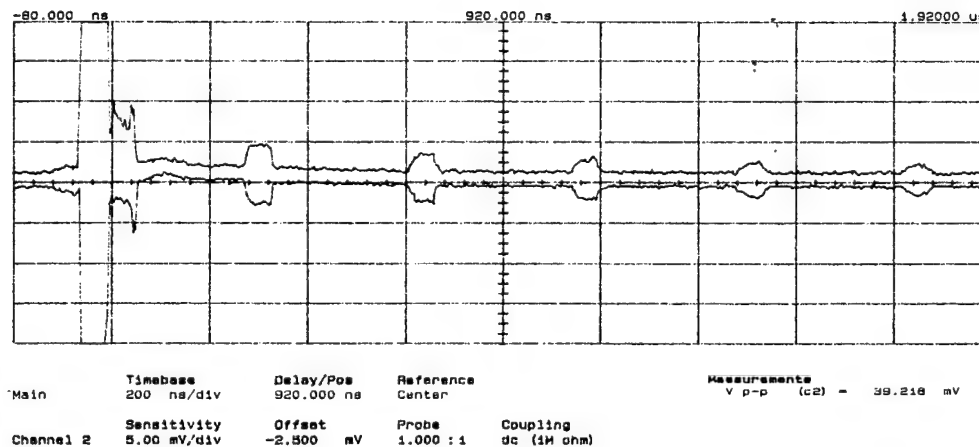


Figure 6: Successive echoes reflected by an unmatched transducer. The power decrease between the two first echoes corresponds to 1.16 dB (the theoretical value is 1.15 dB).

#### I-4 Conclusion.

We have presented theoretical and experimental results concerning pulse-echo experiments that have been carried out. We have shown that the transducers we build exhibit very low transduction losses (approx. 3 dB). We have seen that when the electrodes are small compared to the acoustic wavelength, it is important to take into account the problem of acoustic diffraction. Because the acoustic attenuation depends on the square of the frequency, and since the transducers are of low loss, the acoustic propagation losses have also to be considered.

We have also briefly mentioned the problem of electrical impedance matching. The following section discuss this problem in detail.

## II PROBLEM OF ELECTRICAL IMPEDANCE MATCHING.

### II-1 Why is it important to rematch ZnO transducers ?

We have already mentioned the problem of electric impedance matching. In the first part of this report, we have used the electric impedance of the transducer to determine its dimensions. The problem is that even if the transducer possesses the optimum area for the transducer impedance to be equal to  $50 \Omega$ , it often has to be electrically rematched. There are several reasons leading to a wrong transducer electric impedance.

The electromechanical coupling constant can be different for the sputtered film than for the bulk ZnO.

The acoustic impedance (related to the film density and the acoustic velocity) can differ from the theoretical value.

Because of the non-piezoelectric layer appearing at the beginning of the deposition process, the real resonant frequency is different than the expected one, leading to a different transducer impedance.

The permittivity of sputtered ZnO film is usually different from the bulk value (for example, the refractive index is different).

Of course, the values of these different parameters differ little between the bulk material and sputtered films. But, since the electric impedance strongly depends on these values, the real electric impedance can be different enough from the ideal  $50 \Omega$  to dramatically reduce the diffraction efficiency of the acoustooptic modulator. The following section explains how to match a piezoelectric transducer, regardless of the transducer geometry.

## II-2 Electrical matching of piezoelectric transducers.

Driving an electrical system at RF frequencies requires accurate impedance matching between the RF drive source and the system under investigation. Any impedance mismatch between the two results in the reflection of a significant portion of the incident RF signal. Such reflections are detrimental to piezoelectric transducer operation efficiency because it results in a much lower signal power actually reaching and driving the transducer than originally applied.

Most RF generators are coupled to  $50\ \Omega$  at their outputs. Hence it is necessary to tune/electrically match the input impedance of any piezoelectric transducer under RF excitation to be purely resistive (at  $50\ \Omega$ ) at the drive frequency in order to achieve maximum operation efficiency.

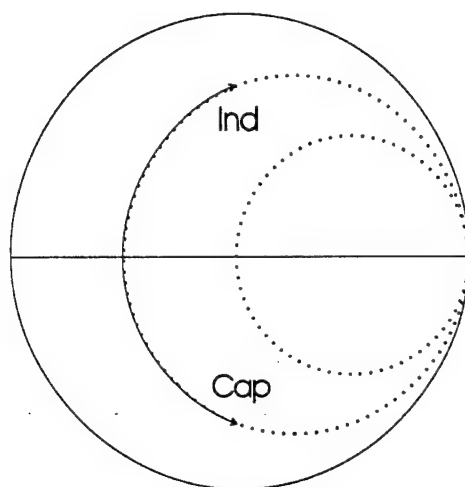
At resonance, a piezoelectric transducer becomes almost purely resistive, its only reactive element arising from its intrinsic capacitance (due to the different values of the sputtered films characteristics as explained in the last section), and any capacitance or inductance contained in the electrical connections to the transducer electrodes.

To counteract this residual reactance, it is necessary to insert capacitance and/or inductance in parallel and/or series with the transducer configuration. By selecting the correct combination of compensating reactive components, one can tune out the residual reactance at the resonant frequency and boost or decrease the intrinsic resistance of the transducer at resonance to match the  $50\ \Omega$  output impedance of the RF drive source.

In the matching of our transducers we have employed the following guidelines (based on the Smith chart interpretation of the spectral impedance of transducers) to determine the compensation components required to achieve a good electrical match.

- (1) Adding a series inductor moves a point on the Smith chart clockwise along a circle of constant resistance. A series capacitor moves the point counterclockwise. An illustration is given on figure 7-a.
- (2) Adding a parallel inductor moves a point anticlockwise along a mirror image of the circle of constant resistance. A parallel capacitor moves the point clockwise (see figure 7-b).
- (3) With series impedances a low value (*i.e.* large capacitance or small inductance) moves the point by small amount, while with parallel reactances a large value (*i.e.* small capacitance or large inductance) is required to change the point minimally.

a)



b)

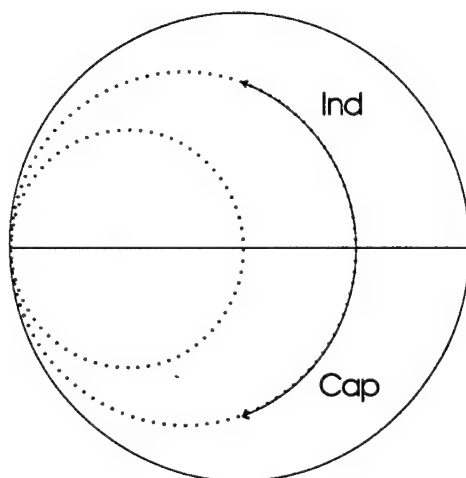


Figure 7: Moving a point on the Smith chart to match a transducer  
a) By using series inductor or capacitor  
b) By using parallel inductor or capacitor

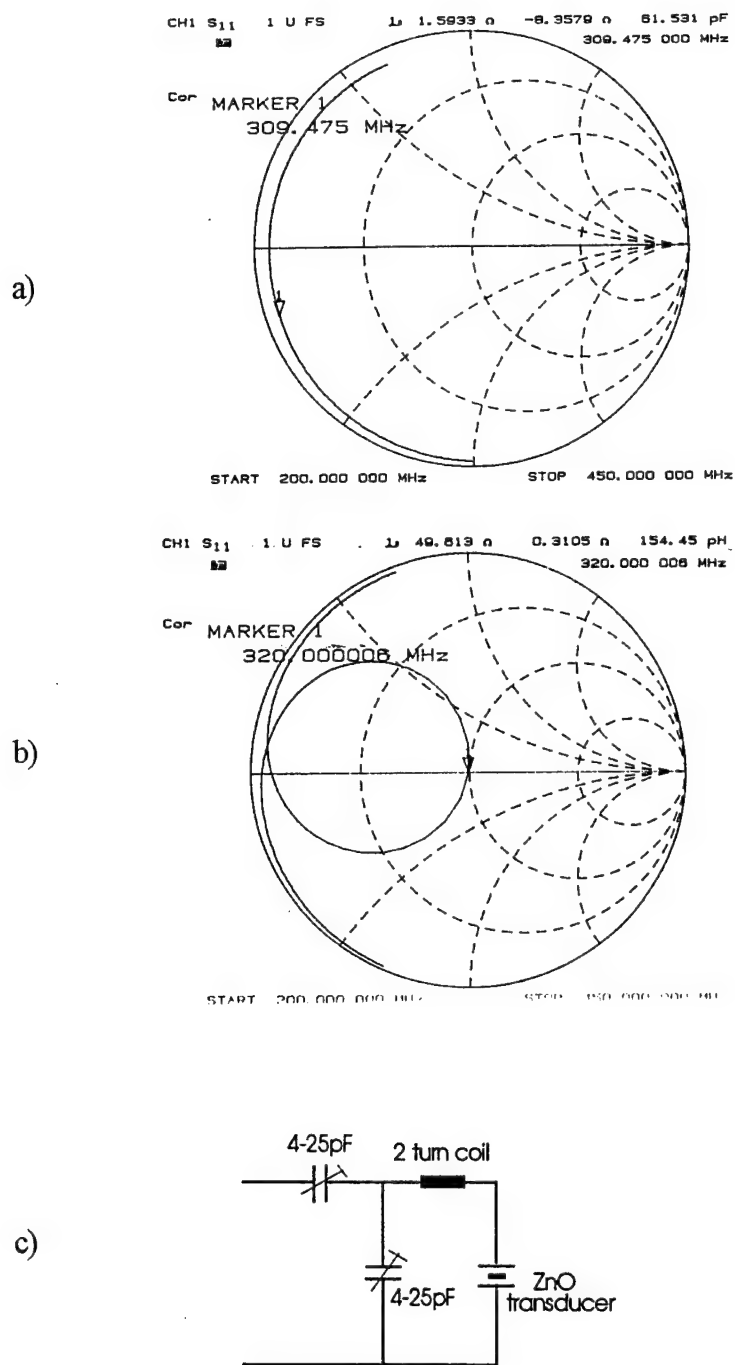
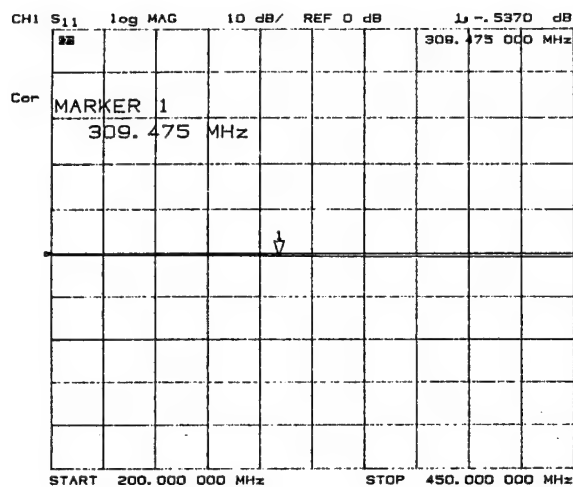


Figure 8: Smith charts of a planar ZnO transducer

- a) Before matching
- b) After matching
- c) Circuit used to match the transducer

a)



b)

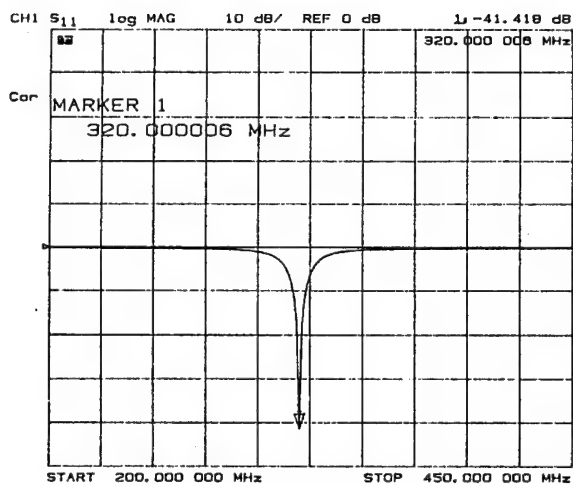


Figure 9: Reflection losses at the resonant frequency  
 a) Before matching  
 b) After matching



Using the above guidelines, one can oscillate a point to and fro on the Smith chart until it is centred on the  $50\ \Omega$  zero reactance centre point. Figures 8-a and 8-b show the Smith charts of a ZnO planar transducer before and after matching, where the circuit shown on figure 8-c was used to tune the device to  $50\ \Omega$  at its resonant frequency of 320 MHz. The dramatic effect that the matching circuit has on the reflection losses at this frequency is illustrated by figures 9-a and 9-b. These diagrams show that before matching almost all of the incident RF power is being reflected at 320 MHz, while afterwards a reflection loss of -41 dB has been achieved, indicating that effectively all incident RF power now reaches the transducer.

### II-3 Conclusion

We have shown the importance of the electric impedance matching. Even if the transducer exhibits the ideal area, leading to a theoretical impedance of  $50\ \Omega$ , it is necessary to rematch because ZnO characteristics are slightly different for sputtered than for the bulk material. Electrical matching can easily be achieved by using a simple electrical circuit, leading to reflection losses of minus a few tens of dB. While matching our transducers, we observed that it was possible to obtain reflection losses of less than -15 dB for non-resonant frequencies. Of course, the reflection losses reach their maximum at the resonant frequency. We have also noticed that it was easy to match transducers whose areas were different from the ideal area calculated to match the transmission line impedance. In this case, the diffraction efficiency is decreased because the electric energy is dissipated in the matching circuit. It is only when the transducer exhibits the correct area that all the incident electric energy is used to induce acoustic waves. Therefore, even if the electrical matching is relatively easy to achieve, it remains of great importance to precisely control the transducer area.

### III ACOUSTOOPTIC INTERACTION IN A $\text{TeO}_2$ CRYSTAL

As previously stated,  $\text{TeO}_2$  is an efficient acoustooptic medium due to its large  $M_2$  figure of merit ( $4.24 \times 10^{-15}$  against  $1.47 \times 10^{-15}$  for fused silica). We have built planar acoustooptic modulators using  $\text{TeO}_2$  crystals. The purpose of this work was to increase our knowledge of the acoustooptic interaction using ZnO transducers at frequencies of about few hundreds of MHz.

This acoustooptic modulator consists of a  $\text{TeO}_2$  crystal having its bottom face angled with respect to the face on which the transducer is deposited. This angle means that the reflected acoustic waves do not induce inverse piezoelectricity in the ZnO transducer. It is easily understood that such echoes would reduce the efficiency of the acoustooptic modulator. The crystal was then glued between grounded aluminium plates, and these plates were screwed on the special housing provided by Gooch & Housego Ltd, which incorporates the electric matching circuit. We built several modulators with resonant frequencies ranging between 250 and 350 MHz. Figure 10 shows one of the acoustooptic modulators in its housing.

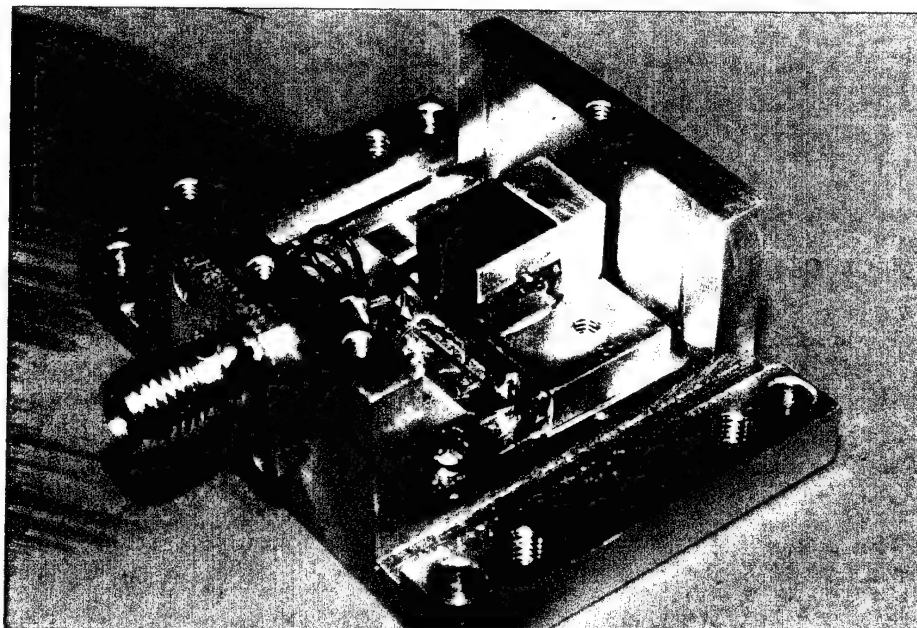


Figure 10: View of a planar  $\text{TeO}_2$  modulator. We can see the electrical matching circuit.

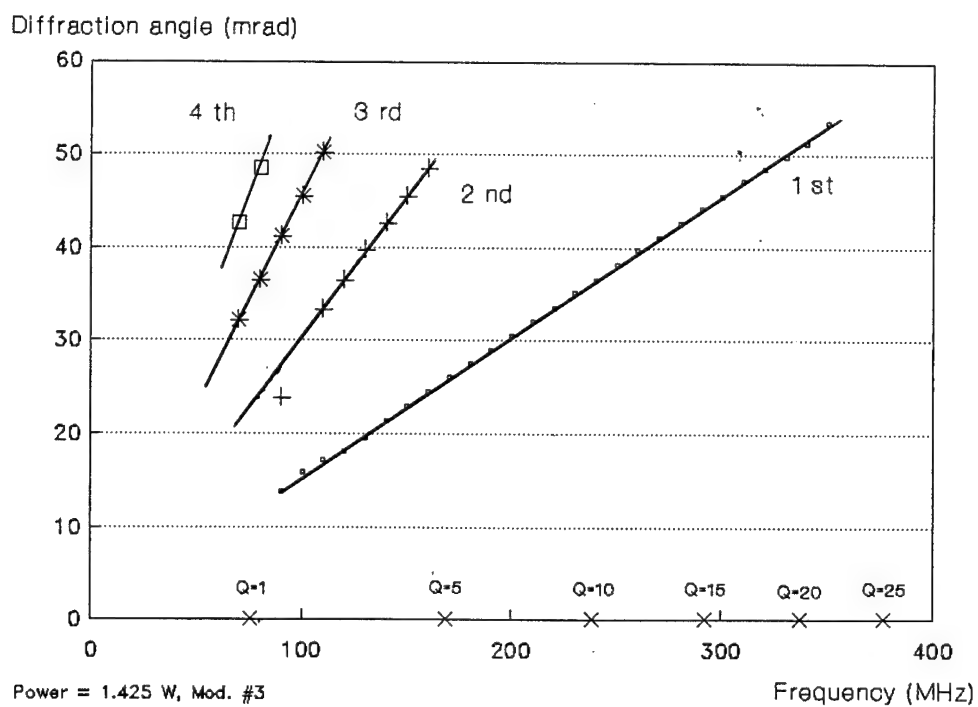


Figure 11: Diffraction angles of the first diffraction orders as a function of the applied frequency.

The modulators were mounted on micropositioners allowing translation along three directions, and rotation around two axes in order to perfectly orient them so that the light is incident at the Bragg angle in the interaction region. We have tested the transducers by using a conventional HeNe laser (wavelength  $\lambda = 633$  nm).

### **III-1 Dependence of the regime of operation with the applied electric frequency.**

In part I, we have mentioned that the regime of operation is related to the Q factor which involves the transducer length, the optical and the acoustic wavelength. We have tested the modulators at frequencies ranging from 100 to 400 MHz. We have noticed that even far below the resonant frequency, it was still possible to observe optical diffraction. Of course, far from the resonant frequency, the diffraction efficiency is very low (less than 5%).

Figure 11 shows the diffraction angles of the four first orders of diffraction as a function of the applied frequency. This result was obtained with the modulator n° 3 (resonant frequency 302 MHz) with an applied RF power of 1.425 Watts.

The diffraction efficiency was maximum at the resonant frequency. When increasing the applied frequency, the diffraction efficiency decrease quickly, so that no acoustooptic diffraction can be observed at frequencies higher than 350 MHz. When decreasing the applied frequency from 350 MHz to 200 MHz, the Q factor remains large enough for the device to operate in the Bragg regime as it can be seen in figure 11 where only the first order diffracted beam is obtained. When the applied frequency is less than 200 MHz, the Q factor is less than 5 indicating that the device operates in the Raman-Nath regime. The different diffraction orders can be seen on figure 11. Only the four first orders are plotted, but the 7<sup>th</sup> order was obtained for frequency less than 90 MHz. Of course, at such low frequencies, the diffraction efficiency was very low. Nevertheless, figure 11 demonstrates the ZnO transducers work well. We conclude that the Q factor has to be equal or greater than 5 for the device to operate in the Bragg regime.

In part I, we have shown that the diffraction angle depends on the acoustic wavelength (*i.e.* the acoustic velocity in the interaction medium). The velocity of sound in TeO<sub>2</sub> is determined by measuring the slopes of plots corresponding to the different diffraction orders. The average measured acoustic velocity is  $4217^{+44}$  m/s which is in good agreement with the theoretical value of 4260 m/s.

### **III-2 Diffraction efficiency, rise time, and bandwidth.**

For this second set of experiments, we used a different modulator. The modulator used in the last section had been damaged by applying a high power continuous drive signal. We then decided to pulse the modulators to reduce the risk of damaging the ZnO transducers. The resonance frequency of this modulator is 214 MHz, where the modulator operates in the near Raman-Nath regime (the second order was visible).

The modulator was driven with 0.55 ms pulses and a repetition time of 1.2 ms. Figure 12-a shows the diffraction efficiency as a function of the average applied power. The curve represents the theoretical diffraction efficiency calculated with a computer program provided by Gooch & Housego Ltd, while the dots are the experimental results. We observe that our experimental results are a bit lower than the theoretical values. This is probably due to the fact that the theoretical calculation is based on a device operating in the Bragg regime, which is not the case. The intensity of the first order diffracted beam is lower in our device than the intensity of the same order in the Bragg regime, because a part of the diffracted energy contributes to the other Raman-Nath orders.

The optical beam diameter we used for the theoretical curve in figure 12-a was determined by the measurement of the rise time of the device shown on figure 12-b. The 10 to 90 % rise time of 196 ns observed on figure 12-b indicates a optical beam diameter of 1.28 mm, that explains the relatively low diffraction efficiency. The 572 ns response time between the applied RF pulse and the increase in the intensity of the diffracted beams indicates the distance from the ZnO transducer and the optical beam. According to a sound velocity of 4260 m/s in the  $\text{TeO}_2$ , this distance is 2.43 mm. It has been extremely difficult to position the beam as so to reduce this response time (by changing the laser beam position) because of the poor crystal quality.

The modulator bandwidth has also been tested. Figure 13-a represents the evolution of the diffraction efficiency with the applied RF frequency. It appears that the modulators, and hence the ZnO transducers, are broadband since the bandwidth is 8 MHz, for a central frequency of 214 MHz.

### III-3 Problem of the resonant frequency.

The transducers we have deposited on the  $\text{TeO}_2$  crystals are supposed to resonate at 250 MHz. In section III-1, we present a transducer resonating at 302 MHz. As previously stated, the discrepancy in the resonant frequency due to the problem of a disordered layer that appears at the beginning of the film growth. For the transducer used in section II-2, we tried to overcome the problem of the non-piezoelectric layer by increasing the deposition time by about 50 mn (we stated before that this non-piezoelectric layer was deposited during the first 50 mn of process). We then tried to rematch the transducer at its expected resonant frequency: 250 MHz. The -25.9 dB reflection loss at 250 MHz shown on figure 13-b (better than what we had at 214 MHz !) seems to indicate that we have succeeded. Unfortunately, the diffraction efficiency obtained at this frequency was lower than what we obtained at 214 MHz. This means that the electric energy is not dissipated in the ZnO film to induce acoustic waves, but in the matching circuit, resulting in a lower conversion efficiency. We think that it is due to the new Zn target we used for building these modulators. Since the Zn target has been changed, the deposition conditions may be slightly different, and the deposition rate a bit higher than before, yielding thicker films with lower resonant frequencies.

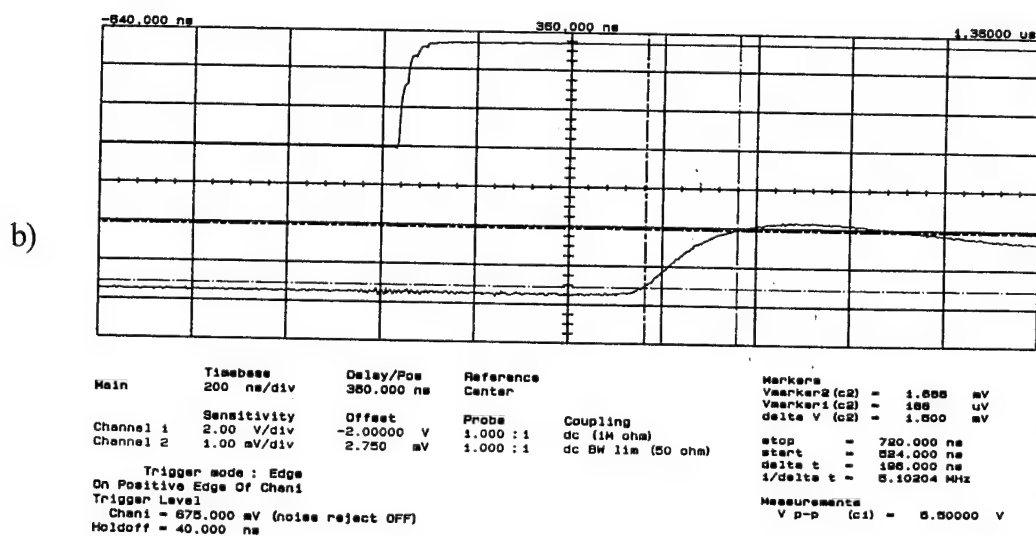
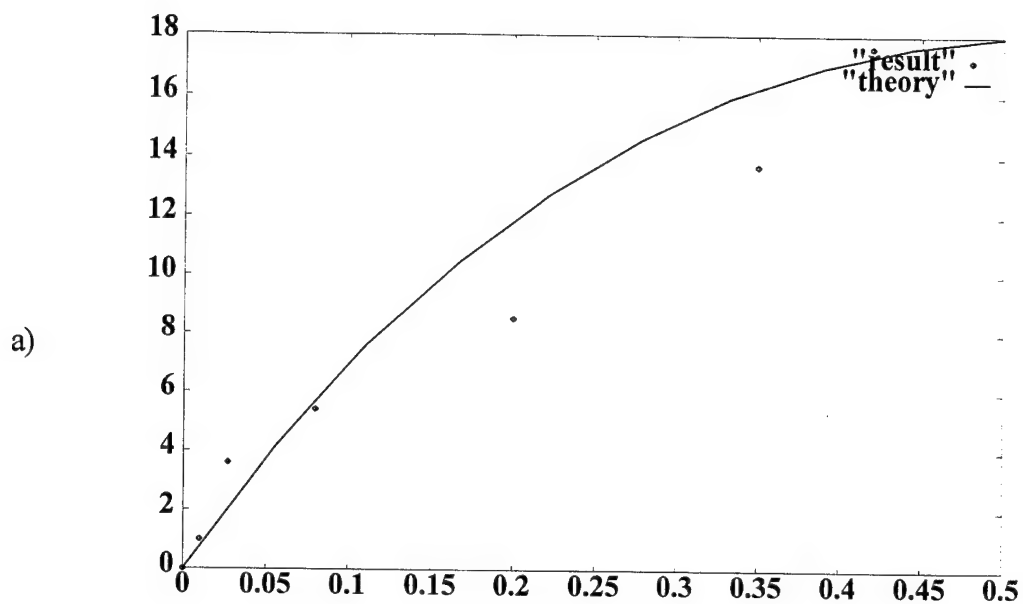


Figure 12: Acoustooptic behaviour of a ZnO/TeO<sub>2</sub> modulator  
 a) Diffraction efficiency versus average applied power  
 b) Measurement of the rise time

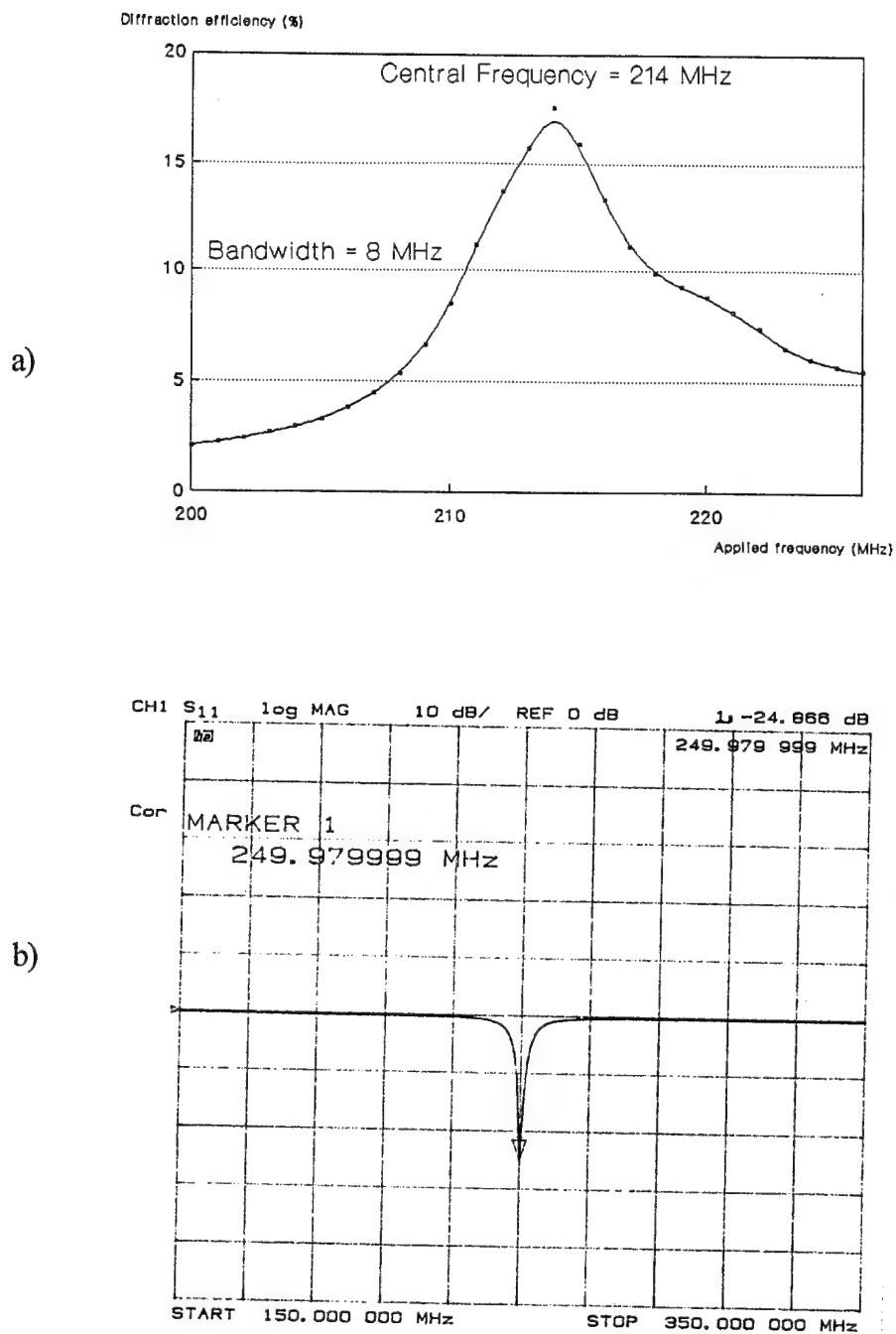


Figure 13: Acoustooptic behaviour of a ZnO/TaO<sub>2</sub> modulator

- a) Transducer bandwidth
- b) Reflection loss of a transducer matched at 250 MHz

### III-4 Conclusion.

We have presented the experimental results obtained with a  $\text{TeO}_2$  crystal that uses ZnO piezoelectric transducers to achieve acoustooptic diffraction. Diffraction efficiency as high as 17 % was obtained despite a beam diameter of 1.28 mm which is larger than the electrode width (0.4 mm). The ZnO transducers are broadband (8 MHz at -3 dB), and acoustooptic diffraction can be obtained with frequency as low as 90 MHz (for a resonant frequency of 302 MHz). Of course, since the Q factor is low at those frequencies, the device operates in the Raman-Nath regime, and about 7 order of diffraction were observed.

The next section deals with acoustooptic interaction in optical fibres. The important aspect of the following part is to test the efficiency of ZnO transducers sputtered on highly curved surfaces.

## IV OPTICAL PHASE MODULATION USING A FIBRE TRANSDUCER

The experimental arrangement for testing the fibre transducers for phase modulation is shown in figure 14. The transducer is spliced into a Mach Zehnder interferometer which operates at 1550 nm. A high frequency infra-red detector at either of the output arms is used to detect RF modulation of the input signal.

### IV-1 Theoretical considerations.

The basic theory of the Mach Zehnder interferometer is that at the output fibres, the light intensity is given by :

$$I = I_1 + I_2 + 2\sqrt{I_1 I_2} \cos \phi \quad (5)$$

where  $I_1$  and  $I_2$  are the intensities in the arms of the Mach Zehnder and  $\phi$  is the phase difference between these signals.

The phase shift is introduced by applying an RF signal to the transducer at its resonant frequency. From this signal the transducer generates a standing acoustic wave in the fibre which periodically modulates the fibre index in the region of the transducer. Hence the optical mode in the transducer arm is phase modulated by a signal which can be represented by:

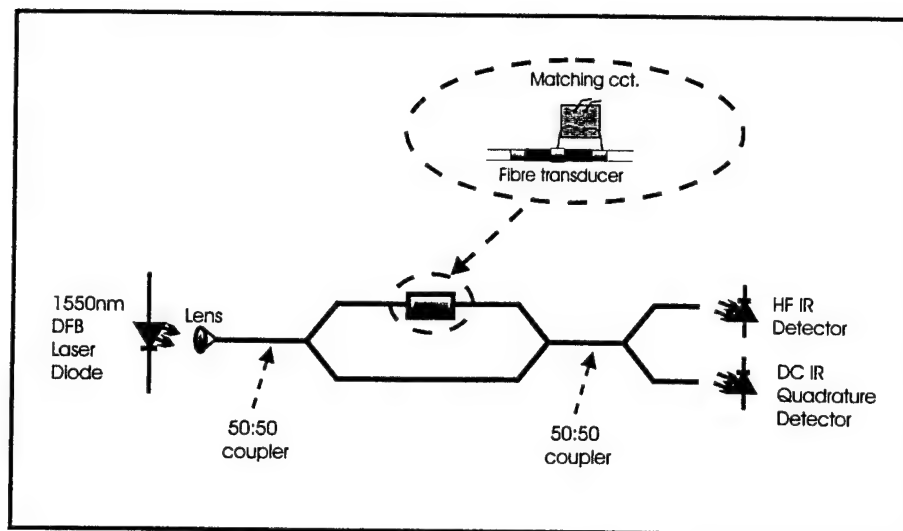


Figure 14: Experimental arrangement for testing the fibre transducer for phase modulation.

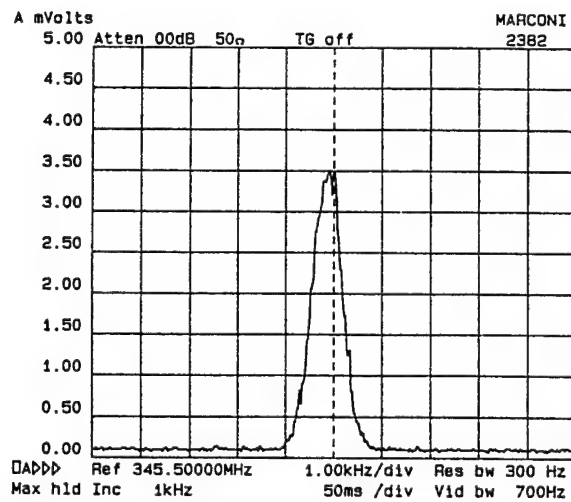


Figure 15: J1 modulation peak detected at the fundamental resonant frequency of the fibre transducer.



$$\phi = \beta \sin(w_{ac} t) \quad (6)$$

where  $w_{ac}$  is the frequency of the RF signal and  $\beta$  is the modulation index. The modulation index represents the phase modulation in radians and is given by:

$$\beta = \frac{2\pi}{\lambda_0} \Delta n d \quad (7)$$

where  $d$  is the length of the transducer,  $\lambda_0$  is the optical wavelength and  $\Delta n$  is the index modulation caused by the acoustic wave.

Combining equations (5) and (6) we can show that the expression for the intensity,  $I$  in either of the output arms is described by a Bessel function. Hence, any phase modulation is detectable as sidebands of the Bessel functions which occur at the RF signal frequency and its harmonics. The ratio of the J1 and J2 sidebands is used to solve for the modulation index as a function of applied power, from which the efficiency of the device can be derived.

## **IV-2 Experimental result.**

### **IV-2-1 Acoustooptic phase modulation in an optical fibre.**

Figure 15 shows the J1 modulation peak detected at the fundamental resonant frequency of 345.5 MHz of our fibre transducer. The magnitude of the induced phase shift is deduced from the ratio of the amplitude of fundamental signal to the amplitude of the first harmonic, J2. We plot the phase modulation in radians as a function of the square root of the input power. Figure 16 shows that with our fibre transducer, which is 0.8 mm long, an efficiency of 0.492 rad/ $\sqrt{W}$  was achieved for the wavelength  $\lambda = 1550$ nm. The poor signal to noise ratio causes a discrepancy in the measurements at low powers. Considering the reduced length of our transducer, this efficiency is more than twice as large as the efficiency of 1.48 rad/ $\sqrt{W}$  reported by Godil *et al*<sup>1</sup> from their 2mm long 180° transducer at 633 nm wavelength.

---

<sup>1</sup> A.A. Godil, *et al* "All-fiber Acoustooptic Phase Modulators Using Zinc Oxide Films on Glass Fiber" J. Lightwave Technology, Vol. 6, 1988, pp. 1586-1590

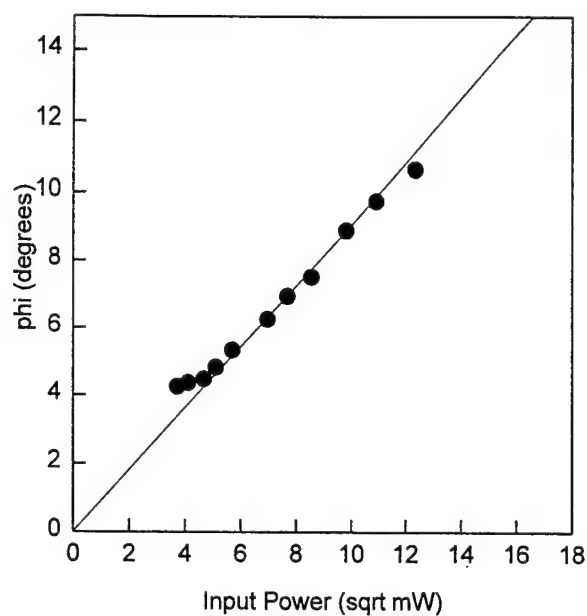


Figure 16: Phase modulation versus the square root of the input power. The transducer is 0.8 mm long and the efficiency is 0.492 rad/ $\sqrt{W}$ .

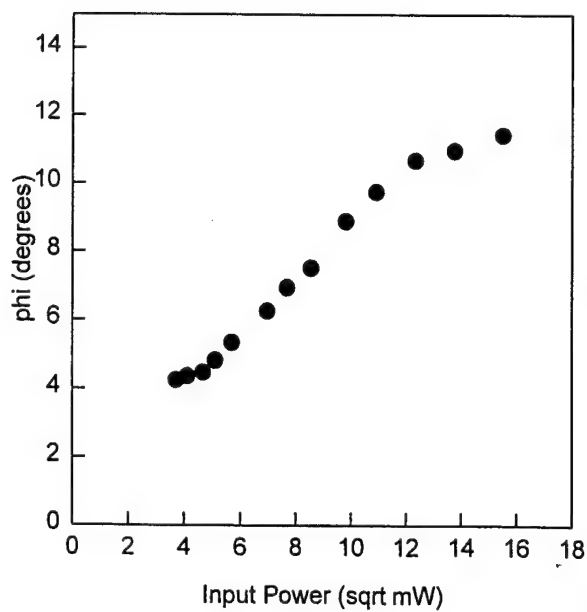


Figure 17: Effect of high powers on the transducers efficiency.

#### IV-2-2 Problem of maximum applied power.

For input powers above 144 mW the efficiency of our transducer degrades (see figure 17). It is possible that the device is overheating and that this is causing the structure to degrade. Indeed it was found that after having operated the transducer CW with an input power of 250 mW for 30 minutes the device had deteriorated considerably. Figure 18 shows the efficiency curve measured after the latter test and demonstrates that the device has lost its former characteristics. Although there is no visible damage to the transducer it is likely that overheating has caused irreversible damage to the piezoelectric properties of the transducer. To overcome this problem it will be necessary to devise a form of heat sinking for the device, which will then allow greater phase modulation to be achieved at higher input powers. The phase modulation may also be enhanced by increasing the length of the device. However the increased transducer area poses problems in the electrical matching of the device. We are currently experimenting with a 10mm long transducer with which we hope to achieve much larger phase modulation.

#### IV-3 Conclusion.

In the above discussion, we have presented theoretical and experimental results from an in-fibre acoustooptic modulator consisting of a ZnO transducer deposited directly on the highly curved surface of an optical fibre. Phase modulation of 0.492 rad/W has been achieved, which is to the best of our knowledge, the best result obtained with an in-fibre modulator. The phase modulation can be increased by applying more power, but the transducers degrade for applied powers greater than 200 mW. The phase modulation could also be enhanced by using longer ZnO acoustooptic modulator, provided that the electrical matching of the device remains possible.

This efficient phase modulator could be applied to various acoustooptic devices such as a mode-locked fibre laser or an in-fibre tunable gratings. It also demonstrates that it is possible to deposit ZnO on highly curved surfaces without sacrificing the piezoelectric behaviour of the transducer.

#### V ACOUSTOOPTIC MODULATOR USING A GRADIENT INDEX LENS.

The graded index acoustooptic modulator we have fabricated is based on a quarter pitch graded index lens with a quadratic index profile  $n(r) = n_0(1 - A r^2 / 2)$ , having on-axis index  $n_0 = 1.6075$ ,  $\sqrt{A} = 0.339 \text{ mm}^{-1}$ , and a numerical aperture (NA) = 0.46. The length of the lens is 4.63 mm and its diameter is 1.8 mm. The GRIN lens was supplied with a Cr/Au layer on the outer surface (thickness 700 nm), and antireflection coated for  $\lambda = 633 \text{ nm}$ . The lens was then mounted in a drilled brass block to reduce backward acoustic reflections and to provide good electrical contact with the bottom electrode of the modulator.

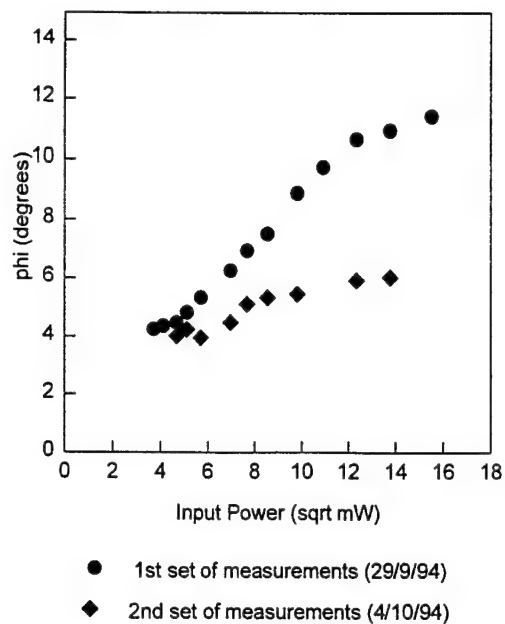


Figure 18: Deterioration of the efficiency after having operated the transducer CW for 30 mn.

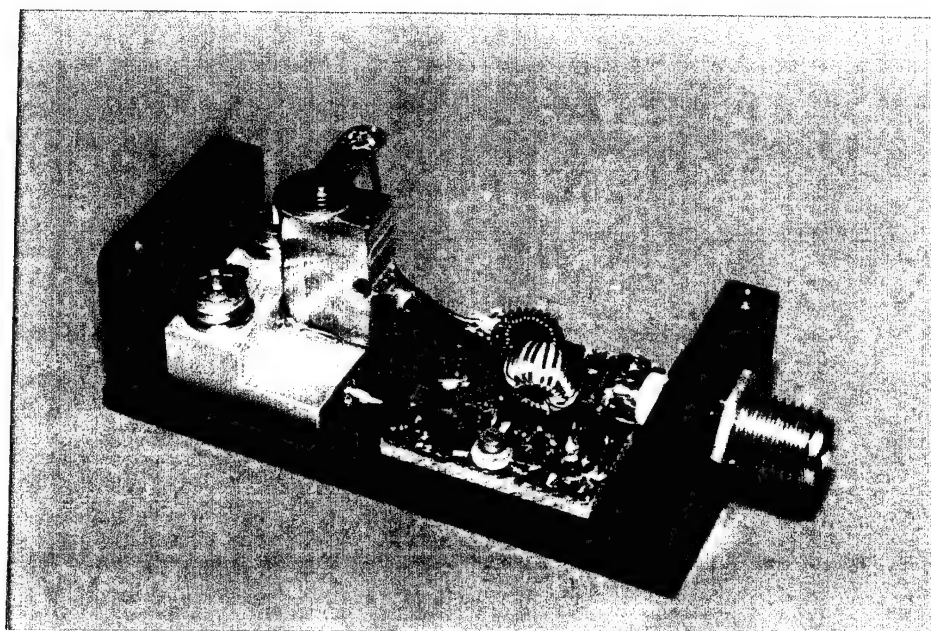


Figure 19: View of a low frequency planar graded index modulator fabricated at the ORC.

A 6.625  $\mu\text{m}$  thick ZnO film (resonant frequency of 400 MHz) was then deposited on the curved surface of the graded index lens. Finally, a top Cr/Au electrode was evaporated in the form of a stripe (0.2 $\times$ 3.5 mm) aligned directly above the exposed curved surface of the lens.

This device is currently being bonded and mounted in a conventional housing by Gooch & Housego Ltd. Therefore, the experimental results from this device will not be available before the end of November 1994. Nevertheless, from the good results obtained with the planar TeO<sub>2</sub> modulators and with the in-fibre acoustooptic phase modulators, we expect to obtain similar acoustooptic efficiency with this graded index device. Furthermore, a planar, low resonant frequency, graded index modulator has already been demonstrated in the ORC in 1993 (see figure 19). The main result from this device is that the rise time is low (14 ns), the diffraction process is not appreciably distorting the profile of the diffracted beams, and hence the imaging properties of the graded index lens are conserved.

## VI CONCLUSION.

In this part, we have presented experimental results concerning the piezoelectric activity of ZnO films. Different experiments were carried out to evaluate the transduction efficiency of the ZnO transducers, and also to investigate the behaviour of the acoustooptic devices we built.

In section I, we measured the transduction losses of the transducer by using a conventional pulse-echo technique. We enhanced this technique by accounting for the effects of acoustic diffraction and propagation loss. We concluded that the ZnO transducers we build are efficient, since the measured transduction losses are 3.2 dB.

We emphasized the problem of electrical matching in section II. In particular, we demonstrated that even if the transducer exhibits the ideal area (having an impedance of 50  $\Omega$ ), it is generally necessary to rematch the transducer because the characteristics of sputtered ZnO differ from the bulk material. We matched the different transducers we tested by using a HP network analyzer, and reflection losses as high as - 41 dB were obtained.

In section III, we presented a complete study of planar ZnO/TeO<sub>2</sub> acoustooptic modulators. The bandwidths of the transducers are of 8 MHz at -3 dB. However, it is still possible to observe acoustooptic diffraction far below the resonant frequency. Of course, since the Q factor is proportional to the applied frequency, several diffraction orders were observed for acoustic frequencies of about 90 MHz. The diffraction efficiency as a function of the applied power was measured and was in good agreement with theoretical calculations. An efficiency of 17 % was achieved with an applied RF power of 420 mW. The relatively low value of the diffraction efficiency is mainly due to the optical beam diameter which is large compared to the electrode width (1.28 mm for the optical beam against 0.4 mm for the electrode). Consequently, the rise time was quite high: around 196 ns.

We also investigated acoustooptic interaction in a ZnO coated optical fibre. In section IV, we have presented results concerning an in-fibre photoelastic phase modulator. Phase modulation of 0.492 rad/ $\sqrt{\text{W}}$  was obtained for a 0.8 mm long modulator and for the telecommunication

wavelength of 1550 nm. This result is, to the best of our knowledge, the best ever efficiency achieved with such a modulators at this optical wavelength. This means that one can deposit c-axis oriented ZnO on highly curved surfaces by using an appropriate rotation stage.

Finally, we have built a quarter pitch graded index device. This device is currently being mounted and bonded by Gooch & Housego Ltd in a special housing. The greatest difficulty was to deposit ZnO on the GRIN lens without damaging the optical anti-reflection coated surfaces. We succeeded in building such a holder, and also in precisely aligning the copper etched electrode mask. Experimental results from this device will be available soon.

## GENERAL CONCLUSION

This report has described the work carried out at the Optoelectronics Research Centre, University of Southampton under the U.S. Air Force project number F 49620-93-1-0494, concerning a "Fibre-compatible acoustooptic modulator using a gradient index lens". A large number of acoustooptic modulator fabrication aspects were investigated.

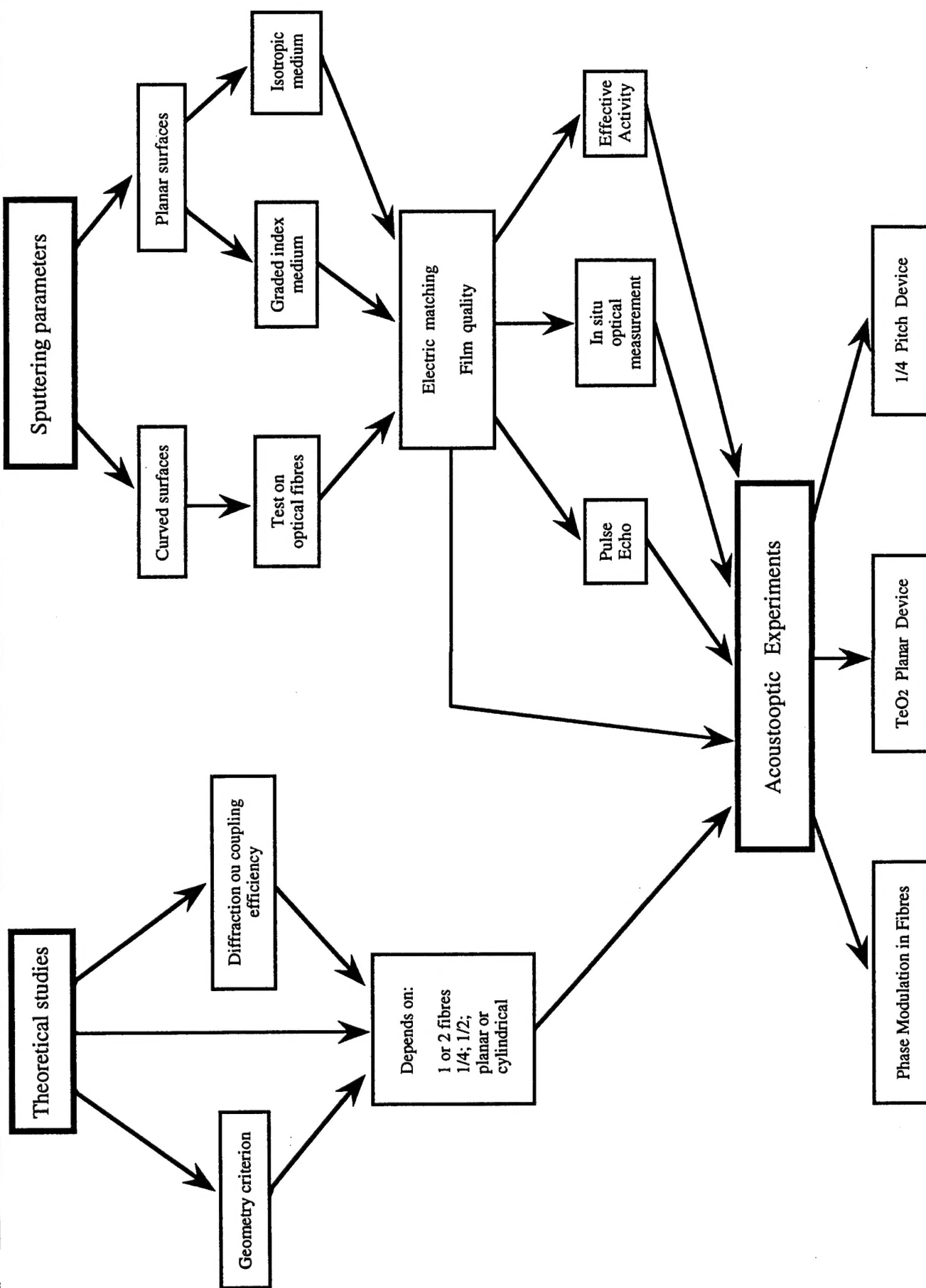
A complete theoretical study concerning the design of fibre-compatible acoustooptic switcher-connectors has been carried out. This part is of great importance since it explains how to build the most efficient AOM according to the characteristics required for different specific applications. The concept of modulators exhibiting a double curvature has been proposed.

The deposition and evaluation of ZnO thin films obtained by RF planar magnetron sputtering has been investigated in detail. During this study, more than 1 mm ZnO has been deposited on various substrates ! This work has highlighted several new aspects concerning the sputtering of thin piezoelectric films. An *in situ* interferometric method used to measure both the film thickness and the depth resolved optical losses of the film has been developed. We also have investigated the real piezoelectric activity of sputtered ZnO films.

Several different acoustooptic modulators have been fabricated and extremely good results have been achieved, in particular concerning the acoustooptic interaction in optical fibres. The main results are; a diffraction efficiency in good agreement with the theoretical calculations, a broad frequency range of operation, low transduction losses, the ability to electrically match every type of transducer, and a phase modulation efficiency in optical fibres twice that which has already been published.

The following diagram emphasizes the large number of essential theoretical and experimental studies that have been carried out during the period November 1993 - November 1994. The next appendices deal with the possibility of improving the performances of our AOM's by using high  $M_2$  graded index materials and new transducer materials. They also deal with new acoustooptic devices.

The work carried out during this year demonstrates the ability of the Optoelectronics Research Centre to build very efficient acoustooptic components. We have established how to make these devices, and we have fabricated some of them. There is no doubt that we will be able to build the new components proposed in the appendices within the near future.





## APPENDICES

### GENERAL COMMENTS AND DIRECTIONS OF RESEARCH

#### I. HIGH $M_2$ GRADED INDEX MATERIALS.

This project started with the initial assumption that the most natural way of building a fibre-compatible acoustooptic modulator(AOM) or "fibre Bragg cell" would be to exploit the imaging properties of a graded index (GRIN) lens. The one problem is the lack of commercially available graded index materials having a high acoustooptic  $M_2$  figure of merit. Despite a large number of enquiries we have not been able to track down any GRIN material other than the borosilicate material used by Nippon Sheet Glass. Commercially available GRIN material are chosen for their ion-exchangeability, not their  $M_2$ ! We have two ideas for manufacturing our own high  $M_2$  materials.

#### **Method (1) : Diffusion of high-polarisability ions into high-index glasses.**

This method is based on the diffusion of cerium ions (to raise the index) into a tube of a lead silicate glass such as SF6 from a melt contained within the tube. After flushing out the salt, the tube will be collapsed and pulled into a cane approximately 1-2 mm diameter. One of the fibre fabricators has once (unintentionally) produced slight index gradients this way and has agreed to repeat the experiment with us, and try to increase the diffusion of cerium.

#### **Method (2) : Creation of GRIN material by direct writing in chalcogenides.**

This method is based on the ability to write index changes into chalcogenide glasses using one or two photon absorption. While a lot of effort has gone into writing structures having high spatial resolution (gratings), we have not found evidence of any effort directed towards exploring the possibility of tailoring the spatial profile of a writing beam to obtain graded index structures of a desired form. We do know, however, that the effects are large enough (typically changes up to nearly 10% may be obtained) to construct the sort of lenses we want.

Chalcogenide glasses have some of the largest  $M_2$  figures of any materials known. We have done some initial experiments with various chalcogenide glass samples obtained from Sassoon

Advanced Materials UK. The most notable result so far is that we found that very large permanent changes in absorption can be produced at  $0.633\text{ }\mu\text{m}$  with an unfocused HeNe beam in arsenic trisulphide. We are in the process of characterising the altered glass as a lens at  $1.5\text{ }\mu\text{m}$ , away from the induced absorption edge. We think that this is an interesting new field in its own right, with applications to the creation of complex structures such as microlens arrays, apart from the acoustooptic applications. In addition, we believe that a two photon absorption process will, if large enough effect can be obtained, remove some of the design constraints from the single photon process. For example, with the single photon process, the write wavelength must always be a compromise between depth of penetration of the beam into the sample (hence the power of the lenses obtainable) and the efficacy of the writing process. In the two photon process and the other hand, there is more freedom to choose the wavelength, subject only to the constraint that the photon energy must be greater than half the band gap. We are currently using a mode-locked YAG laser to irradiate a set of samples of chalcogenides.

There is a large amount of evidence to suggest that all the lenses created by exploitation of photosensitivity in chalcogenides (and other materials such as germanosilicates) are substantially birefringent, thus further increasing the usefulness of lenses produced this way. The birefringence could of course be suppressed if desired by dithering the polarisation during the write operation.

## II ANOTHER TRANSDUCER MATERIAL : BARIUM SODIUM NIOBATE, BSN.

We are investigating the use of BSN as an acoustic transducer material in addition to ZnO for high frequency acoustooptic (AO) devices, and have purchased a sputtering target. This material is ferroelectric, has a very low relative dielectric constant and an electromechanical coupling constant substantially higher than the  $36^\circ$  rotated  $\text{LiNbO}_3$  which is conventionally used for most AO devices. Problems of twinning in the basal plane which have prevented this material becoming more useful in optical  $\chi^2$  applications do not matter in applications to acoustic wave generation. As the material is ferroelectric, it can be poled after deposition and thus c-axis reversal is unimportant, as long as the c-axis is perpendicular to the substrate. This gives rise to the possibility of obtaining apodised transducers by direct writing with an e-beam or by using suitable masks. Such transducers would be capable of generating acoustic beams of high frequency having arbitrary profiles. One immediate application would be to construct an acoustooptic tunable filter (AOTF) having narrow pass band with no side lobes.

## III NEW ACOUSTOOPTIC DEVICES INVOLVING ZnO TRANSDUCERS.

Consequently to the large amount of work done during this year, several new acoustooptic components may be constructed within few months. These components deal principally with switcher-connectors, frequency shifters, and doped fibre lasers.

### 1) Switcher connector.

This component is certainly the most direct application related to the work presented in this report. We have previously mentioned the problem of coupling the direct and diffracted beams to output optical fibres. The key point is the beam separation at the output face of the device

which has to be at least equal to the optical fibre diameter. Theoretical studies have shown that having a beam separation equal to a fibre diameter lead to important optical coupling losses. A way to overcome that problem is to keep a relatively small beam separation, and to use longitudinally polished optical fibres to reduce the distance between the two cores. Of course, the distance between the two cores has to remain large enough for the light not to be coupled from one fibre to the other one.

## 2) Q-Switched fibre laser.

In this case, we propose to use the high efficiency double curvature  $\text{TeO}_2$  acoustooptic switcher described in part I, in a configuration involving only one output fibre. The advantage of this configuration is to obtain a high diffraction efficiency as well as a low rise time and low optical coupling losses. A acoustooptically Q-Switched fibre laser, using a bulk  $\text{TeO}_2$  modulator, has already been realised at the ORC. The system proposed here reduces the number of intra-cavity interfaces, leading to a higher optical power. Furthermore, the use of high  $M_2$  graded index lenses (described above) should strongly increase the emitted optical power.

## 3) Mode locked fibre laser.

We have presented results concerning an in-fibre acoustooptic phase modulator involving a cylindrical  $\text{ZnO}$  transducer deposited directly on a fibre. This component can easily be used with a rare earth doped optical fibre to build a mode-locked fibre laser. The applications of such fibre laser are various concerning optical telecommunications, code division multiple access systems (CDMA), and optical sensing.

## 4) Fibre-compatible frequency shifter.

In part I, we have quickly presented a fibre-compatible acoustooptic frequency shifter involving a one pitch graded index lens. The interest of the method proposed here is that all the diffracted beams (whatever the applied acoustic frequency is) are focused on the lens axis on the output face of the graded index lens. As a result, the coupling efficiency between the diffracted frequency shifted beams depends only on the output angle. But since variation of the output angle with the applied frequency is small (few degrees), the optical coupling losses remain small. As previously stated, the use of high  $M_2$  graded index lenses should lead to a high conversion efficiency.

## 5) Acoustooptically tunable in-fibre grating.

In-fibre gratings are obtained by using UV interferences on a fibre fabricated with photorefractive materials. The position of the reflection peak of such gratings depends on the core refractive index. Therefore, it is possible to acoustooptically tune the position of the reflection peak by depositing a  $\text{ZnO}$  phase modulator directly on the in-fibre grating.